Development of cellulose-based photoactive nanohybrid membranes for water purification

Ph.D. Dissertation

Bilal El Mrabate

Supervisor:

Dr. Zoltán Németh

Antal Kerpely Doctoral School of Materials Science & Technology

Institute of Chemistry

University of Miskolc,

Miskolc 2021

TABLE OF CONTENTS

Acknowledgment

This thesis is a long-term project, a challenge that we give to ourselves. But above all, it is an excellent story of relationships, meetings, and friendships. This research work could not have been completed without the rich collaboration that I have been able to have with many people and without the precious help and constant support they have given me. I want to show them my gratitude within these few lines.

It will be quite hard for me to acknowledge everyone because it is due to the guidance and help of many people that I was able to complete this thesis.

I would like to warmly thank Dr. Zoltán Németh, Senior Research Fellow, for the confidence he has given in me by accepting the scientific direction of my work. I am thankful to him for allowing me throughout this work to benefit from his great competence, his intellectual rigor, his dynamism, and his willingness to help in all circumstances that I will never forget. Be assured of my devotion and my deep gratitude.

I would like to express my gratitude to all my respected teachers of the University of Miskolc who taught me different subjects during the first two years of the program.

I am also thankful to all the staff of the institute of chemistry.

I also thank my teachers at the University of Mohammed V - Rabat, who gave me a good scientific foundation that helped me and still.

Last but not least, I would like to thank my parents for giving birth to me in the first place and supporting me devoutly throughout my life, my brothers Hamza and Mouad and my little sister Meryem, my dear wife Khadija, and the rest of my family for their non-stop support during my studies and preparation of my Ph.D. dissertation.

This work is a special dedication to my beloved baby Fatima-Ezzahrae. I love you.

This research was supported by the European Union and the Hungarian State, co-financed by the European Regional Development Fund in the framework of the GINOP-2.3.4-15-2016-00004 project, aimed to promote the cooperation between the higher education and the Industry.

List of Figures

List of Tables

Abbreviations:

AA	**A**cet**a**ldehyde
AC	**A**ctivated **c**arbon
BC	**B**acterial **c**ellulose
BET	**B**runauer-**E**mmett-**T**eller - specific surface area measurement
CCVD	**C**atalytic **c**hemical **v**apor **d**eposition
CNC	**C**ellulose **n**ano**c**rystals
CNF	**C**ellulose **n**anofibrils
CNT	**C**arbon **n**ano**t**ube
CNs	**C**ellulose **n**anomaterials
CTAB	**C**etyl **t**rimethyl **a**mmonium **b**romide
CVD	**C**hemical **v**apor **d**eposition
DLS	**D**ynamic **l**ight **s**cattering
DOC	**D**issolved **o**rganic **c**arbon
DOM	**D**issolved **o**rganic **m**atter
E. Coli	**E**scherichia **Coli**
EDAX	**E**nergy-**d**ispersive **X**-ray spectroscopy
EtOH	**E**thanol
FIB-SEM	**F**ocused **i**on **b**eam- **s**canning **e**lectron **m**icroscopy
FTIR	**F**ourier **t**ransform **i**nfra**r**ed spectroscopy
GC	**G**as **c**hromatography
HA	**H**umic **a**cid
ICP-MS	**I**nductively **c**oupled **p**lasma - **m**ass **s**pectroscopy
IEP	**I**soelectric **p**oint
LRV	**L**og **r**etention **v**alue
MB	**M**ethylene **b**lue
MWCNT	**M**ulti-**w**alled **c**arbon **n**ano**t**ube

NBCNT	**N**-doped **b**amboo-like **c**arbon **n**ano**t**ube
NOM	**N**atural **o**rganic **m**atter
NFC	**N**ano **f**ibrillated **c**ellulose
NP	**N**ano**p**articles
POU	**P**oint **o**f **u**se
SDS	**S**odium **d**odecyl **s**ulfate
SEM	**S**canning **e**lectron **m**icroscopy
TEM	**T**ransmission **e**lectron **m**icroscopy
TG	**T**hermal **g**ravimetric analysis
UV	**U**ltra**v**iolet
XRD	**X**-**r**ay **d**iffraction
ZP	**Z**eta **p**otential
ZnO	**Z**inc **o**xide
µCT	X-ray micro-**c**omputed **t**omography

Introduction

Water is an essential compound in our daily life activities and for the environment. Water makes up 60-75% of human body weight, and a loss of 15% of total body water can be lethal. Although 71% of the Earth's surface is covered with water, only 0.2% is suitable for drinking, and its distribution is very inhomogeneous, knowing that 98% is salty, and 1.8% is frozen in glaciers. The quality of most resources we rely on is being drastically reduced and exhausted due to the rapid population growth, climate change, global warming and agriculture activities, etc. [1,2]. Freshwater is necessary for human survival but also serves as a primary raw material for numerous industries. Almost 70% of the world population could be under water-deficit conditions, and millions of people will be suffering from absolute water deficiency by 2025, as claimed by the United Nations [3,4]. Based on these alarming forecasts, the number of people who will experience water deficiency is expected to reach 7 billion by 2050 [5,3]. Given this situation, massive efforts are initiated throughout the world to prevent this emerging crisis. The reuse, recycling, and recovery of water have proven fruitful in creating a new and reliable water supply while not compromising public health, and this can be achieved by improving wastewater treatment plants and related technologies such as membrane filtration, UV disinfection, treatment with activated carbon, ozone, and advanced oxidation to remove the contaminants present in water [6]. Membrane filtration is recognized as one of the most promising and extensively used processes for cleaning wastewater, seawater, and brackish water [7]. However, the use of conventional materials in water treatment processes such as activated carbons and petroleum-based polymers have a large carbon footprint associated with their production and application [8]. Thus, it is critical to employ low-cost, environmentally friendly green alternatives with superior performance and lower carbon footprints for a sustainable future. In this context, adsorption properties, photocatalytic activity, and electrostatic interactions are the most major useful, attractive and clean technology for water treatment, virus removal, and antibacterial properties [9]. Recently bio-based nanomaterials, such as bacterial cellulose (BC), cellulose nanocrystals (CNC), cellulose nanofiber (CNF), referred to as cellulose nanomaterials (CNs), have been investigated for the water treatment process and virus removal since cellulose is recognized as one of the most abundant biopolymers used as a reinforcing material for fiber composite materials [10] and represents one of the most

inexhaustible sources of raw material for the growing need for biodegradable and biocompatible products [11,12]. The advantages of cellulose and cellulose derivatives consist of being environmentally friendly, non-toxic, renewable, low cost, biocompatible, sustainable, and cost-effective sources of carbon-based composites and support material for the development of hybrid nanocomposite materials [13,14]. However, the application of cellulose was limited in food packaging due to their lack of antibacterial activity [15,16]. Functional nanomaterials are widely used to enrich cellulose with antibacterial properties, [17,18,19,20]. Cellulose is used as a support material for carbon derivates, metal nanoparticles, and metal oxides such as TiO_2, ZnO, Fe_2O_3, CuO, Ag, Cu, and multi-walled carbon nanotubes (MWCNT) attracted much attention in the past decade [21,22,23]. Because of their high surface area, water suspendability, and reductive surface functional groups, CNs are attractive supports for carbon derivatives such as MWCNT, metal NPs, and metal oxides. The incorporation of CNs inside polymer matrices - likewise to the addition of carbon nanotubes - modifies the membrane characteristics even at very low weight percentages [24]. The most remarkable property improvement is the large improvements in membrane tensile strength obtained from small weight additions of CNs [25,26]. Other beneficial characteristics include changes to membrane surface hydrophilicity, more superior permeability, higher selectivity, and more excellent resistance to biofouling [27].

Thus, this dissertation focuses on the synthesis of novel cellulose reinforced nanohybrid membranes for the application in the removal of bacteria (such as *E. Coli*) and organic dyes (such as methylene blue). In addition to that, the catalytic hydrogenation of n-butene was also investigated. The overall objectives of this dissertation were as follows:

a) Preparation of the composites (ZnO-MWCNT), which are used as additives to improve the adsorption and photocatalytic properties of as-prepared hybrid membranes. The preparation was performed following two different methods: the impregnation and the solvothermal method. The mechanical and chemical properties of the composite were investigated intensively using different analytical techniques. The photocatalytic activity of the as-prepared ZnO-MWCNT nanocomposite additives was examined through the decomposition of acetaldehyde.

b) Synthesis of the photoactive BC-ZnO-MWCNT hybrid membranes, using bacterial cellulose as matrix material and ZnO-MWCNT composites as additives. Two types of ZnO-

MWCNT additives with different morphologies were used in a wide concentration range from 0% to 90% for BC-based hybrid membranes produced by filtration. The interaction between BC and ZnO-MWCNT and the effect of concentration and morphology of additives on some properties like zeta potential, hydrophilicity, electrical conductivity were studied. Furthermore, the as-prepared membranes were characterized by the use of scanning electron microscopy (SEM), focused-ion beam scanning electron microscopy (FIB-SEM), energy-dispersive X-ray spectroscopy (EDAX), X-ray powder diffraction (XRD), and surface area measurement (BET).

c) The performance of the hybrid photoactive membranes in the adsorption and photocatalytic degradation of methylene blue (MB) under UV irradiation and the removal of *Escherichia coli (E. Coli)* was investigated.

d) Although this thesis's focus point is the water treatment, the application of BC reinforced hybrid membranes in catalytic hydrogenation was also studied through BC-Pt-NBCNT membranes, presenting the wide range of application of cellulose-based hybrid membrane technology.

1. Literature review and knowledge gap

According to World Health Organization (WHO) [28], the drinking water of almost 2 billion people is infected with feces leading to about 502 000 gastrointestinal infections, resulting in severe health implications, including death each year. For countries struggling with providing access to healthy drinking water, adequate water treatment criteria are difficult to fulfill [29,30]. Various treatment methods are constantly being developed to address this problem, with the purpose of removing as high proportion as possible of the contaminant species. Nevertheless, researches show that multiple potentially toxic compounds are still existing [31]. High-efficient nanomaterials for water purification are also under investigation, such as carbon nanotubes (CNTs) [32], cellulose [33], and their composites are exhibiting outstanding performances [34]. These nanomaterials are widely utilized as an adsorption procedure for extracting contaminant species and have also been examined as size exclusion membrane filters that block contaminants while allowing the flow of water [35]. Photodecomposition is also one of the promising processes dedicated to removing pollutants from the environment. During this phenomenon, the adsorbed species on the surface are decomposed by the absorption of photons in the visible, ultraviolet, or infrared regions [36,37]. Photocatalysts are widely used in order to take advantage of photodegradation and decomposition of pollutants. Most of these photocatalysts are semiconductors with the appropriate bandgap, high surface area, morphology, stability, and reusability, TiO_2, ZnO, SnO_2, etc., are widely employed [38,39].

1.1. Carbon nanotubes-based composites in water treatment

Carbon nanotubes (CNTs) are nanoparticles that have unique features such as physical properties, mechanical properties, high chemical resistance, and large surface areas [40]. They can be regarded as cylindrical molecules consisting of a rolled-up graphite layer (a hexagonal lattice of carbon). As a result of these intriguing characteristics, they have gained significant attention in recent years, and many research studies have been devoted to their understanding [41]. Basically, two types of carbon nanotubes can be distinguished. These are the single-walled carbon nanotube (SWCNT) and the multi-walled carbon nanotube (MWCNT) [42].

With their exceptional characteristics, CNTs have been employed in many potential applications. [43,44]. As a result of their large specific surface area and high adsorption capability, MWCNT have been commonly employed in environmental applications [45]. The combination of semiconductors with MWCNT is an ideal strategy to improve photocatalytic performance. MWCNT has large electron storage abilities and conductivity similar to that of copper, consequently, the MWCNT could act as electron reservoirs in the composites [43]. The unique thermal, electrical and physical properties, plus adsorption capacities of cylindrical hollow structures of MWCNT, were explicitly exploited by many researchers to enhance as support for semiconductors with photocatalytic properties. CNTs have certain advantages because they are inert in most reaction conditions. They can give excellent dispersion of semiconductor photocatalysts and create several active sites for photocatalytic degradation [46]. As it was reported earlier, MWCNT can conduct electrons and have a high adsorption capacity for specific organic substrates [47].

The recombination of electron-hole charges is the main disadvantage in photocatalysis that results in inefficient photodegradation [48]. This electron-hole recombination can be reduced by making MWCNT-based composite material with other semiconductor nanoparticles or metal oxides [49]. MWCNT is well known as a material that has the capacity to capture electrons due to its high charge conducting ability that ultimately reduces the phenomenon of electron-hole recombination. Consequently, MWCNT can be viewed as a good acceptor for photo-generated electrons by supporting the interfacial electron transfer process, while the semiconductors can be considered as good electron donors under irradiation [50,51] this phenomenon is explained in Figure1. Different preparation methods were applied to coat many types of semiconductor metal oxides on MWCNT, such as TiO_2 [52,53], SnO_2 [54], Cu_2O [55], CeO_2 [56] and ZnO [57,58,59]. A summing-up of these studies was presented in Table 1.

Due to its broad bandgap of 3.37 eV and a high exciton binding energy (60 meV) at room temperature, ZnO is considered a promising semiconductor material [60]that gained extensive attention as an optoelectronic material due to its outstanding features in electronics, optics, and photonics applications [61]. It is also considered as a right candidate for the application in photocatalytic decomposition of organic compounds under UV irradiation. Moreover, ZnO nanoparticles have numerous advantages for photocatalytic reactions, such as high absorption efficiency of light irradiations, stability, and antibacterial properties [62]. So far, numerous

techniques, such as solvothermal synthesis, sputtering, chemical vapor deposition (CVD), and vacuum infiltration, have been conducted to decorate the surface of MWCNT with ZnO nanoparticles [63,64,65]. Koh *et al.* also published the modification of the MWCNT by ZnO nanorods utilizing the hydrothermal method [66].

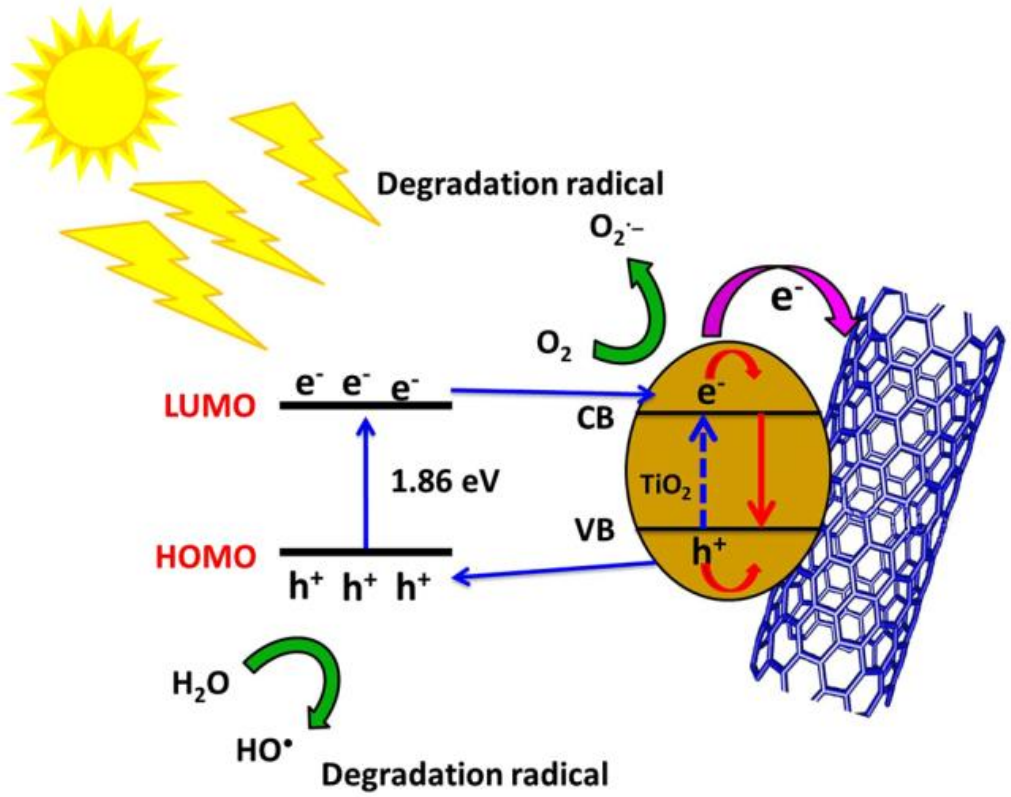

Figure 1. Schematic diagram for the photocatalytic degradation mechanism of MB dye using TiO_2-MWCNT nanocomposite, adopted from [67].

Chen *et al.* made ZnO-MWCNT composites through the acid treatment of MWCNT with HNO_3, H_2SO_4, and NH_3 [68]. Modifying the surface functional groups through acid treatment serves two principal objectives [69]. The first objective is to reduce the agglomeration of nanotubes, diminish impurities, and create open-ended tubes. The second goal of the acid treatment is to give more attachment of functional groups and increase the degree of functionalization, which enables the CNTs to be further chemically modified [70,71]. In composite systems, the particle size and morphology control by an easy and low-cost approach are crucial to their employment in photocatalytic applications.

Table 1. Photocatalytic activity of MWCNT mediated composites.

S. no	Composite	Photocatalytic activity	Reason for enhanced activity/optimization conditions	Ref.
1	MWCNT-TiO_2	Degradation of 2,6-dinitro-p-cresol (DNPC)	0.05% MWCNT in TiO_2; 6.0 g/L catalyst concentration; 150 min irradiation time	[72]
2	MWCNT-TiO_2	Degradation of methylene blue (MB)	Electron acceptor (H_2O_2 used in this study)	[73]
3	MWCNT-TiO_2	Degradation of methylene orange (MO)	MWCNT acted as a dispersing agent to hinder the agglomeration of TiO_2	[74]
4	MWCNT-F-co-doped TiO_2 (MWCNT-FT)	Decomposition of methyl orange under UV irradiation (254 nm)	Non-metal insertion in TiO_2 improves the photocatalytic effects	[75]
5	Thin films of MWCNT-TiO_2	Degradation of Porcion Red dye	No initial requirement of oxidation of MWCNT. The Micellar mechanism of AOT/toluene impart surface charge on MWCNT and TiO_2	[76]
6	Pd/MWCNT-TiO_2	Degradation of MO molecules	The introduction of Pd helps to trap electrons from MWCNT to TiO_2	[77]
7	ITO/MWCNT-TiO_2/ITO	Degradation of Rhodamine B (RhB) molecules	Promoted novel photo-electrocatalytic (PEC) degradation	[78,79]
8	MWCNT-TiO_2	Decomposition of colored dye (RhB)	The treatment of composite with phosphoric acid enhances the amount of O_2 adsorbed on MWCNT	[80]
9	MWCNT-TiO_2	Degradation of rhodamine 6G	10% loading MWCNT remarkably demonstrated a high photocatalytic effect	[81]
10	MWCNT-ZnO	Degradation of RhB	Sonophotocatalytic process (the combination of photocatalysis and ultrasonic irradiation) induces rapid decomposition	[82]
11	MWCNT-ZnO	Photodegradation of methylene blue (MB)	Reduction of recombination rate of photo-generated charge carriers increased by loading CNTs on ZnO	[83]

12	MWCNT-ZnO	Photocatalytic degradation of malachite green under visible light	The MWCNT/ZnO nanocomposites were synthesized through a novel two-step ball milling-hydrothermal synthetic method in which there was no need for initial functionalization of THE MWCNT	[84]
13	MWCNT-$ZnFe_2O_4$	Degradation of methylene blue (MB)	H_2O_2 addition acting as electron scavenger to generate hydroxyl radicals	[85]
14	MWCNT-ZnPc	Degradation of 93.2% of RhB achieved	Zinc phthalocyanine (ZnPc) photo-chemically converts triplet oxygen into singlet oxygen that responsible for the bleaching of RhB	[86]
15	MWCNT-Pd-ZnO	Reduction of aqueous Hg(II)	The doping of Pd into ZnO acting as an electron sink to accept the photo-generated electrons from ZnO, and also Pd declines the recombination rate	[87]
16	MWCNT-BiOCl	Dye degradation of malachite green (MG), congo red (CR), and bromophenol blue (BP)	The 98% in 105 min, 97% in 60 min, and 97% in 90 min degradations were observed under UV irradiation for the BP, CR, and MG, respectively.	[88]
17	MWCNT-$BiPO_4$	Degradation of MO	The employed solvothermal technique endorses the effective contact between $BiPO_4$ and MWCNT rather than the simple mixing	[89]
18	MWCNT-$Bi_4O_5Br_2$	Degradation of tetracycline hydrochloride (TC) and rhodamine B (RhB)	83.1% degradation of RhB in 75 min and 86.2% degradation of TC in 120 min is observed	[90]
19	MWCNT-CdS	Degradation of RhB molecules	Templating agent poly(amidoamine) (PAMAM) dendron on MWCNT to stabilize the higher loadings of CdS nanoparticles	[91]
20	MWCNT-CdS-polymer	Decolorization of MO	CdS/MWCNT/polymer-H_2O_2 system removes 99.9% in 90 min	[92]
21	MWCNT-CdS QDs	Photooxidation of malachite green (MG)	The 94.9% decomposition of MG was observed with 2.5% of CdS QDs/MWCNT catalyst at 20 min	[93]

			under visible light. Quantum dots (QDs) improves the absorption of visible light	
22	MWCNT-Ag@Ag_3PO_4	Decay of malachite green (MG)	3.0 wt% of MWCNT containing Ag@Ag_3PO_4/MWCNT showed strong photocatalytic efficiency. The higher contents of MWCNT abating photocatalytic activity	[94]
23	MWCNT/Ag_3PO_4-AgI	Decontamination of Cr(VI) and orange II	7:3 molar ratio of Ag_3PO_4 and AgI in the MWCNT/Ag_3PO_4-AgI composite showed good photocatalytic activity	[95]

1.2. Nanocellulose-based composites in water treatment

Cellulose is an organic compound formed of repeating units of β linked D-glucose units [96]. Cellulose structure is a hierarchical assembly of elementary fibrils, constituted of 18 to 24 or 36 cellulose macromolecules packed into nanofibrils and microfibrils forming the cell walls of green plants [97,98] as shown in Figure 2. The number of molecules constituting elementary fibrils is still discussed and debated even though this research has been dated for more than 100 years [99].

Nanocellulose (NC) is constituted from these elementary fibrils with diameters as low as 4 nm depending on the source, and lengths are usually in the micrometer range [100]. These elementary fibrils have remarkable mechanical properties due to their high specific surface area with high strength, chemical inertness, and adaptable surface chemistry [101] making NC a promising material for highly efficient membranes and filters in order to selectively eliminate harmful species from industrial and drinking waters [102]. There are three main categories of NCs; bacterial cellulose (BC), cellulose nanofibrillated (CNFs), and cellulose nanocrystals (CNC), also referred to as cellulose nanowhiskers or nanocrystalline cellulose [103]. Table 2 summarizes the three categories of nanocellulose and their synonyms, typical sources, and average dimensions.

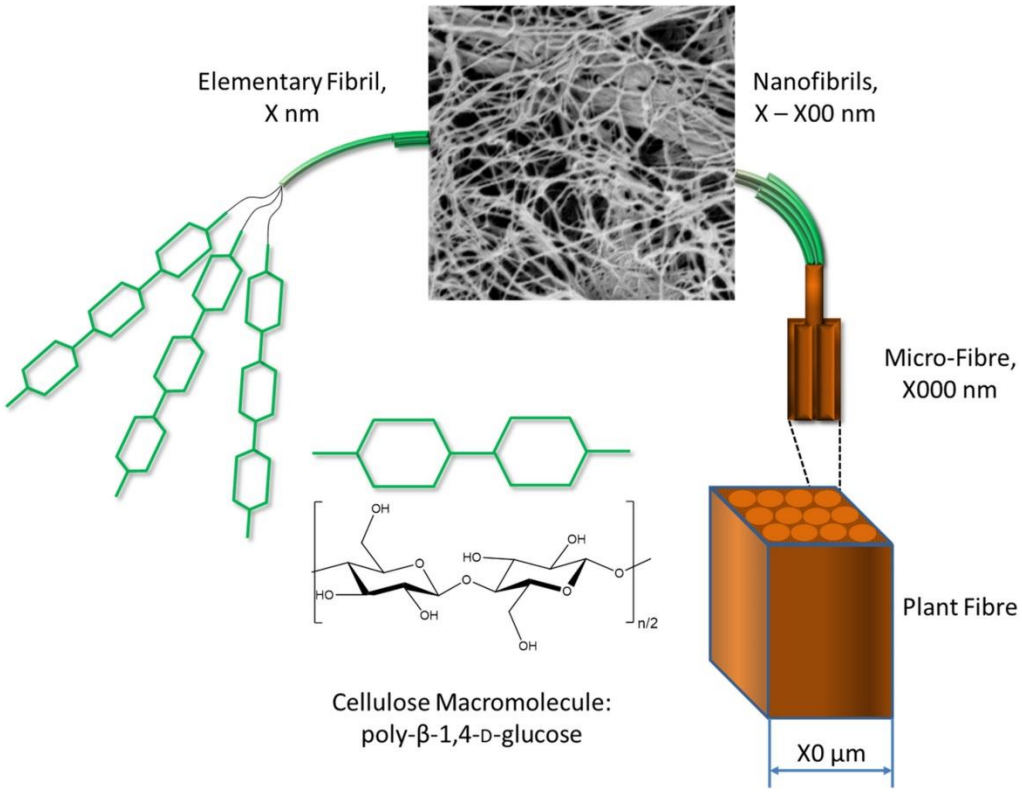

Figure 2. The hierarchical structure of plant fibers [104].

Table 2. Three common types of nanocellulose, as well as their synonyms, typical sources, and sizes

Type of nanocellulose	Synonyms	Typical sources	Average sizes
Cellulose **n**ano**f**ibrillated (**CNFs**)	Cellulose nanofibrils, cellulose microfibrils, and nanofibrillated cellulose	Wood, sugar beet, potato tuber, hemp, and flax	Diameter: 3-60 nm; Length: several micrometers
Cellulose **n**ano**c**rystals (**CNC**)	Nanocrystalline cellulose, cellulose crystallites, cellulose whiskers, rod-like cellulose, and cellulose microcrystals	Wood, cotton, hemp, flax, wheat straw, mulberry bark, ramie, and tunicin	Diameter: 3-60 nm; Length: 100-250 nm
Bacterial **c**ellulose (**BC**)	Microbial cellulose, bacterial nanocellulose, and biocellulose	Low-calorie-weight sugars and alcohols	Diameter: 20-100 nm; Length: several micrometers

BC is ubiquitous in nature, being produced by microorganisms fermenting sugars and plant polysaccharides. *Komagateibacterxylinus* (previously called Acetobacter or *Gluconoacetobacter*) are the best-known bacteria species that are capable of making the fermentation process. [105,106]. Apart from the species utilized, selecting the culture medium and parameters is crucial for the produced BC properties [107]. BC fibrils are discharged from the microorganisms in an accumulated state in the form of planar fleeces/pellicles.

Moreover, growing complex structures, even in three-dimensions, is possible by direct growth templates [108]. CNCs and CNFs are made via the top-down method, obtained by breaking up raw cellulose materials into nanosized particles. In the past, ultrasound was utilized to defibrillate cellulose and isolate CNC from wood pulp and cotton. The particles generated were labeled as crystallites and cellulose micelles, based on the observation of Staudinger of the micellar structure of cellulose [109]. Currently, sulfuric acid is usually used for the acid hydrolysis cleavage of the glycoside bonds in non-crystalline regions of cellulose fibrils, yielding CNCs. CNFs are synthesized by applying strong mechanical machining [110]. The first directed approach to isolate CNFs by mechanical disintegration was revealed by Turbak *et al*. in 1983 [111]. Subsequently, several approaches and devices were proposed and studied, e.g., high-pressure homogenizers, ball milling, ultrasonication, steam explosion, common refiners, or high-speed blenders [112,113].

The application of NC in water treatment can be achieved by different methods [114]. The easy one is utilizing pure NC as adsorbent material. This is achieved by the adsorption of the contaminants such as dyes, heavy metals, etc., on the surface of NC through electrostatic interaction and chemical bonds. The realization of this method strongly depends on a high specific surface area, which can lead to removing multiple pollutants, most importantly cations such as heavy metal ions, organic pollutants including dyes, oils, pesticides, and pharmaceuticals [115]. Nevertheless, the use of several types of modified NC and their affinity toward contaminants has been viewed as a good substitute to the energy-intensive and costly technology based on commercial, activated carbon-based adsorption [116]. Table 3 summarizes the application of NC-based composites towards the adsorption of different organic pollutants. Many hybrid-based cellulose nanocomposites have recently gained more attention as new types of photocatalysts with exceptional optical, electrical, mechanical, and thermal characteristics [117].

Table 3. Cellulose and cellulose-based composites as adsorbents for various types of organic pollutants.

Cellulose derivatives-based composites					
S No.	**NC-based composites**	**Model pollutants**	**Adsorption capacity (mg/g)**	**Duration (min)**	**Ref No.**
1	Amino-functionalized nanocrystalline cellulose	acid red GR congo red 4BS reactive light-yellow K-4G	134.7 199.5 183.0	300	[118]
2	BC-Fe_3O_4 spheres	Pb^{2+} Mn^{2+} Cr^{3+}	65.0 33.0 25.0	120	[26]
3	CNC-alginate hydrogel beads	methylene blue	255.5	210	[119]
4	Carboxylate-functionalized adsorbent based on CNC	crystal violet methylene blue malachite green basic fuchsin	243.90	240	[120]
5	Cationic CNF functionalized with glycidyl trimethylammonium chloride	PO_4^{3-} SO_4^{2-} F^- NO^{3-}	55.0 50.0 10.6 44.0	-	[121]
6	Calcium hydroxyapatite CNF	Cr(VI)	114.79	5	[122]
7	BC-Fe_2O_3-SnO_2	Methylene blue	28.87	60	[123]
8	CNF-TiO_2 composites	Pb^{2+}	371.0	180	[124]
9	Cellulose-ZrO_2 nanohybrid	Ni_2	79	60	[125]
10	BC-Fe_2O_3-ZrO_2 nanohybrid composite	Methylene blue As(III)	38.10 1.01	120	[126]
11	MnO_2-loaded biocomposite based on microcrystalline cellulose	Pb(II)	247.5	180	[127]

12	NC-amino linked by maleic acid supported on magnetite	Arsenic	85.3	90	[128]
13	Cellulose aerogel based on cationic CNF	blue dye CR19 red dye 180 orange dye 142	230 160 560	80	[129]

The low photocatalytic activity of the cellulose and cellulose derivatives under visible or UV light irradiation leads many research groups to modify cellulose with semiconductors to enhance their photocatalytic activity. Various researches have studied the photocatalytic activity of cellulose-based metal oxides such as TiO_2, ZnO, graphene oxide, and Fe_2O_3 in the form of a membrane, thin-film, and hybrid materials water treatment under UV and visible light irradiation. The degradation rate of organic pollutants was enhanced by using these NC-metal oxide composites as photocatalysts compared to pure materials. The application of cellulose-based photocatalyst materials for photocatalytic decomposition of different organic species is presented in Table 4.

Table 4. Application of nanocellulose-based hybrid photocatalysts in photocatalytic degradation of various types of organic pollutants.

Type of catalyst	**Model pollutants**	**Light source**	**Photocatalytic degradation efficiency (%) and reaction time (min)**	**Ref.**
Nanocellulose-graphene oxide-TiO_2 composites	30 mL of 30 mg/L of congo red	sunlight irriadiation with average intensity of ≈900 W/m^2	98%, 240 min	[130]
Nanocellulose-ZnO-graphene oxide composite	25 mL 2–4 mg/L ciprofloxacin	solar light 100 mW/cm^2	98%, 40 min	[131]
Cellulose-ZnO composites	50 mL 3.25 g/L of methylene blue	UV lamp with unknown wavelength and intensity	79%, 300 min	[132]
Hydroxypropyl cellulose/molybdenum disulphide nanocomposite hydrogels	250 mL methylene blue	sunlight	90%, 180 min	[133]

Cellulose-TiO_2-HPM hybrid material	100 mL 10 ppm 4-nitrophenol	250 W halogen lamp (main range 400-800 nm)	85%, 180 min	[134]
BC-graphene oxide-TiO_2 nanocomposite	100 mL 10 mg/L methyl orange	UV lamp (365 nm, 175 W)	100%, 120 min	[135]
Carboxymethyl cellulose-TiO_2 nanocomposite hydrogel	30 mL 30 mg/L congo red	sunlight	91.5%, 240 min	[136]
Flexible cellulose fabrics covered with TiO_2	99.995% CO_2 at a flow rate of 300 mL/min for 1 h	four UVA lamps (8 W each lamp) $\lambda = 365$ nm	194.0 ppm/g and 50.8 ppm/g for CO and CH_4, 360 min	[137]
BC-CdS hybrid fibers	200 mL 20 ppm methyl orange	300 W Xe lamp with a cut-off of $\lambda < 420$ nm	82%, 90 min	[117]
Cellulose fibre covered zinc phthalocyanine	10 mL of 50 μM basic green 1	100 W lamp visible light, $\lambda > 400$ nm	98%, 90 min	[138]
Cu_2O nanoparticles and graphene oxide in cellulose matrix	10 mg/L methyl orange	sunlight (cloudy, 20 °C)	72%, 300 min	[139]
Cellulose-N-doped TiO_2 nanorods thin films	150 mL 40 mg/L methylene blue	UV lamp at $\lambda = 312$ nm, 30 W	96%, 360 min	[140]
Cellulose acetate supported Ag@AgCl composites	methyl orange	500 W Xe arc lamp equipped with a UV cut-off filter ($\lambda > 420$ nm)	73%, 160 min	[141]
BC-TiO_2 membrane	3 mL 15 mg/L reactive red X-3B	UV irradiation with unknown wavelength and intensity	95%, 180 min	[142]

Bacterial cellulose has numerous excellent properties, but the absence of antibacterial activity limits its application to food packaging. Fazli *et al.* [143] have presented a facile method for incorporation of ZnO nanoparticles into BC in order to introduce the antibacterial characteristics into it, the nanohybrid composite BC-ZnO was fabricated by immersing BC pellicles in zinc nitrate solution followed by treating with NaOH solution and then was investigated towards the photocatalytic activity of methyl orange (MO), and the results revealed 91% degradation of MO

under UV-irradiation within 2 h. Furthermore, the BC/ZnO nanocomposites were tested against Gram-positive and Gram-negative and demonstrated significant UV-blocking properties as well as a high bacterial activity against all strains. In another study Guang *et al*. [144] have in situ synthesized silver nanoparticles in BC membranes by template method. The results indicated that the samples showed a strong bactericidal effect of the BC-AgNPs composites towards both *E. Coli* and S. aureus bacteria with more than 8-log reduction and >99.99% killing ratio in the number of viable *E. Coli* after contact for 18h. Szekeres *et al.* [145] prepared a Cu coating on the surface of a cheap organic material (NFC) to prepare an efficient virus membrane, which could be a promising solution for an optimized, high-performance point of use (POU) virus filter (Figure 3). Firstly, the group investigated the adsorption capacity for both poly(tetrafluoroethylene) (PTFE) membrane and the pure NFC in batch experiments by stirring on-air, only the pure NFC showed a <1Log retention and none of the rest showed any measurable effect on the virus concentration. Cu-NFC showed a 3Log virus retention in batch experiments. Cu-NFC showed a 3Log virus retention in batch experiments. Cu-functionalized membranes of 50 mg of NFC were used in the flow experiments at pH = 5.0, 7.5, and 9.0. These filters exhibited virus retention of 3 magnitudes at pH = 7.5 and 9.0 and retention of 4 magnitudes at pH = 5.0. By using so-called double amount (DA) filters, the virus removal passed five magnitudes (LRV > 5) at all three pH values; based on results, the authors concluded that both the quantity of Cu and the NFC quantity act significantly on the synthesis of an effective filter.

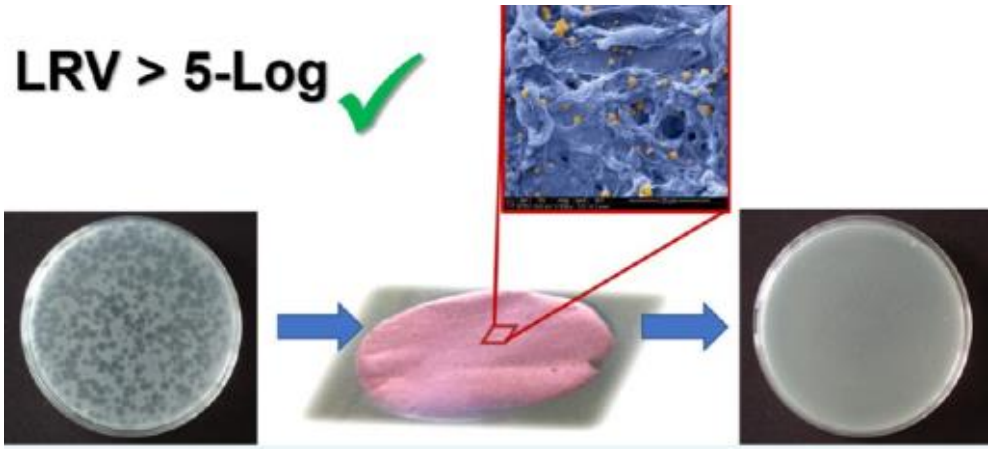

Figure 3. Photograph of MS2-infected *E. Coli* culture after MS2 bacteriophage filtration with Cu-NFC filters [148].

Zhou *et al.* [146] developed a new nanohybrid catalyst consisting of CuO nanoparticles (NPs) supported on the surface of nanocellulose crystals, which demonstrates superior catalytic activities for the reduction of 4-nitrophenol compared with unsupported CuO NPs and other catalysts (e.g., graphene oxide-supported CuO) for this reaction. Their results suggest that this enhancement is a result of both the high surface area of the CNCs and the abundant hydroxyl groups-induced immobilization of CuO NPs, which also leads to a very stable CuO NPs-CNCs suspension. Sun *et al.* [147] have reported the fabrication of BC-TiO_2 hybrid nanofibers with high surface area and high photocatalytic activity. The oriented anatase TiO_2 nanoparticle arrays were implanted on BC fibers using a molecular imprinting technique. The BC-TiO_2 hybrid nanofibers are mesoporous and consist of partially cemented anatase particles with diameters in the range of 4.3-8.5 nm and a surface area of 208.17 m^2/g. The BC-TiO_2 hybrid nanofibers show high photocatalytic activity and exceed that of Degussa P25. Yang *et al.* [117] have reported a facile approach to fabricate BC-CdS hybrid nanofibers with high photocatalytic activity. The photocatalysis activity of the recently produced BC-CdS hybrid nanofibers was examined by MO degradation. The results show that the robust BC-supported CdS nanoparticles are useful in the photocatalysis degradation of organic dyes such as MO. Moreover, shape and size-controlled CdS pasted on BC nanofibers allow the possibilities as recyclable photocatalyst in the field of catalytic methods. Ma *et al.* [148] made CNC-based nanofibrous microfiltration (MF) membrane by impregnating CNC into the polyacrylonitrile (PAN) electrospun nanofibrous structure, resulting in a cross-linked nanofibrous mesh with a very high surface-to-volume ratio. The as-prepared membrane possessed an overage pore size of 0.22 μm, a narrow pore size distribution, and a high retention ratio (LRV = 6) against bacteria: *E. Coli* and B. diminuta (through screening filtration). The produced CNC had a large surface (negative) charge density (zeta potential was -75.2 mV), as validated by the adsorption of positively charged dyes.

1.3. Knowledge gap

As can be seen and concluded from the literature review, many reports and scientific papers investigated the synthesis as well as the application of MWCNT composites; however, the effect of solvent conditions on the preparation of ZnO-MWCNT composites on the photocatalytic activity performance has not been investigated, yet. Furthermore, no study compared the influence of solvothermal and impregnation methods on the structural, optical, morphological properties, and photocatalytic activity of the ZnO-MWCNT composites. The preparation and investigation of NC-based composites in the field of water treatment towards various species present in contaminated water were reported, and numerous semiconductor materials (TiO_2, ZnO, graphene oxide, CdS, and Fe_2O_3) have been added to NC in order to improve the photocatalytic degradation as well as the adsorption capacity of NC towards different organic pollutants present in contaminated water. Although, several studies have reported the fabrication and application of BC, CNC, or CNF with different organic-inorganic materials, including photocatalysts such as TiO_2, ZnO, CuO, Fe_2O_3, etc., or MWCNT, the fabrication, the antibacterial properties and the photocatalytic activity of the BC-ZnO-MWCNT nanohybrid membranes have not been studied so far.

1.4. Objectives

The current work's primary objective is to create an efficient water treatment solution derived from sustainable and most abundant renewable resources at low cost and fabricated through a facile preparation synthesis. Therefore, a stable and self-supported BC-ZnO-MWCNT membrane constituted of MWCNT as a material with high adsorption capacity, ZnO as a photocatalyst, and BC as a support material with high mechanical strength and high hydrophilicity properties was produced. The adsorption capacity, the photocatalytic degradation, and the antibacterial activity of the as-prepared hybrid membranes were investigated.

1- The preparation has been performed following two phases:
   a) The first phase is the synthesis of the ZnO-MWCNT composites was achieved by two preparation methods, the impregnation method, and the solvothermal synthesis.
   b) In the second phase, the BC-ZnO-MWCNT hybrid membranes were produced using a papermaking technique that involves passing the prepared suspension through a

microfiltration apparatus under vacuum, then the prepared membranes were pressed slightly.

2- The as-prepared ZnO-MWCNT composites and the hybrid membranes were extensively characterized utilizing different analytical techniques to mention XRD, BET, SEM, FIB-SEM, Raman spectroscopy, contact angle measurements, zeta potential measurements, etc.
3- Subsequently, the photocatalytic activity of the ZnO-MWCNT composites was investigated towards the degradation of acetaldehyde, and a comparison of the efficiency has been made based on the solvent conditions in which the composites were prepared. Eventually, the BC-ZnO-MWCNT hybrid membranes were applied as adsorbent materials and photocatalysts for the decomposition of methylene blue; furthermore, the antibacterial activity was studied towards the removal of *E. Coli* as *Gram-negative* bacteria.

2. Materials and methods

2.1. Materials used

For the synthesis of MWCNT

- Acetylene (C_2H_2) (Sigma-Aldrich)
- Iron (Fe) (Sigma-Aldrich)
- Cobalt (Co) (Sigma-Aldrich)
- Calcium Carbonate ($CaCO_3$) (Sigma-Aldrich)

For the synthesis of NBCNT

- N-butylamine as a carbon source (Sigma-Aldrich)
- Hydrochloric acid (Sigma-Aldrich)
- Nickel (II)-nitrate hexahydrate (Merck)
- Magnesium oxide (Merck)

For the synthesis of ZnO-MWCNT nanocomposites:

- Sodium-dodecyl-sulphate (SDS) (Sigma-Aldrich)

- Hydrochloric acid (HCl) (Sigma-Aldrich)
- Zinc acetate ($Zn(CH_3COO)_2 \times 2H_2O$) (Sigma-Aldrich)
- Multi-walled carbon nanotubes (MWCNT) (Nanocyl, Belgium)
- Absolute Ethanol (EtOH) (VWR chemicals)
- Deionized water (H_2O)
- Cetyl trimethyl ammonium bromide (CTAB) (Reanal, Hungary)

For the synthesis of BC-ZnO-MWCNT hybrid membranes:

- BC fibers were received from nata de coco cubes (FI, Philippines)
- Absolute Ethanol (EtOH) (VWR chemicals)
- Polytetrafluoroethylene (PTFE) filter (pore size of 0.22 μm and the diameter of 47 mm)
- As-prepared ZnO-MWCNT nanocomposites

For the synthesis of BC-Pt-NBCNT:

- Nickel (II) nitrate hexahydrate (Merck)
- Magnesium oxide (Merck)
- n-butylamine (Sigma-Aldrich)
- Hexachloroplatinic (IV) acid (Merck)
- Nitrogen (99.995%, Messer)
- Hydrogen (99.999%, Messer)
- 1-butene (99.500%, Messer)
- Hydrochloric acid (36 wt%)
- Distilled water
- BC fibers were received from nata de coco cubes (FI, Philippines)
- Absolute Ethanol (EtOH) (VWR chemicals)
- Polytetrafluoroethylene (PTFE) filter (pore size of 0.22 μm and the diameter of 47 mm)
- Platinum solution (0.04 g $H_2PtCl_6 \times H_2O$ in 0.5 ml water)

2.2. Syntheses

2.2.1. Preparation of MWCNT and NBCNT

MWCNT was prepared by the catalytic chemical vapor deposition (CCVD) method in a rotary oven at 720 °C in nitrogen flow. Acetylene was utilized as the carbon source, and Fe, $Co/CaCO_3$ as the catalyst, and the total concentration metal was 5 wt%. The support material and the catalyst particles were removed by stirring the product in 10% hydrochloric acid (HCl) for 1 h, and then it was filtered and washed with distilled water until neutral pH was achieved. The average diameter of the MWCNT was 20-60 nm, while average lengths were about a few hundred nanometers to few micrometers [149,150]. The specific surface area of the MWCNT was 182.1 m^2/g. The main features of MWCNT Raman spectra are the D, G, and G′ peaks. The purity of the carbon phase can be easily determined by the rations of these three peaks, and the metal content was previously regarded with a quantitative ICP-MS analysis [151]. This analysis and peak intensity ratios in the case of MWCNT indicate good quality and a highly graphitic nature.

N-doped BCNT (NBCNT) was produced by the chemical vapor deposition (CVD) method. For that, nickel (II)-nitrate hexahydrate (Merck) and magnesium oxide (Merck) were used as the catalyst, and N-butylamine was applied as the carbon source (Sigma-Aldrich) in a tube furnace at 700 °C in nitrogen flow. To remove the residual support material and catalytic particles, the as-prepared NBCNT was treated with cc. HCl (36 wt. %) under vigorous stirring for two hours, then washed with distilled water until neutral pH was achieved.

2.2.2. Preparation of ZnO-MWCNT composites under different solvents conditions

The chemical adsorption of SDS molecules on the surface of the MWCNT induces electrostatic repulsion between polar heads that expose in the aqueous solution, thus preventing MWCNT aggregation and inducing the formation of stable black suspensions. Non-covalent functionalization of MWCNT is necessary, therefore pristine nanotubes were dispersed in 2 wt% dilute SDS aqueous solution [152] to modify MWCNT surface. The ZnO-MWCNT composites were prepared by a simple impregnation method. Surface-treated MWCNT was applied as raw material and $Zn(CH_3COO)_2 \times 2H_2O$ as precursor compound. MWCNT contents were fixed at 10 wt% of the total ZnO-MWCNT composites calculated to the final crystallized product after annealing. Initially, 0.1 g SDS modified MWCNT was dispersed in 50 mL water and EtOH via

ultrasonication for 15 min. During this time, the exact amount of the precursor (2.45 g) was dissolved in another 50 mL of water and EtOH. For complete dissolution of the precursors, the solution was stirred vigorously using a magnetic stirrer for 10 min at 300 rpm. Finally, the precursor solution was added drop by drop (~2 mL/min) to the MWCNT suspension under continuous stirring. Then, the mixture was heated to 40 °C to evaporate EtOH and 70 °C to evaporate H_2O on a hot plate. The composite powder was further dried at 70 °C in air for 12 h. Finally, the as-prepared nanomaterials were annealed in a static furnace in air with a heating rate of 5 °C/min for 3 h at 300 °C to obtain crystalline ZnO. Materials of ZnO for comparative examinations were prepared precisely in the same way as the composites without the presence of MWCNT.

2.2.3. Preparation of ZnO-MWCNT applying different syntheses methods

To prepare the ZnO-MWCNT composites two different synthesis routes were applied. These were the impregnation and solvothermal methods. The precursor solution was prepared by dissolving 2.42 g of zinc acetate in 50 ml of EtOH and left under vigorous stirring for 15 min at 300 rpm to ensure complete dissolution. Meanwhile, a suspension of purified MWCNT (100 mg) was sonicated in 100 ml of EtOH for 15 min using an ultrasonic laboratory homogenizer (40 kHz and output power of 40 W; Heilsher GmbH, Germany). The MWCNT content was set at 10 w/w% in the final composites' total mass in both cases. For impregnation synthesis, the solution of precursor was dropwise added (at 1 ml min^{-1}) to the MWCNT suspension. Then, the mixture was kept reacting under mechanical stirring for 12 h; afterward, it was heated up to 75°C to evaporate the solvents. Eventually, the final product was annealed at 400°C for 4 h in air at 5°C min^{-1} heating rate to form ZnO nanoparticles on the surface of MWCNT. In the case of the solvothermal route, the MWCNT suspension was added directly to the precursor solution under stirring. Next, the mixture was emptied into 150 ml stainless steel autoclaves with an attached Teflon tube and then placed in a static furnace for 12 h at 150°C. Afterward, the residues were removed by centrifugation and washing, and then the samples were annealed at 400°C at 5°C min^{-1} heating rate for 4 h. The final products synthesized by impregnation and solvothermal were named ZnO-MWCNT-IMP and ZnO-MWCNT-SOLVO, respectively. The surface properties of the ZnO-MWCNT composite additives synthesized by both methods were modified through treatment with

CTAB, which also helps to stabilize them against van der Waals attraction. [153,154]. The modification was achieved by dispersing 0.1 g of ZnO-MWCNT composite material in 50 cm^3 of the CTAB solution (0.05 M) in deionized water. The solution was sonicated for 10 min and then stirred for 4 h. Subsequently, it was centrifuged and washed with distilled water until neutral pH was achieved. Finally, the powders were dried overnight in air at 100 °C.

2.2.4. Preparation of BC-ZnO-MWCNT hybrid membranes

The BC-ZnO-MWCNT nanohybrid membranes' preparation was achieved by immersing the calculated amount of BC fibers into 15 ml EtOH to obtain the BC suspension. Meanwhile, the ZnO-MWCNT-IMP and ZnO-MWCNT-SOLVO composite additives were sonicated in 50 ml EtOH for 15 min. The composite ZnO-MWCNT additives' content in the final nanohybrid membrane was varied in a wide range from 10 to 90 w/w%. The BC suspension was then mixed with the ZnO-MWCNT-IMP and the ZnO-MWCNT-SOLVO suspensions and mechanically stirred for 5 h at 300 rpm. Finally, the BC-based hybrid membranes were prepared by vacuum filtration through a PTFE membrane to reach a loading of 8 mg cm^{-2} (the total mass being 100 mg per membrane), then kept to dry in air under pressing. The membranes were denoted as IMP 10-90 and SOLVO 10 - 90 depending on the preparation route (IMP, SOLVO) and the composite additive concentration (10 - 90%). Figure 4 shows a schematic illustration of the preparation of the hybrid membranes.

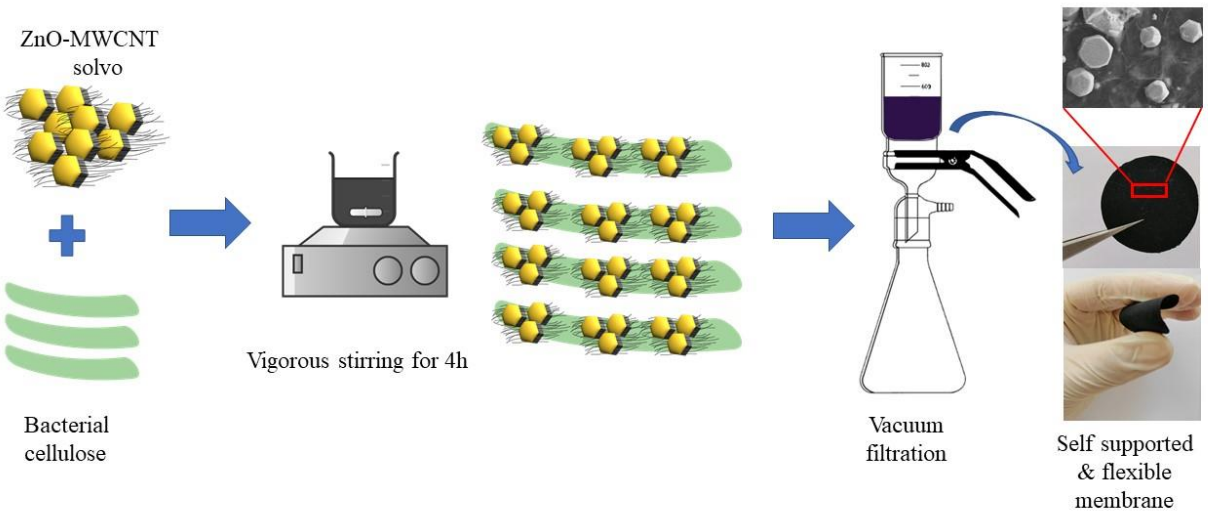

Figure 4. Schematic illustration of the preparation of BC-ZnO-MWCNT-SOLVO hybrid membranes

2.2.5. Preparation of the BC-Pt-NBCNT hybrid membranes

To prepare the BC-Pt-NBCNT nanohybrid membranes with an NBCNT content of 90 w/w% in the final product, a suspension of BC was first prepared by immersing the calculated amount of BC fibers into 15 cm^3 EtOH. Simultaneously, the NBCNT was sonicated in 50 cm^3 EtOH for 15 min. Then, the NBCNT suspensions were poured into the BC suspension, and the mixture was kept under stirring for 5 h at 300 rpm. The final BC-based hybrid membranes were achieved by vacuum filtration through a PTFE filter to reach a total mass of 100 ± 10 mg/membrane with a loading of 8.0 ± 0.9 mg/cm^2), then each membrane was dried overnight in air under pressing. In the next step, a 0.5 cm^3 20 wt% platinum solution (0.04 g $H_2PtCl_6 \times H_2O$ in 0.5 cm^3 water) was used for the impregnation of the BC-NBCNT membranes (100 mg). During the process, 0.25 cm^3 of the platinum solution was dropwise added to both sides of the membranes. Impregnated membranes were dried at 120 °C overnight. Finally, BC-Pt-NBCNT membranes were hydrogenated at 400 °C for 30 min in a tube furnace with a 50 mL/min hydrogen flow rate.

2.3. Characterization of composite materials and hybrid membranes

2.3.1. Transmission electron microscopy (TEM)

The formation of ZnO inorganic nanoparticles on the surface of MWCNT was verified by transmission electron microscopy (TEM, Philips CM10). For TEM investigations, a small amount of the sample was sonicated in 1.25 mL of distilled water. A few drops of this suspension were then dribbled onto the surface of the grid (LC200- Cu TEM grid covered with lacey carbon film-Electron Microscopy Sciences-USA).

2.3.2. Scanning electron microscopy (SEM)

The morphology of the ZnO-MWCNT, BC-ZnO-MWCNT, and BC-Pt-NBCNT samples was investigated by scanning electron microscope. SEM investigation of the ZnO-MWCNT composites was performed by a Hitachi S-4800 Type FE-SEM operating in the range of 0-30 keV. Before the measurement, the samples were mounted on conductive carbon tape. In the case of BC-ZnO-MWCNT hybrid membranes, focus-ion beam scanning electron microscopy (FIB-SEM) was also used, the SEM investigations were performed with the use of Hitachi S-4800 Type II FE-SEM operating in the range of 0–10 keV, and the FIB-SEM measurements were done with a Thermo

Helios G4 PFIB CXe instrument. The surface morphology of the BC-ZnO-MWCNT hybrid membranes before and after *E. Coli* filtration experiments was investigated by SEM and FIB-SEM using the same instruments mentioned before. The SEM measurements of the BC-Pt-NBCNT hybrid membranes were done with Thermo Helios G4 PFIB CXe and JEOL JSM 7200F instruments.

2.3.3. Energy-dispersive X-ray spectroscopy (EDAX)

The energy-dispersive X-ray spectroscopy (EDAX) measurement of the ZnO-MWCNT composites and the BC-ZnO-MWCNT hybrid membranes was completed with the scanning electron microscope equipped with a Röntec XFlash Detector 3001 SDD device. Energy-dispersive X-ray spectroscopy (EDAX) measurement of the BC-Pt-NBCNT was performed by a scanning electron microscope (Thermo Helios G4 PFIB CXe) and an Ametek EDAX Octane Elect Plus (detector area 30 mm^2) device.

2.3.4. X-ray micro-computed tomography equipment (µCT)

The three-dimensional architecture of the BC-ZnO-MWCNT hybrid membranes was characterized using YXLON FF35 dual-beam X-ray micro-computed tomography equipment (CT) (microfocus X-ray tube, transmission beam, acceleration voltage: 50 kV).

2.3.5. X-ray powder diffraction (XRD)

The crystalline structure of the as-prepared ZnO-MWCNT composites was determined by powder X-ray diffraction method (Rigaku Miniflex II Diffractometer) utilizing characteristic X-ray (CuKα (λ = 15405 Å)) radiation). Scanning was carried out over a 2θ range of 10 - 80° with a step size of 0.0167°.

In the case of the BC-ZnO-MWCNT hybrid membranes, the crystalline structure was determined by the X-ray powder diffraction (XRD) method (Bruker D8 Advance diffractometer) with Cu Kα radiation (40 kV and 40 mA) in parallel beam geometry (Göbel mirror) with a position-sensitive detector (Vantec1, 1° opening). Measurements were taken in the 2–100° (2θ) range with 0.007° (2θ)/14 s goniometer speed, on top-loaded specimens in zero-background Si sample holders. The presence and physiognomy of platinum nanoparticles on the surface of BC-Pt-NBCNT hybrid membranes were investigated by X-ray diffraction (XRD) with a Bruker D8 Advance diffractometer (Cu-Ka source, 40 kV and 40 mA generator settings), equipped with a Vantec1 position sensitive detector (1 window opening). The instrument's parallel beam geometry

(by Göbel mirror) allowed measurements to be made at the milligram level without the need for pressing powder specimens. Zero background sample holders (Si crystal cut) eliminated the issue of sample transparency; thus, no sample holder contribution presents. Measurements were taken in the 2°– 100° (2θ) range with 0.007° (2θ)/14 s goniometer speed, on top-loaded specimens in zero background Si sample holders.

2.3.6. Surface area measurement (BET)

The specific surface areas of the samples were determined by the adsorption of nitrogen at 77 K according to the method of Brunauer-Emmett-Teller [155]. After the samples were pre-treated at 300 °C for 15 min in helium atmosphere (50 mL/min), measurements were carried out by a single point BET instrument (BEL Japan Inc. BELCAT-A). To determine the surface area and micropore volume (t-plot method) of the BC-ZnO-MWCNT hybrid membranes Nitrogen (N_2) adsorption-desorption experiment was performed at 77 K using (ASAP 2020, Micromeritics Instrument Corp. Germany). Before each measurement, the samples were degassed at 90 °C for 24 h.

2.3.7. Thermogravimetric analysis (TG)

Thermogravimetric analysis (NETZSCH STA 409 PC connected to a Pfeiffer QMS 200 mass spectrometer system) of the ZnO-MWCNT composites was performed in the air (measurement range: 25–800 °C, flow velocity: 40 mL/min, heating rate 10 °C/min) using 100 mg sample.

2.3.8. Dynamic light scattering (DLS)

Electrophoretic measurement of the BC-ZnO-MWCNT hybrid membranes was performed by dynamic light scattering (DLS) (ZetaSizer NS, Malvern, UK) device. The measurement is based on the combination of laser Doppler velocimetry and phase analysis of light scattering (PALS) in Malvern's M3-PALS technique.

2.3.9. Mercury intrusion porosimetry (MIP)

The BC-ZnO-MWCNT hybrid membranes were also investigated by mercury intrusion porosimetry (MIP) to determine the pore size distribution. Measurements were done on PASCAL 140 (low pressurization system down to 0.04 MPa) and PASCAL 440 (high pressurization system up to 400 MPa) instruments (manufactured by Thermo Scientific).

2.3.10. Fourier transform infrared spectroscopy (FTIR)

The hydrogenation process of 1-butene and the catalytic activity of the BC-Pt-NBCNT membranes was followed by vertex 70 type Fourier transform infrared spectroscope (FTIR) in a gas cell with a KBr window.

2.3.11. Raman spectroscopy

Raman spectroscopy measurements of the ZnO-MWCNT composites and the BC-ZnO-MWCNT hybrid membranes were performed by a high-resolution Raman spectrometer Nicolet Almega XR (Thermo Electron Corporation, USA) with a 532 nm Nd:YAG laser (50 mW).

2.3.12. UV-VIS spectroscopy

The UV photoreactor applied was equipped with fluorescent lamp (Vilber-Lourmat T-6L UV-A, 6 W power, radiation maximum at 365 nm). Changes in the concentrations were followed with gas chromatograph (Agilent 6890 N) using a HP-PLOT Q column, equipped with thermal conductivity (TC) and flame ionization (FI) detectors and Agilent 5975C VL MSD mass spectrometer.

2.3.13. Gas chromatography (GC)

The changes in the concentration of acetaldehyde were followed with gas chromatography (Agilent 6890 N) using an HP-PLOT Q column, equipped with thermal conductivity (TC) and flame ionization (FI) detectors and Agilent 5975C VL MSD mass-spectrometer.

2.3.14. Contact angle measurement

Contact angle measurement of the BC-ZnO-MWCNT hybrid membranes was carried out using the sessile drop method (SP 12 melt microscope, Sunplant Ltd, Hungary), making a silhouette shot. KSV software (KSV Instrument Ltd, Finland) was used to evaluate the recording and determine the angular values.

2.3.15. Colorimetric and water vapor absorption

The color of the BC-ZnO-MWCNT hybrid membranes was measured using a HunterLab Color Quest XE (USA) colorimeter (D65/10°) and compared to the white background tile of the apparatus. Color difference (ΔEab*) and lightness (L*) values were determined in CIELab color space. Water vapor sorption is usually used for characterization of the internal surfaces of cellulose-based substrates available for water vapor molecules and determined by exposing the

samples, previously dried over P_2O_5 for 5 days, to an atmosphere of 65% RH at 25°C for 5 days and calculated as the percentage of the dry weight.

2.3.16. Tensile strength, tear elongation, electrical conductivity

Mechanical properties of the BC-ZnO-MWCNT hybrid membranes were examined by an Instron 5566 tensile tester (USA) at 10 mm min^{-1} cross-head speed and 10 mm gauge length on specimens with 5 mm width. At least four parallel measurements were performed and averaged. A LabView-based measurement system was used to perform the electrical conductivity measurements. The measurement setup constituted an NI PXI-1044 chassis, an NI PXI-8106 embedded controller module, and an NI PXI-4071 high-precision DMM (digital multimeter) module. For the measurements of the resistance (conductance) of the sample, the Kelvin (four-wire) method is used.

3. Results and discussions

3.1. Investigation of ZnO-MWCNT composites prepared under different solvents conditions

3.1.1. TEM analysis

The ZnO-MWCNT composite samples were investigated by the TEM technique. Figure 5 shows TEM micrographs at various magnifications of the prepared ZnO-MWCNT nanocomposites. The fabrication of ZnO-MWCNT composites using $Zn(CH_3COO)_2 \times 2H_2O$ as precursor and SDS modified MWCNT was successful using both solvents, although different composite structures were observed during TEM observations. Figures 5 (A, B) show representative electron micrographs obtained from the investigation of composite materials prepared in ethanol. TEM images revealed that ZnO nanoparticles covered most MWCNT, and segregated particles could not be observed during analysis. Figures 5 (C, D) present views of the nanocomposite sample prepared in water, and these images demonstrated that the surface of MWCNT was covered weakly with ZnO nanoparticles. Larger, segregated ZnO crystallites and uncovered MWCNT were also observed when water was used as the solvent. By analyzing the as-prepared products, it can be concluded that EtOH provides more uniform ZnO-MWCNT nanocomposite samples. In previously published results, ZnO crystallites with different

morphologies can be observed using different solvents, such as water, ethanol, and *n*-propanol [156]. The surface tensions of these solvents are very different from each other, so the final composite morphology can be varied easily by changing the solvent.

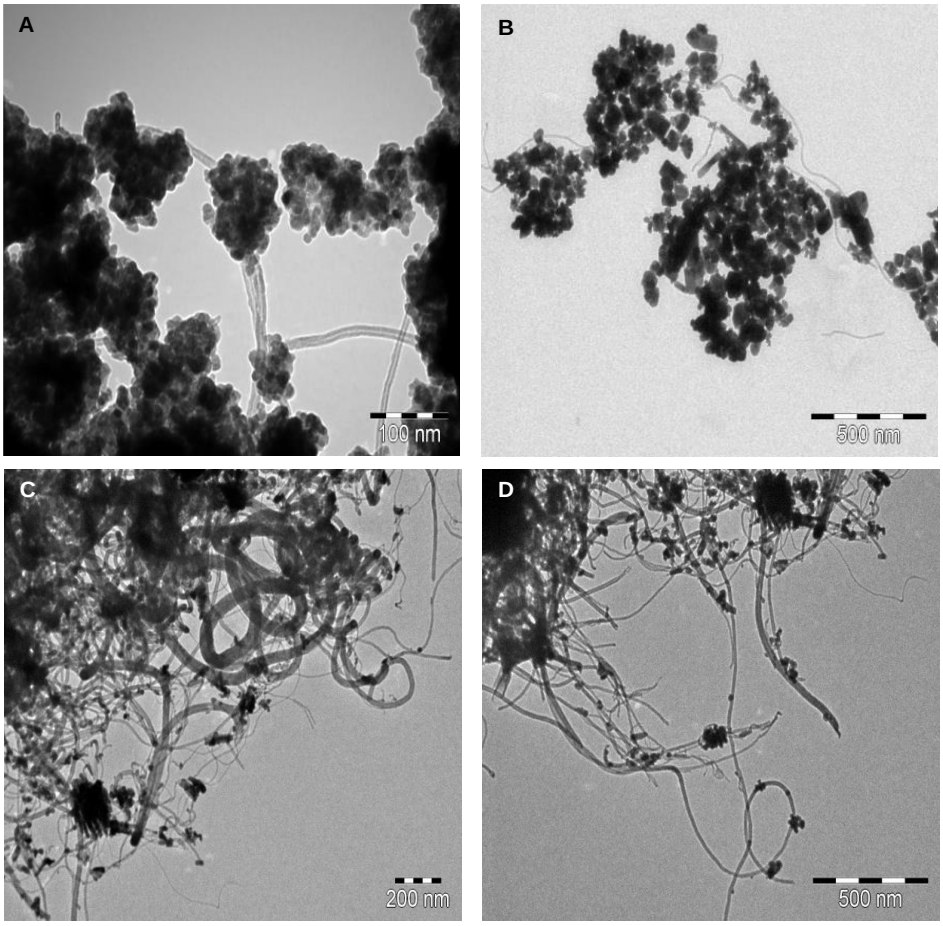

Figure 5. TEM images of ZnO-MWCNT nanocomposites applying EtOH (A, B) and water (C, D) as a solvent

3.1.2. TG, XRD, and BET analysis

To identify the ZnO nanoparticles and transform the amorphous phase into the crystalline phase, the composite samples were heat treated. Before that, the DTG gave us essential information about the phase transformations resulting from the rise of the temperature (Figure 6). The first thermal event was observed up to 100 °C with ~14.9% weight loss. This weight loss can be associated with the thermal dehydration of $Zn(CH_3COO)_2 \times 2H_2O$ and, more specifically, with the loss of the two water molecules. By further increasing the temperature, the decomposition of anhydrous $Zn(CH_3COO)_2$ into ZnO occurs at ~250 °C and is completed at ~300 °C with a ~28.8% weight

loss. Beyond this temperature and up to 400 °C, the formation of stable ZnO crystal takes place. Based on these results, we decided to perform the calcination at 300 °C for 3 h since a stable ZnO phase is obtained. Further thermal events can be noticed from 450 °C to 550 °C with a ~4.8% weight loss, which belongs to the burning of SDS modified MWCNT.

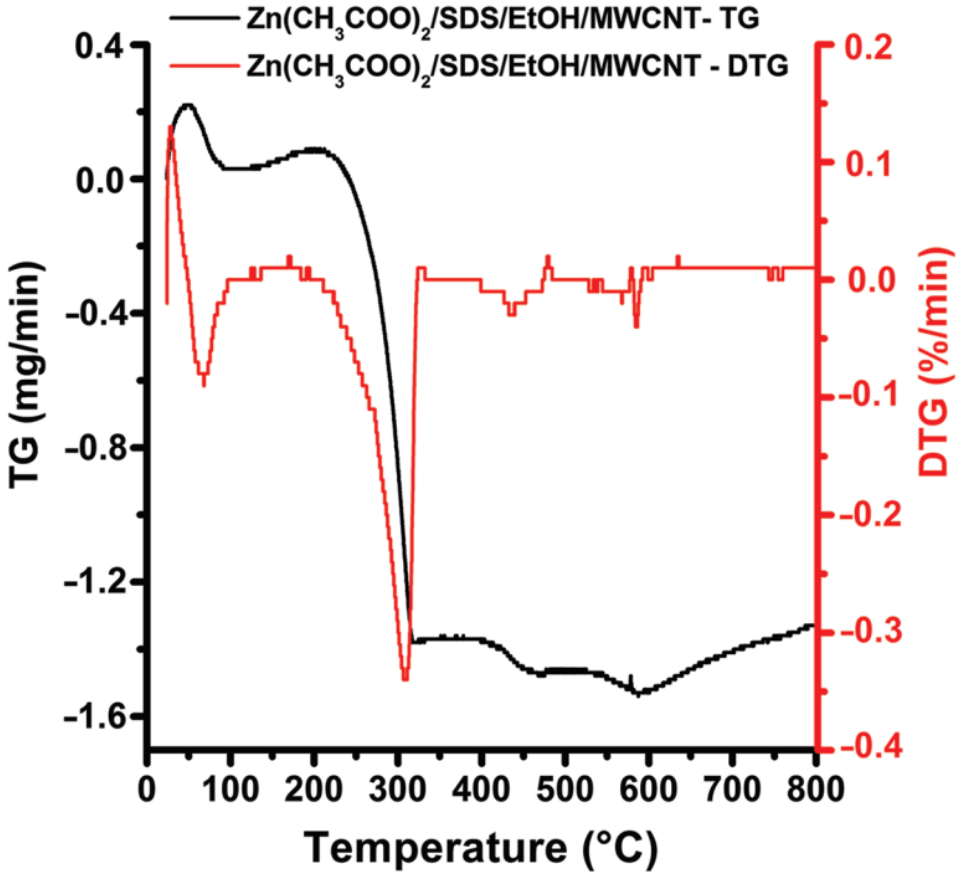

Figure 6. Thermal analysis of $Zn(CH_3COO)_2 \times 2H_2O$/SDS/EtOH/MWCNT nanocomposite material.

The degree of crystallization of composite samples was investigated by XRD. The results of the analysis are presented in Figure 7. The diffraction peak at $2\theta = 26.5°$ can be identified as the 002 reflection of MWCNT. The other diffraction peaks in the range of $20° < 2\theta < 80°$ correspond to the (100), (002), (101), (102), (110), (103), (200), (112), (201), (004) reflections of ZnO. The average crystalline size of inorganic particles can also be estimated from X-ray diffractograms by the Scherrer equation [157]:

$$\boldsymbol{D = (K\lambda)/(\beta \cos \theta)}$$

Where D is the diameter (in nanometer) of the grain or the layer, K is the shape factor (0.89), λ is the X-ray wavelength of Cu Kα (0.154 nm), is the experimental fullwidth half maximum of the respective diffraction peak(s), and θ is the Bragg angle. Furthermore, from the analysis of the TEM pictures, the average particle sizes were also calculated using iTEM software (Olympus Soft Imaging Solutions). The particle size distribution was concluded by measuring the size of 100 particles in all samples. We considered that the TEM images only show a 2D projection of the 3D particles; thus, the observed particle size distribution is a distribution of the particles' projected dimension. Particle size values obtained with the two different calculations showed good agreement. Table 5 shows the average particle diameters (d_{av}) in nanometers, calculated from TEM and XRD investigations. In the case of pure MWCNT, TEM images were used only to determine the average diameter. As-prepared MWCNT-based filter materials were also characterized by the N_2 adsorption technique to measure their specific surface area. Table 5 shows the measured specific surface area values.

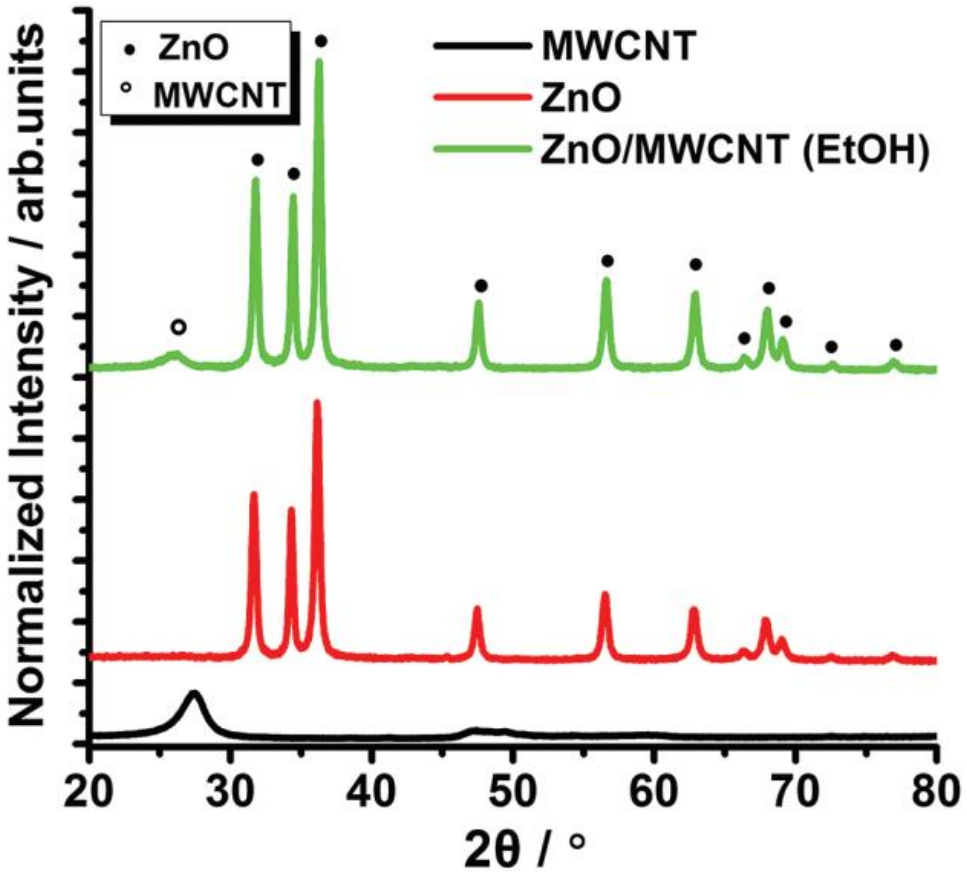

Figure 7. X-ray diffractograms of heat-treated raw materials and ZnO-MWCNT nanocomposite sample prepared in EtOH.

Table 5. Particle size (in average) and specific surface area of raw materials and MWCNT based composites

Sample name	$d_{average}$ (nm)	BET (m^2/g)
MWCNT	35.8	182.1
ZnO	15.1	51.2
ZnO-MWCNT/EtOH	20.2	64.3
ZnO-MWCNT/H_2O	23.4	61.8

3.1.3. Determination of photocatalytic efficiency

Photocatalytic experiments of the ZnO-MWCNT composites prepared under different solvent conditions were carried out using the system, which can be seen in Figure 8. The applied UV photoreactor (Figure 8 A - marked by a red circle) was equipped with a fluorescent lamp (Vilber-Lourmat T-6L UV-A, 6W power, radiation maximum at 365 nm). The added amounts of the photocatalysts were 0.5 g/L, and acetaldehyde (AA), a harmful chemical material (Spektrum3D, 99.0 %), was used to characterize the photocatalytic activity of the specimen. First, MWCNT composites were suspended in EtOH with a concentration of 0.5 mg/mL. In the next step, 100 mL portions of these ZnO-MWCNT suspensions were deposited onto high purity alumina-based ceramic papers (COTRONICS Corporation-Ultra Temp 300) [158] with a diameter of 47 mm by simple filtration, enhanced with vacuum suction. Every suspension was used within a few hours to avoid MWCNT aggregation, which could alter the membranes' final performance. As a final step, the as-prepared MWCNT composite membranes were dried at 100 °C for 30 minutes to remove residual solvents. As-prepared alumina-based ceramic membranes, with a load of 0.75 mg/cm^2 (50 mg/membrane), were cut into half to fit into the sample vial easily and placed into glass vials equipped with opening and locker plastic head as can be seen in Figure 8B.

Figure 8. UV photoreactor (left corner-A) with GC (A) and glass vials with ZnO-MWCNT nanocomposites, pristine ZnO, alumina paper, and MWCNT (B).

Glass vials were rinsed with N_2 gas before starting the photocatalytic decomposition of AA. Then, vials were filled with a saturated vapor of AA (0,987 bar; 20 °C; 0.9 mM) and wait until the adsorption equilibrium state (~40 min). Vials were placed into a stationary reactor and irradiated the specimen in AA atmosphere with a wavelength of 365 nm at room temperature for 120 min. Changes in AA concentrations were followed with a gas chromatograph (Agilent 6890 N) using an HP-PLOT Q column, equipped with thermal conductivity (TC) and flame ionization (FI) detectors and Agilent 5975C VL MSD mass-spectrometer. The split ratio was 10:1 in all cases. Each nanocomposite sample was tested three times. As reported previously, several types of intermediates can be generated during the decomposition of AA (e.g., formaldehyde, acetic acid) [159]. However, the main product was CO_2. In this report, the determination of CO_2 by gas chromatography was performed.

3.1.4. Photocatalytic decomposition of acetaldehyde

Before photocatalytic measurements, blank experiments were carried out to determine the decomposition of AA without any photocatalysts. The AA transformation was below 5 % during 120 min long irradiation. The adsorption capacities of laboratory-prepared nanocomposites were also measured in dark experiences. Results pointed out that nanocomposites produced via the utilization of EtOH solvent during the synthesis method resulted in higher adsorption ability. These

materials adsorbed 10-15 % of AA at applied concentration after 120 min. in the dark, while nanocomposites produced in water solution adsorbed only 5-8 % of AA. The estimated difference in adsorption capacities cannot be connected to the specific surface areas since these properties of the materials are very similar (see Table 5). The difference probably due to some unclarified special surface property resulted from the different solvents applied during synthesis methods. The adsorption capacity of pure alumina ceramic membrane was also investigated under dark conditions. Pure alumina membrane adsorbed only 1-3% of AA (Figure 9 - brown curve). The photocatalytic behaviors of the raw materials, the pure alumina ceramic paper, the simple mechanical mixture of MWCNT and ZnO, and ZnO-MWCNT composites were examined as shown in Figure 9. In the case of the ZnO + MWCNT mechanical mixture, the MWCNT content was 10 wt % also. Comparing the decomposition efficiency of the modified MWCNT, the pristine ZnO, the mechanical mixture of MWCNT and ZnO with the as-prepared ZnO-MWCNT nanocomposites, it was found that ZnO-MWCNT nanocomposites have comparatively higher photocatalytic activity, as can be seen in Figure 9 (green and yellow curves).

Furthermore, ZnO-MWCNT composite prepared in EtOH possesses the highest photocatalytic activity in the AA degradation reaction, which comes up to 71 % in the AA photocatalysis processes. While by ZnO-MWCNT photocatalyst, 71 % (using EtOH as a solvent - Figure 9 green curve) and 65 % (using H_2O as a solvent - Figure 9 yellow curve) AA was decomposed after 120 minutes of irradiation, by ZnO-MWCNT mechanical mixture only 35 % of AA was degraded after 120 minutes. Furthermore, it was found that the decomposition curve shape of pure MWCNT (Figure 9 - black curve) is different from other curves, which is related to the excellent adsorption of AA by MWNT because of high specific surface area (182.1 m^2/g) and the tubular structure of MWNT [58]. Presumably, this can be a plausible explanation for the higher photocatalytic activity of MWCNT than ZnO or the ZnO + MWCNT mechanical mixture.

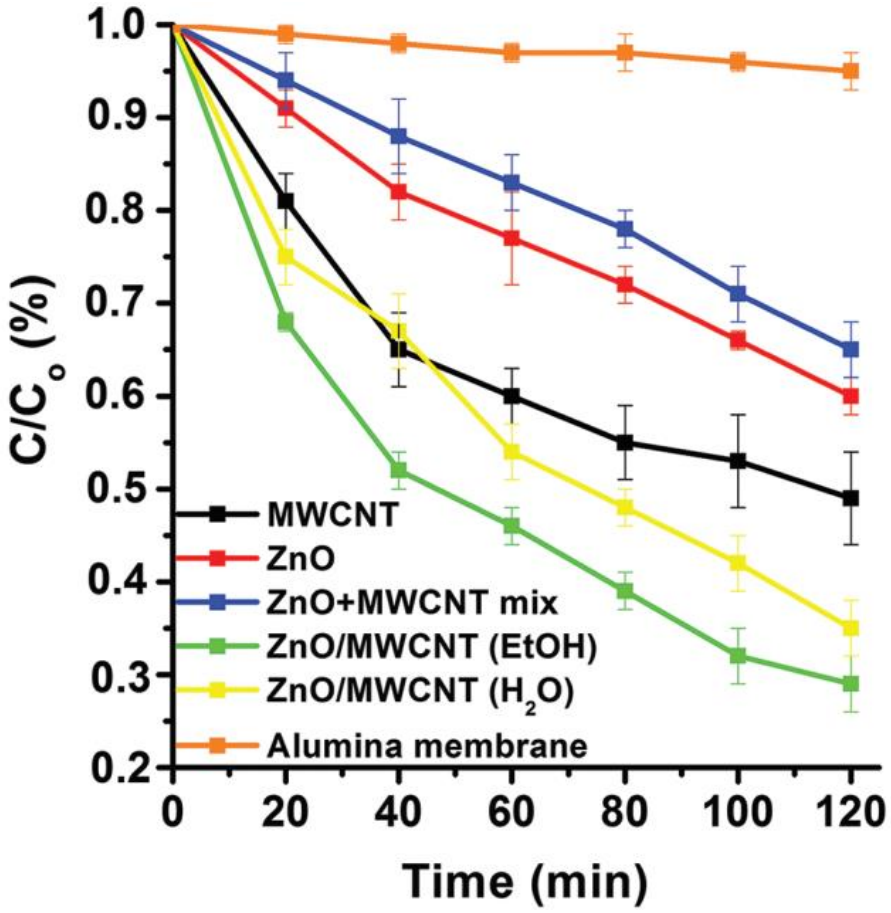

Figure 9. Photocatalytic decomposition of AA (c_{AA} = 0.9 mM; λ_{max} at 365 nm) by ZnO nanoparticles, MWCNT, pure alumina membrane, the mechanical mixture of ZnO and MWCNT (ZnO + MWCNT) and ZnO-MWCNT nanocomposites prepared in EtOH and H_2O.

3.2. Investigation of ZnO-MWCNT composites prepared by different syntheses methods

3.2.1. SEM and EDAX analysis

The as-prepared ZnO-MWCNT composites were observed with SEM and EDAX techniques. The fabrication of ZnO-MWCNT composites from ethanol solution was successful using both of the applied synthesis methods, although different ZnO layer structures were observed during SEM observations. Figure 10 shows representative views at various magnifications of the obtained ZnO-MWCNT composites materials prepared with the impregnation method, and these images revealed

the presence of ZnO nanoparticles formed on the surface of MWCNT. By analyzing the images mentioned above, it was found that the average diameter of ZnO nanoparticles is in the range of 22±5 nm, although ZnO particles were sticking together on the surface of CNTs resulting in larger ZnO agglomerates in some cases. On the other hand, SEM images confirmed that ZnO nanoparticles covered the majority of MWCNT, and separated ZnO particles could not be observed during investigations.

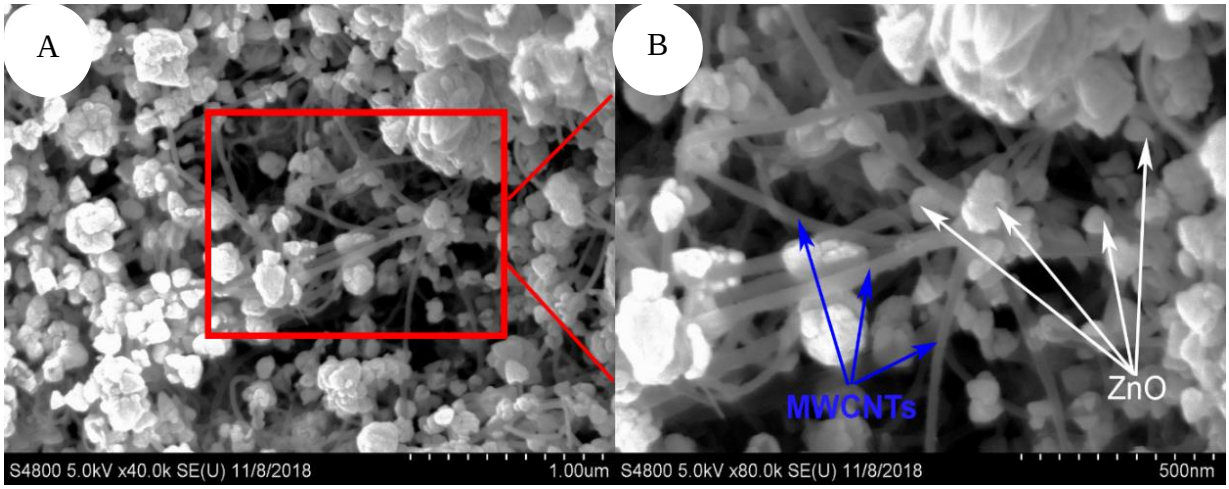

Figure 10. SEM images (A-B) of ZnO-MWCNT nanocomposite prepared by impregnation

Figure 11 A-D shows SEM images at low (Figure 11 A-B) and high (Figure 11 C-D) magnification of ZnO-MWCNT composites prepared by solvothermal method. These images clearly demonstrate that produced composites contain bigger ZnO particles with hexagonal structures. The average diameter of these ZnO hexagonal is between 3-5 µm. SEM observations revealed that MWCNT were built into the ZnO crystals, as can be seen in Figure 11. Based on SEM analysis, it is presumed that not only the solvent but also the applied synthesis technique is could be a determinative parameter during the formation of ZnO particles and the preparation of ZnO-MWCNT composite materials. As shown in Figure 11, ZnO crystallites were aggregated into bigger hexagonal particles in EtOH medium during solvothermal synthesis due to the solvent's surface tension. Consequently, the final morphology of the ZnO-MWCNT composites can be varied easily by applying the suitable method.

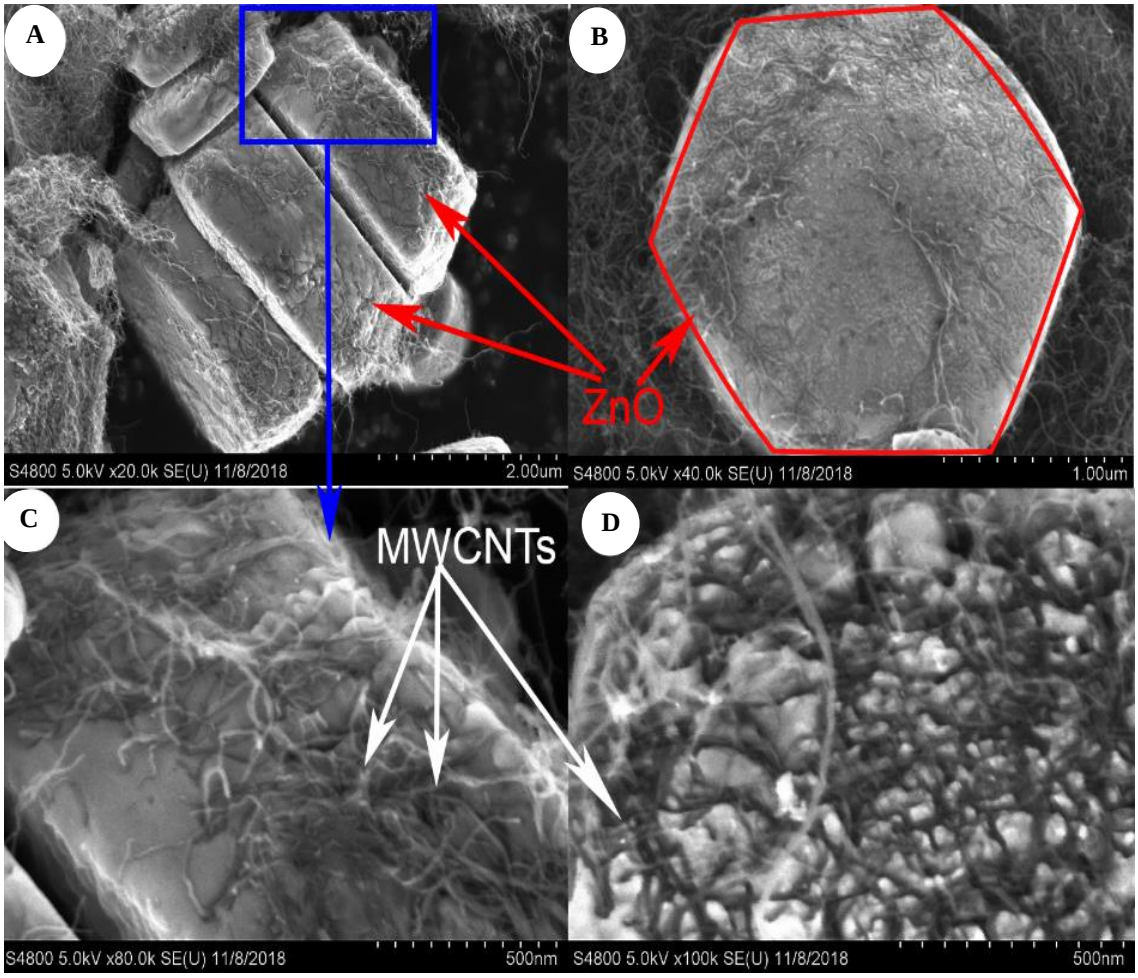

Figure 11. SEM images (A-D) of ZnO-MWCNT nanocomposite prepared by solvothermal method

In order to characterize the quality of ZnO particles on the surface of MWCNT, EDAX analysis was performed by the SEM instrument for each sample. In this dissertation, two EDAX spectra are presented based on the high degree of similarity of the obtained results (Figure 12). The most significant signals are originating from carbon (C), oxygen (O), and zinc (Zn). EDAX analysis confirms the presence of ZnO and MWCNT in the composite samples.

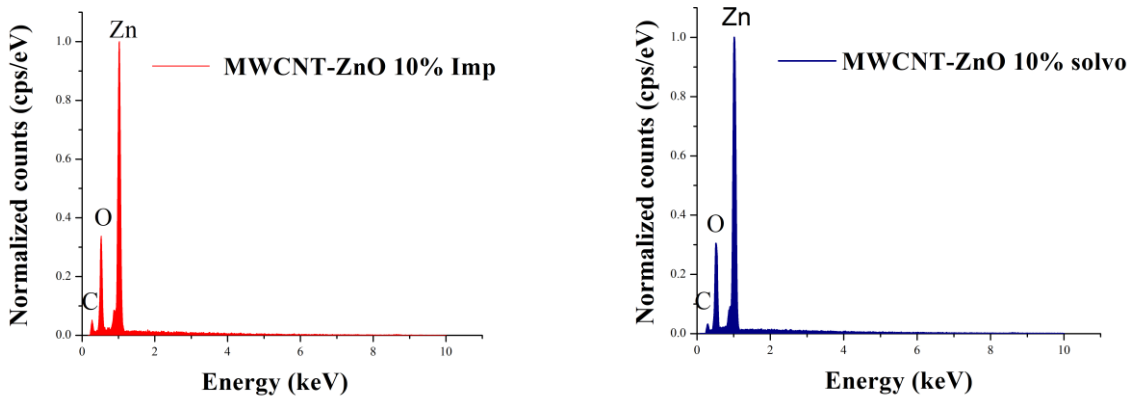

Figure 12. EDX analysis of ZnO-MWCNT nanocomposites

3.2.2. Raman spectroscopy analysis

Raman spectroscopy investigation of the prepared ZnO-MWCNT samples confirmed the presence of ZnO and MWCNT in the composites. Compared to the Raman spectra of pristine MWCNT, and Raman spectra of the products exhibits two peaks at 437 cm^{-1} and 1151 $cm^{-1,}$ which are characteristic peaks of ZnO (Figure 13).

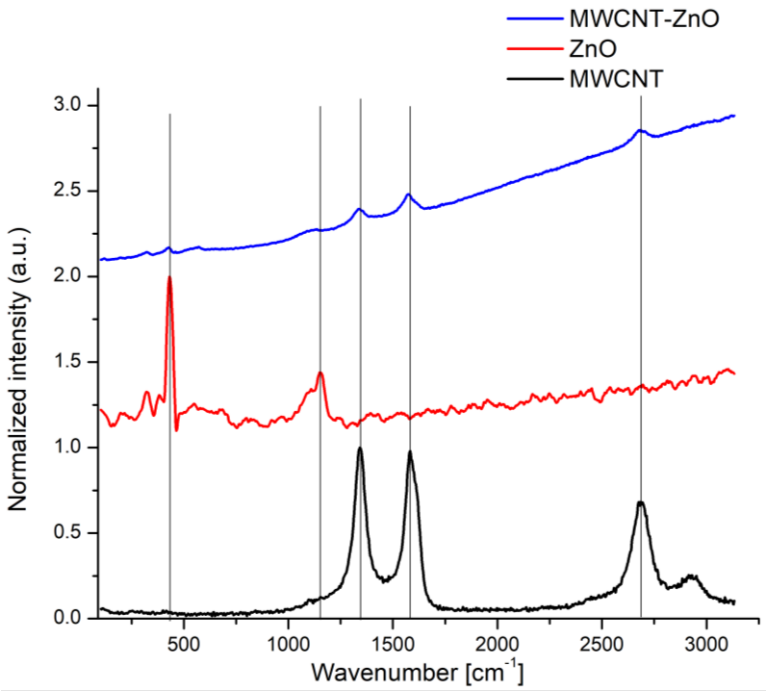

Figure 13. Raman spectra of MWCNT, ZnO, and ZnO-MWCNT composites

Three other strong bands deriving from MWCNT appear at 1340 cm^{-1}, 1574 $cm^{-1,}$ and 2680 cm^{-1}, attributing to the D-, G- and G'- bands of MWCNT, respectively. The sharp and most intensive peak at 437 cm^{-1} in the Raman spectra of ZnO can be assigned to the E2 (high) mode of ZnO, which is the strongest model in the wurtzite crystal structure [160]. Probably due to the interaction between the MWCNT and ZnO particles, the bands slightly shifted, as can be seen in Figure 13.

3.3. Characterization and application of the BC-ZnO-MWCNT hybrid membranes

3.3.1. SEM, EDAX, and μCT analysis

Scanning electron micrographs in Figure 14 show the surface structure of neat BC membrane (A) and hybrid membranes (B, C, E, F). The fabrication of membranes was successful in all cases, although different morphology was observed during SEM investigations. The as-prepared hybrid membranes were stable, flexible, and self-supported, except for the membranes with the highest additive content (IMP 90 and SOLVO 90). These properties can be explained by the interaction between a certain amount of hydroxyl (–OH) groups on BC fibers and the oxygen-containing species on the surface of MWCNT, which resulted in interfacial bonding [161, 162]. SEM images in Figure 14 B and C prove the presence of ZnO nanoparticles on the surface of BC-based membranes prepared by the impregnation method. In a few cases, the ZnO particles stacked together, resulting in larger ZnO agglomerates. Applying ZnO-MWCNT-SOLVO additives (Figure 14 E, F) the produced hybrid membrane consists of typical hexagonal ZnO particles with an average size of 3-5 μm, and likely, the MWCNT was built inside the ZnO crystals. The presence of ZnO particles on the surface of MWCNT was investigated by EDAX analysis and was performed for each sample. EDAX spectra in Figure 14 D and G reveal that the detected signals originated from three elements, carbon (C), oxygen (O), and zinc (Zn), confirming the presence of BC, MWCNT, and ZnO in the hybrid membranes. Furthermore, in order to demonstrate the differences between the distribution and particle size of ZnO crystals, elemental mapping analysis (Figure 14 D, G) was recorded for atoms of interest: C represents both MWCNT and BC, the same as Zn for ZnO. It was discerned that the concentration and distribution of Zn showed a vital difference, therefore confirming the different surface morphology of hybrid membranes.

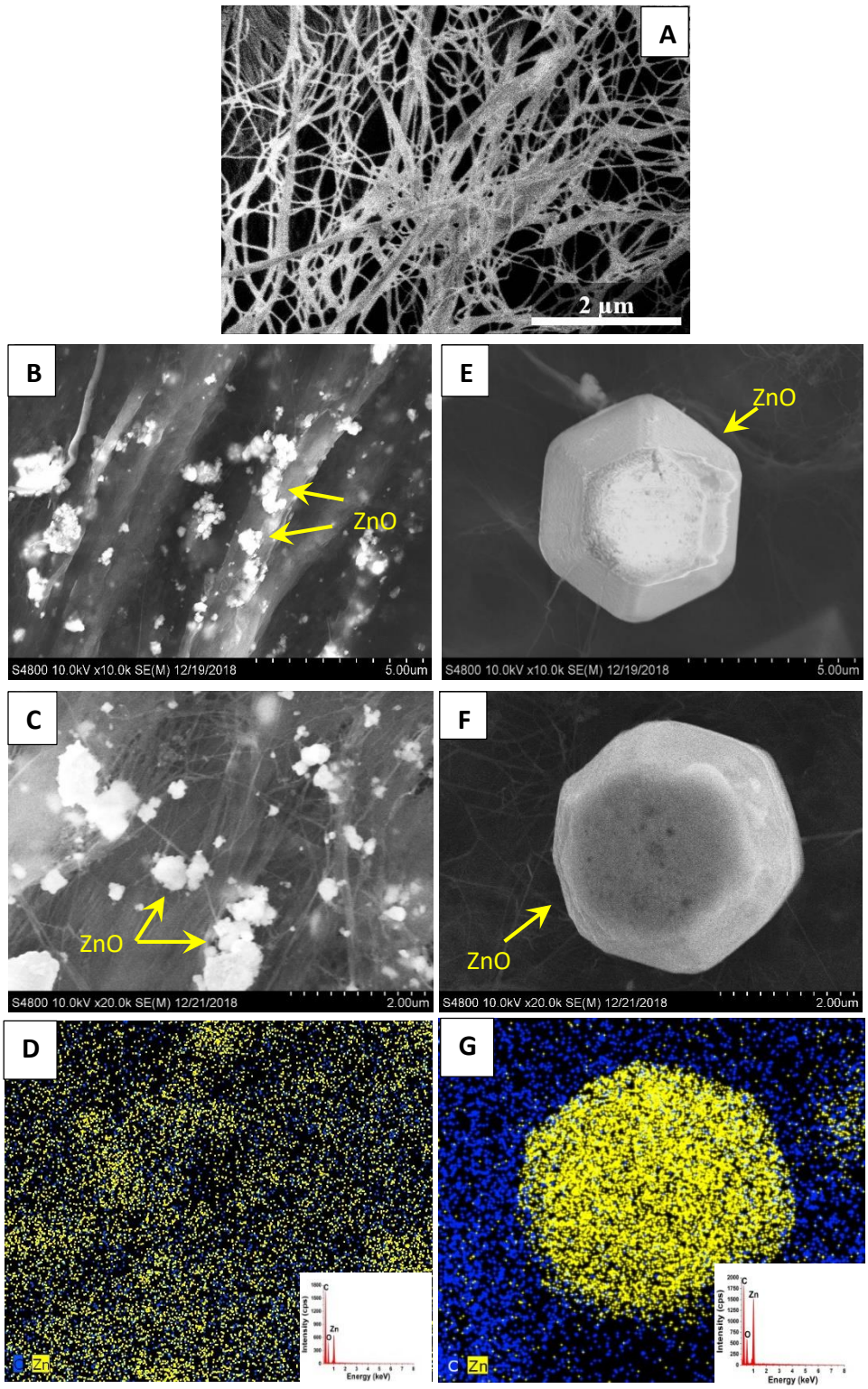

Figure 14. SEM micrographs of pure BC membrane (A) and BC-ZnO-MWCNT hybrid membranes: IMP 20 (B, C) and SOLVO 20 (E, F). EDAX spectra and elemental mapping of hybrid membranes: IMP 20 (D) and SOLVO 20 (G).

FIB-SEM was performed for the SOLVO 20 nanohybrid membrane in order to answer the question of whether the MWCNT is built inside the hexagonal ZnO particles, leading to a variation in the properties of BC-based hybrid membranes. Figure 15 A-C shows the representative SEM images of the outer (Figure 15 A) and internal (Figure 15 B, C) structure of ZnO particles. The ZnO hexagonal particle was beforehand cut to get some knowledge about their morphology. As shown in Figure 15 B, the inside structure of the ZnO crystals contains many cavities. Presumably, this phenomenon could be related to the presence of MWCNT and the crystallization process of ZnO particles. These holes are filled with a tubular material with a wall thickness of approximately 30 nm, as was witnessed on the cross-section analysis in Figure 15 C. Measured values show a good correspondence with the medium diameter of the MWCNT, validating the presence of carbon nanotubes in the internal structure of the hexagonal ZnO. Moreover, the EDAX mapping examination results also prove the presence of MWCNT inside the ZnO particles as the carbon signals were registered in the ZnO particle (Figure 14 G).

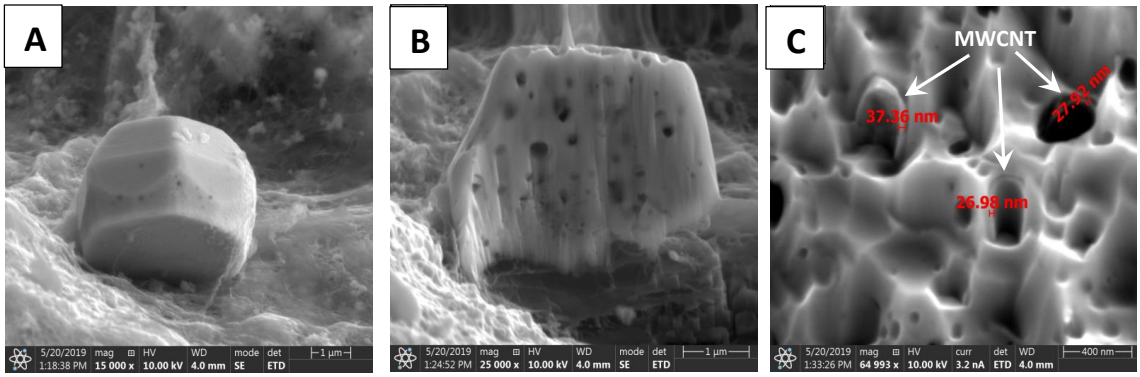

Figure 15. FIB-SEM images of SOLVO 20 hybrid membrane: ZnO microparticle (A), cut ZnO particle (B), the internal structure of ZnO. MWCNT with an average diameter of 30 nm are indicated with white arrows (C).

Although electron microscopy is often used during the analysis of nanocomposite materials, there are some limitations of these techniques - e.g., the size of the investigated area. In order to gain information about the homogeneity and the surface morphology of the whole membrane, CT analysis was performed in the case of SOLVO membranes. Figure 16 A shows the cross-section analysis, while Figure 16 B shows the surface morphology of the SOLVO 50 membrane.

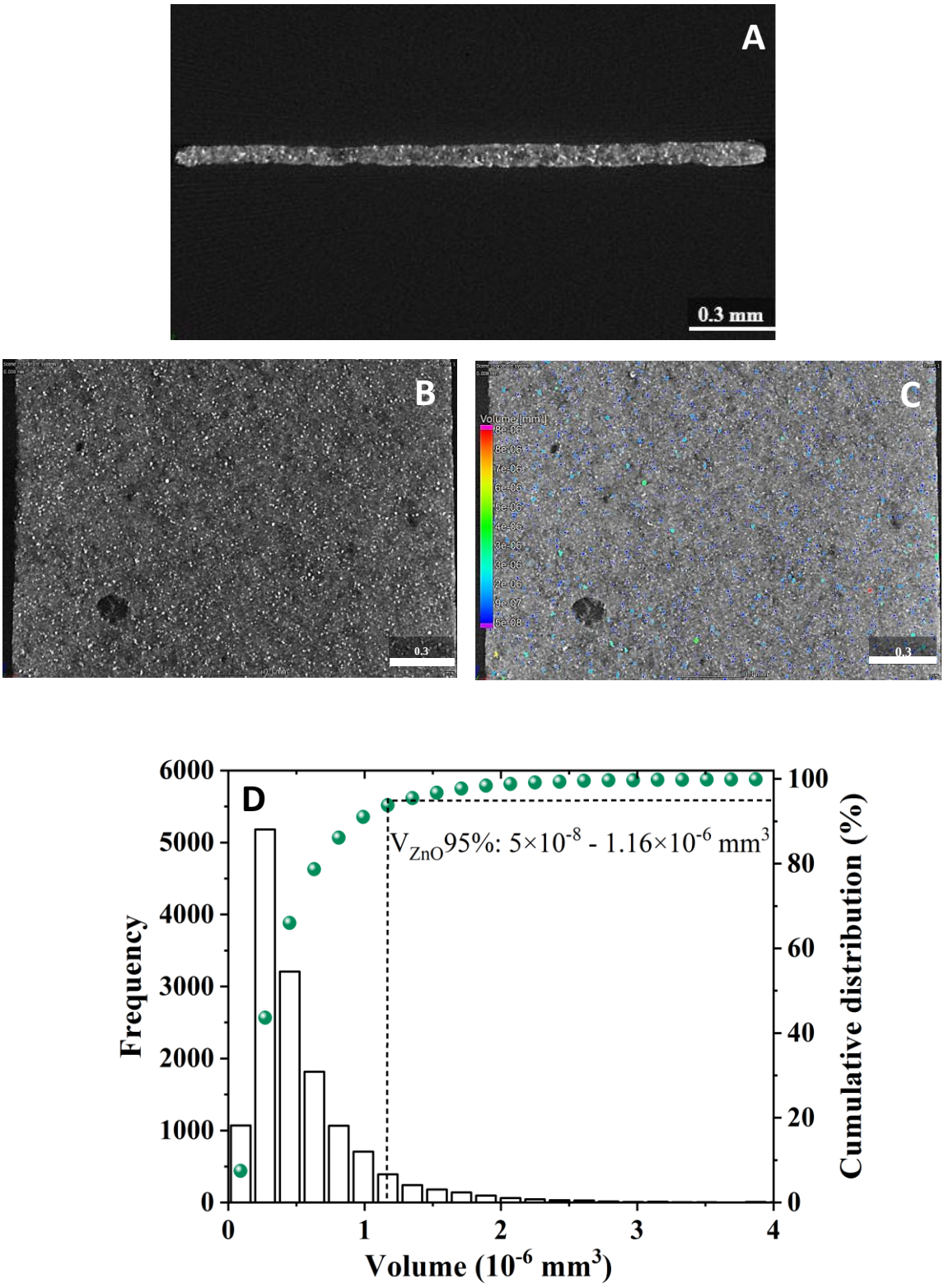

Figure 16. CT analysis of SOLVO 50 hybrid membrane: cross-section analysis (A); surface morphology (B), particle volume distribution (C and D)

The bright dots in Figure 16 B and C represent the homogeneous distribution of ZnO microcrystals on the surface of the hybrid membrane. The volume of the individual ZnO particles was also determined in the full 3D extension of the sample (Figure 16 C). It was found that 95 % of the ZnO microparticles have a volume from 5×10^{-8} mm^3 to 1.16×10^{-6} mm^3 in the case of both types of SOLVO membranes (Figure 16 D). Presumably, these ZnO microcrystals could play an important role in the photocatalytic decomposition of organic dyes and/or bacteria as larger photoactive centers. It is clear that ZnO particles in the micrometer range have significantly higher volume than ZnO nanoparticles; consequently, increased photocatalytic performance can be assumed by applying SOLVO membranes.

3.3.2. XRD, Raman spectroscopy, MIP, and BET analysis

To convert the amorphous phase of ZnO into crystalline, the composite additives were annealed at 400°C for 4 h before usage for the modification of BC. The diffraction peaks at 2θ of 26.5° and 44° can be assigned to the graphite structure of MWCNT (Figure 17 A, black curve). The characteristic peak of BC (Figure 17 A, red curve) existed at 2θ of 14.5°, 16.4°, and 22.5°, referring to the diffraction plane (101) (amorphous region), $(10\bar{1})$ (amorphous region) and (200) (crystalline region), respectively [163,154]. In agreement with Crystallography Open Database No. 9004178, diffraction peaks at 2θ of 31.7°, 34.5°, 36.1°, 47.5°, 56.7°, 62.8°, and 67.9° correspond to the (100), (002), (101), (102), (110), (103) and (200) planes, respectively, reflections of hexagonal ZnO (Figure 17 A, blue curve) [164]. They are present in the diffractograms of ZnO-containing additive (Figure 17 A, purple curve) as well as in the IMP 20 and SOLVO 20 hybrid membranes (Figure 17 A, green and deep blue curves, respectively).

Particle size was calculated from the XRD results, utilizing Rietveld refinement in Bruker TOPAS4, given as weight mean column length. The average particle diameter of ZnO crystallites is 20 ± 5 nm in the IMP hybrid membranes, whereas it was 260 ± 58 nm when the solvothermal method was applied for the preparation. Based on the particle size analysis and the SEM study (Figure 14 E, F) presented above, it can be assumed that ZnO crystallites form larger (4–5 μm) particles of hexagonal structure in SOLVO hybrid membranes than in membranes prepared by the impregnation method.

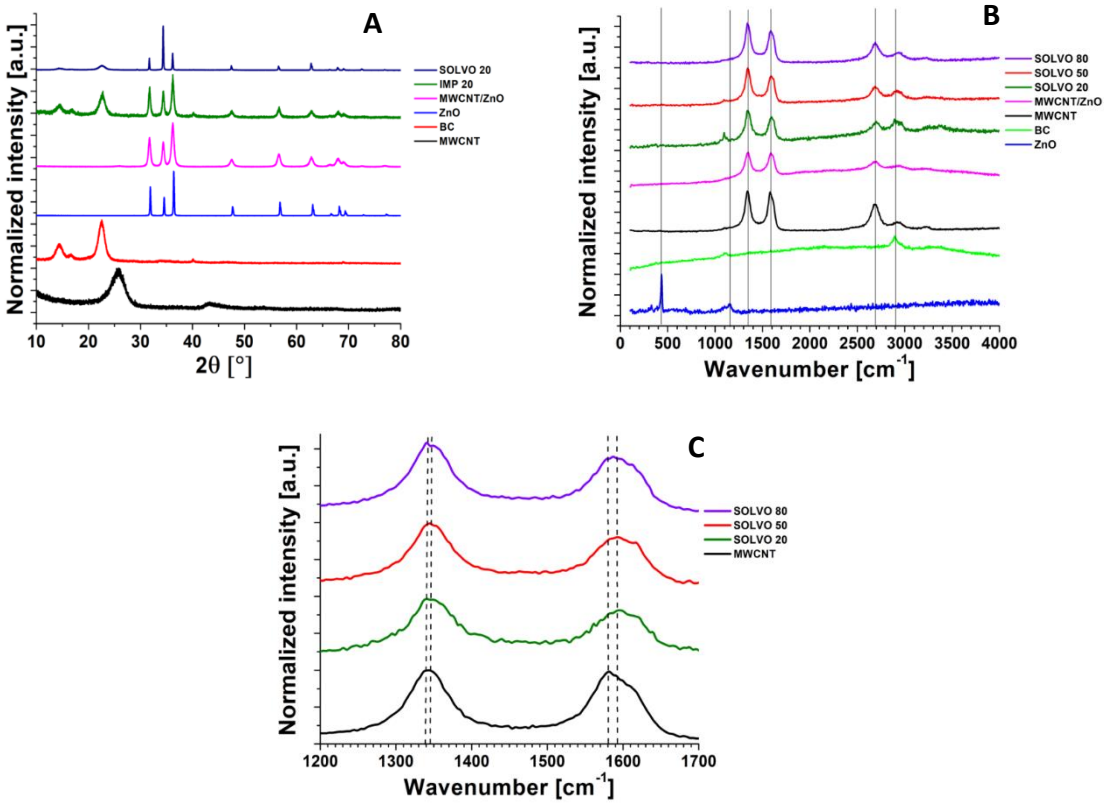

Figure 17. XRD (A) and Raman spectra (B,C) of pure materials (BC, ZnO, and MWCNT), ZnO-MWCNT additives, and BC-based hybrid membranes

The lattice parameters of ZnO were determined during Rietveld refinement, values for the impregnated samples are on average a = 3.251 ± 0.001 Å and b = 5.210 ± 0.002 Å, while the solvothermal synthesis shows a = 3.250 ± 0.001 Å and b = 5.207 ± 0.001 Å. The theoretical lattice parameters (COD 9004178) are a = 3.249 Å and b = 5.203 Å, in good agreement with the refined values. In order to confirm the chemical interaction between BC and ZnO-MWCNT composite additives, Raman spectra of the pristine materials (BC, MWCNT, and ZnO) and hybrid membranes were recorded (Figure 17 B, C). The characteristic peaks of ZnO can be distinguished at 438 and 1156 cm^{-1} (Figure 17 B, blue curve). The green curve in Figure 17 B shows peaks at 1105 and 2897 cm^{-1}, which are the characteristic bands of BC. Increasing the amount of the composites, the intensity of the two bands of BC diminished considerably, and the peaks became nearly invisible in the case of hybrid membranes with high ZnO-MWCNT content. Three other principal peaks originating from MWCNT (Figure 17 B, black curve) appear at 1339, 1580, and 2683 cm^{-1}. They are attributed to the D-, G- and G′-bands of MWCNT, respectively. By determining the ratio of these bands, the purity of the MWCNT samples can be efficiently determined [165]. As can be

seen in Figure 17 C and Table 6, notable differences were not distinguished by comparing the intensity ratios of D/G, G′/G, and D/G′, showing that the structure of the composite additive was not destroyed during the membrane preparation procedure [166]. The D-band is attributed to disorder provoked by defects and curvature in the nanotube lattice; the G-band is the in-plane vibration of the C–C bonds, while the G′ band is the overtone of D-band [167]. Moreover, in Figure 17 C, an up-shift in both D-band (from 1339 to 1345 cm^{-1}) and G-band (from 1580 to 1592 cm^{-1}) was witnessed in the spectra of hybrid membranes. This aspect could be described by the formation of non-covalent interactions, likely hydrogen bonds, between the MWCNT and BC fibers, resulting in a slight band shifting [170]. According to the relative pore volume histograms (Figure 19), the membranes prepared by the impregnation technique has a wider pore size distribution range. As shown in Figure 19, most pores are in the range of 10 μm to 100 μm in all membranes. By comparing the hybrid membranes, it can be concluded that the average pore size of SOLVO membranes is significantly higher than that of IMP membranes.

Table 6. Summary of the ratios of D, G, and G' peaks

	MWCNT	**SOLVO 20**	**SOLVO 50**	**SOLVO 80**
I_D/I_G	1.02	1.04	1.05	1.04
$I_{G'}/I_G$	0.89	0.97	0.96	0.96
$I_D/I_{G'}$	1.14	1.07	1.09	1.08

The pores that are larger than 10 μm occupied a cumulative pore volume of about 77.0 % and 97.0 % for SOLVO 50 and SOLVO 80, respectively. Moreover, the SOLVO 80 membrane possesses a relatively narrow PSD with the highest relative pore volume at 98.8 μm, while SOLVO 50 shows a wider PSD with 2 larger peaks at 0.008 μm and 0.085 μm.

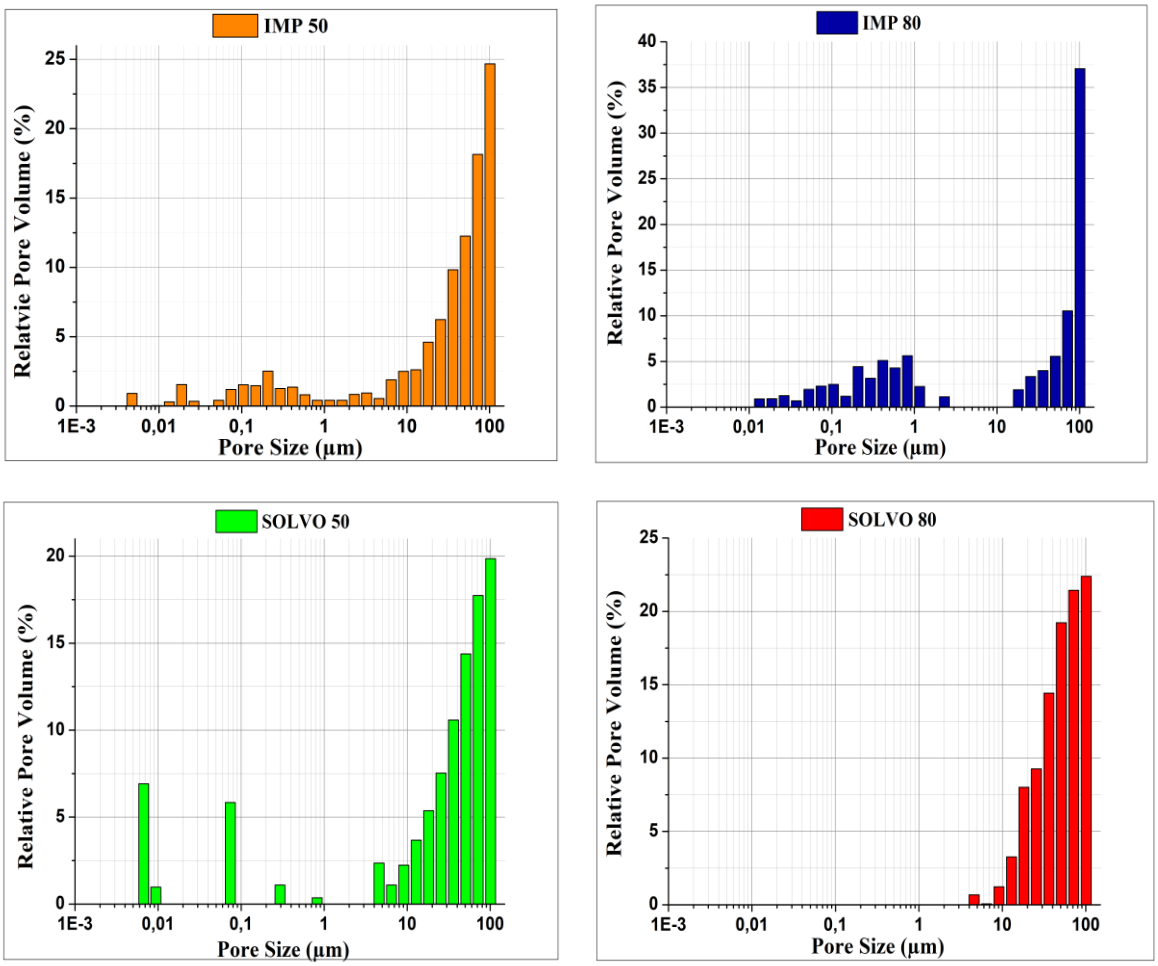

Figure 18. Pore size distribution analysis of hybrid membranes

In the case of IMP samples, the peaks shifted towards the smallest pores, and the number of pores below 10 µm has been increased, in particular those under 1 µm. Based on the pore size distribution analysis, we assumed that the as-prepared hybrid membranes are suitable for filtration and adsorption experiments.

As the results in Table 7 reveal, the specific surface area of BC membranes dried from a water-swollen state was found to be about 0.8 $m^2 g^{-1}$. A similar value was obtained for cotton (1 $m^2 g^{-1}$) also dried from a water-swollen state [168], and a slightly higher value (2.7 $m^2 g^{-1}$) was measured for BC [169]. The commercial MWCNT has a very high specific surface area (302 $m^2 g^{-1}$) also determined by nitrogen sorption.

Table 7. The specific surface area determined by nitrogen of the raw materials, composite additives, and BC-based hybrid membranes

Sample	Specific surface area ($m^2 g^{-1}$)
MWCNT	302
CTAB-MWCNT	-
ZnO	50
BC	1
IMP 10	3
IMP 20	6
IMP 50	13
IMP 80	21
IMP 90	25
SOLVO 10	13
SOLVO 20	17
SOLVO 50	25
SOLVO 80	33
SOLVO 90	36

However, for composite additives where the MWCNT is incorporated with ZnO, the values are significantly lower and depend mainly on the preparation methods (IMP: 27 $m^2 g^{-1}$; SOLVO: 48 $m^2 g^{-1}$). Thus, the surface area of hybrid membranes is higher than that of the BC and lower than that of the composite additives.

3.3.3. DLS and contact angle measurement

Zeta potential (ζ) was measured in a pH range of 3.0 - 9.0 for the hybrid membranes and raw materials, and the results are presented in Figure 19. The samples were dispersed in distilled water to reach the final concentration of 0.1 wt % before starting the experiments. HCl or NaOH diluted solutions (0.1 M) were used in order to adjust the pH. Each measurement was repeated three times.

The pure BC showed a negative zeta potential, whereas the CTAB treated MWCNT and ZnO are positively charged in the chosen pH range. Modification of BC with ZnO-MWCNT composite additives shifts their isoelectric point (IEP) towards higher values (the surface becomes more positively charged). By comparing the results for each pH, it can be concluded that the ζ of hybrid membranes of both series is increasing continuously with increasing the amount of the ZnO-MWCNT composite additive.

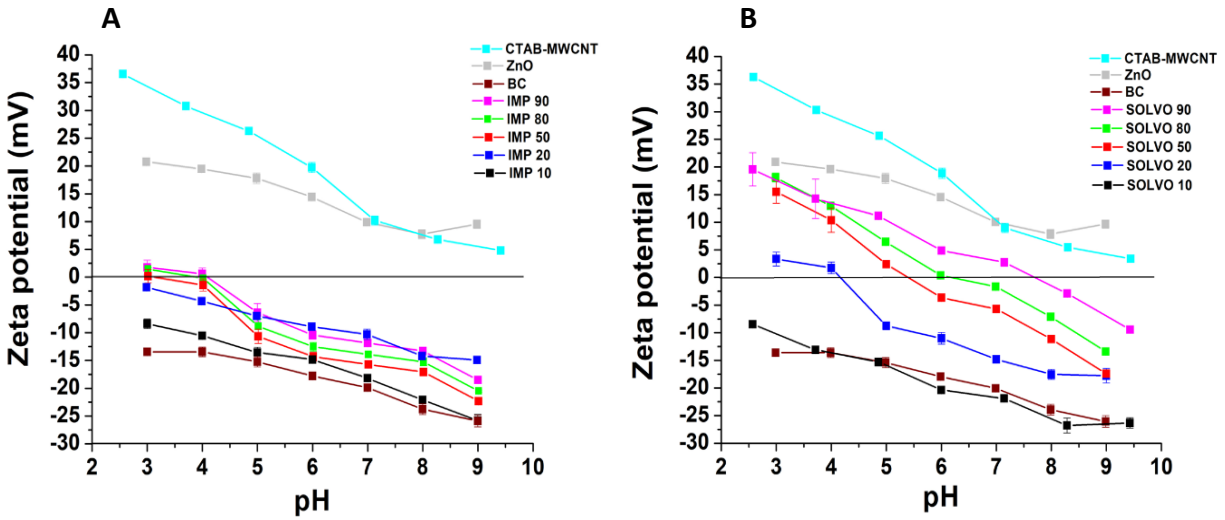

Figure 19. Zeta potential of raw materials: IMP (a) and SOLVO (b) hybrid membranes as a function of pH.

It can also be ascertained that the SOLVO hybrid membranes have significantly higher IEP values (Table 8) than the IMP hybrid membranes in the selected pH range and at the same ZnO-MWCNT additive content. Based on the obtained results from the BET and DLS measurements we realized that samples containing 10 % of additives their BET surface area values and IEP values were low and not promising, on the other hand the samples containing 90 % of additives we unstable and this was the reason that we focused on samples of 20 %, 50 %, and 80 %.

The surface hydrophilicity/hydrophobicity of the membranes was also characterized by water contact angles. Results reveal that the contact angles of IMP membranes were in the range of 36-42° (Figure 20 A-C), the surface is hydrophilic, and the effect of additive content is negligible. It is evident that SOLVO membranes exhibited higher water contact angles than IMP membranes. The contact angle changed from 77° to 136° (Figure 20 D-F) depending on the membrane

composition. Consequently, the hydrophilic surface of the as-prepared hybrid membranes can be easily influenced by incorporating different amounts of ZnO-MWCNT additive prepared by the solvothermal method into the BC network.

Table 8. Isoelectric points (IEP) of the raw materials, composite additives, and BC-based hybrid membranes

Sample	IEP (pH)
MWCNT	4.2
CTAB-MWCNT	> 9
ZnO	> 9
BC	< 3
IMP 10	< 3
IMP 20	< 3
IMP 50	3.2
IMP 80	4.0
IMP 90	4.2
SOLVO 10	< 3
SOLVO 20	4.4
SOLVO 50	5.5
SOLVO 80	6.2
SOLVO 90	7.5

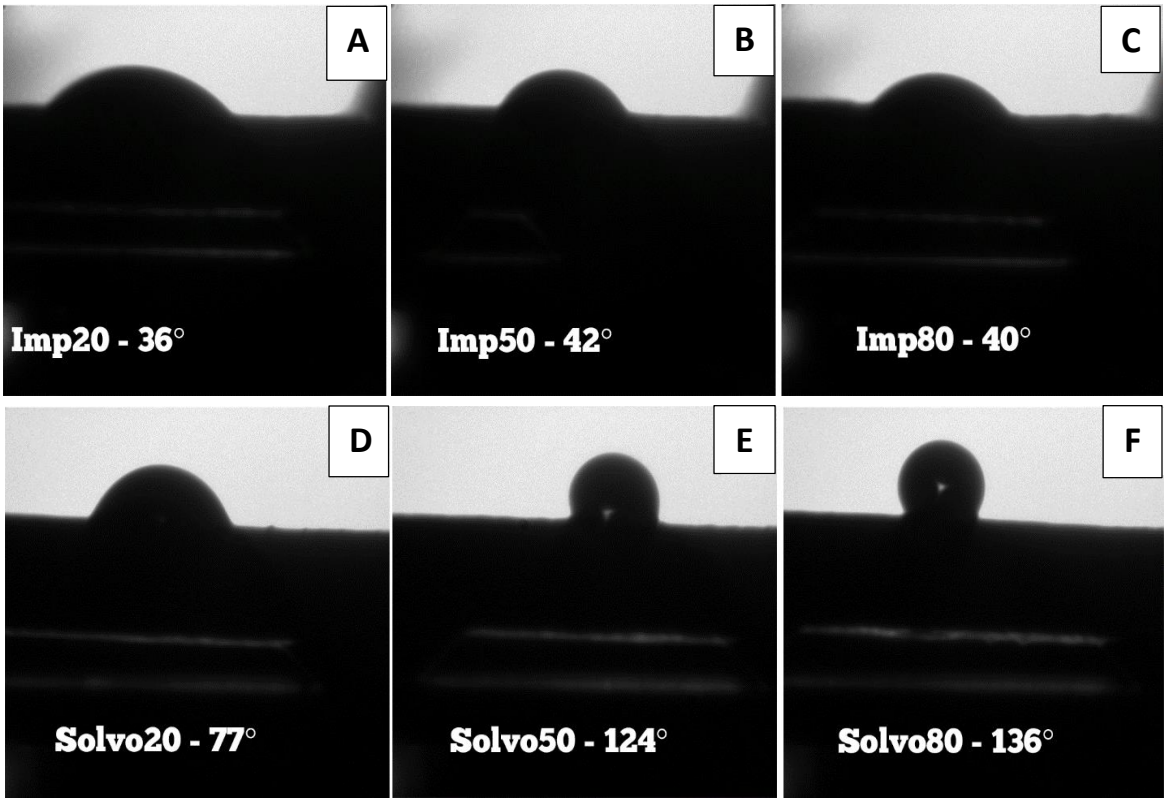

Figure 20. Photomicrographs of a water drop with contact angle values measured on the surface of IMP (A-C) and SOLVO (D-F) hybrid membranes

3.3.4. Color and water vapor absorption capacity measurements

Smooth, flexible, and grey membranes with a thickness of about 40-60 μm are presented in Figure 21. It was evident that the color varies from light to dark grey depending on both the amount of the concentration of the composites added and on the preparation method. As the data in Table 9 reveals, the white color of the BC matrix has changed significantly; the lightness decreased with increasing additive concentration, and the color difference based on the standard white tile of colorimeter ranged from 31 to 48 and from 50 to 65 for IMP and SOLVO membranes, respectively.

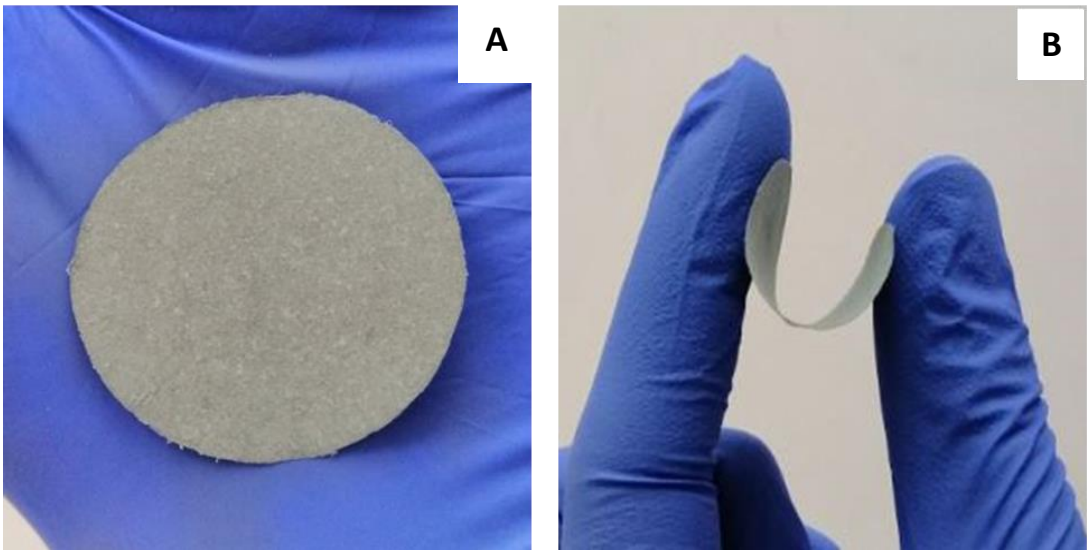

Figure 21. Representative photographs of SOLVO 20 hybrid membranes presenting the color (A) and flexibility (B)

Table 9. Lightness, color difference values, and water vapor sorption capacity of BC and BC-based hybrids membranes

Sample	Lightness (L)	Color difference[a] (ΔE_{ab})	Water sorption capacity[b] (%)
IMP 20	63 ± 2	31 ± 2	5.66 (7.07)
IMP 50	50 ± 1	45 ± 1	3.03 (6.06)
IMP 80	46 ± 3	48 ± 3	1.68 (8.40)
SOLVO 20	44 ± 4	50 ± 4	4.67 (5.83)
SOLVO 50	34 ± 6	61 ± 6	1.73 (3.46)
SOLVO 80	29 ± 2	65 ± 2	1.89 (9.45)
BC	-	-	7.87

[a] Based on the standard white tile of colorimeter
[b] Values in parentheses: calculated on the cellulose content of the membrane

The water vapor sorption capacity of the pure cellulose is around 8.0 [172]. BC is also a good absorbent, and a relatively similar value was obtained for the neat BC membrane (Table 9, 7.87%). For hybrid BC-based membranes, however, the water sorption decreased with increasing the additive content. Furthermore, due to the more pronounced hydrophobicity, the SOLVO

membranes displayed slightly lower water sorption than the more hydrophilic IMP membranes. Besides, water sorption data were also calculated relative to the amount of cellulose in each membrane (Table 9, data in brackets). Interestingly, both membranes with an additive content of 80 absorbed significantly more water vapor (8.40 and 9.45%) than the original BC membrane. A possible explanation of this behavior is that the additive is also accessible to a certain extent of water vapor.

3.3.5. Tensile strength, tear elongation, and electrical conductivity measurements

BC membranes exhibit excellent tensile strength (57 MPa; Table 10) with a sufficient elasticity (about 5% elongation) due to the strong hydrogen-bonding structure of cellulose molecules. The addition of the ZnO-MWCNT additive to BC disrupts this compact and firm structure. For both types of membrane, the tensile strength decreased significantly even at low additive content of 20.

Table 10. Mechanical and electrical properties of BC and BC-based hybrid membranes

Sample	Thickness (µm)	Tensile strength (MPa)	Elongation at break (%)	Electrical conductivity (S cm^{-1})
IMP 20	43	16.3 ± 1.9	4.6 ± 1.4	6.1×10^{-5}
IMP 50	63	4.6 ± 0.6	2.4 ± 0.7	2.3×10^{-4}
IMP 80	65	1.1 ± 0.5	1.7 ± 0.5	1.2×10^{-1}
SOLVO 20	38	13.0 ± 2.6	6.1 ± 1.6	3.1
SOLVO 50	48	0.9 ± 2.6	2.6 ± 0.3	30.5
SOLVO 80	42	6.7 ± 1.7	3.0 ± 0.2	140.1
BC	37	56.8 ± 6.8	4.8 ± 2.0	-

However, the structure of as-prepared membranes is still relatively stable and resilient, as can be seen in Figure 21 B. It is well-known that carbon nanotubes are often used as conductive filler coating materials [65]. The addition of MWCNT to the BC contributes to improving the electrical properties of cellulose/MWCNT composite. The conductivity of the MWCNT-incorporated cellulose was (1.4×10^{-1} S cm^{-1}), based on the total cross-sectional area, containing 9.6 w/w% of MWCNT [164]. A similar value (1.2×10^{-1} S cm^{-1}) was measured for the IMP 80 membrane (Table 10). By comparing the electrical conductivity values of the different membranes, it can be concluded that the BC-based hybrid membranes synthesized by the solvothermal method have

significantly higher electrical conductivity for each composition than those prepared by the impregnation technique. The values of SOLVO membranes increased from 3.1 to 140.1 S cm^{-1} with increasing the additive content. However, for IMP membranes, the values were in a significantly lower range ($6.1 \times 10^{-5} – 1.2 \times 10^{-1}$ S cm^{-1}). Consequently, the electrical conductivity of as-prepared membranes can be tailored by the appropriate synthesis method.

3.3.6. Adsorption properties and photocatalytic decomposition of methylene blue

The Langmuir isotherm models (Figure 22) were used to describe the equilibrium characteristics of the methylene blue (MB) adsorption. The Langmuir is defined by the following equation:

$$q_e = \frac{q_m \times K_L \times c_e}{1 + c_e \times K_L}$$

Where q_e is the amount (mmol/g), while c_e is the equilibrium concentration of MB in the solution (mmol/L), q_m is the maximum sorption capacity (mmol/g), and K_L is the Langmuir equilibrium constant (L/mg). K_L and q_m can be calculated with nonlinear regression.

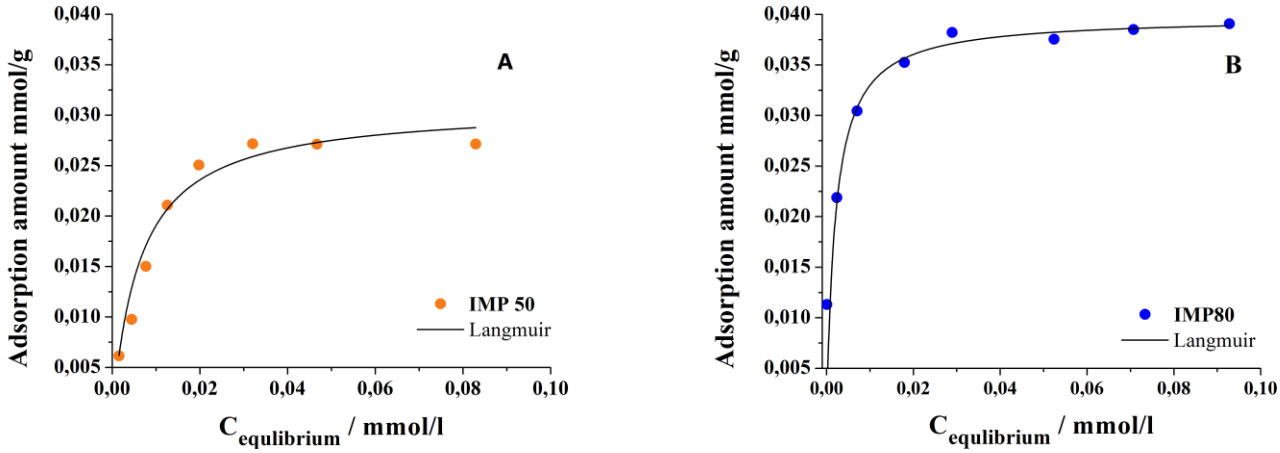

Figure 22. Adsorption isotherms of IMP 50 (A) and IMP 80 (B) hybrid membranes

Sample	q_m (mmol/g)	K_L (L/mg)	R^2
IMP 50	0.031 ± 0.001	160.8 ± 35	0.9982
IMP 80	0.040 ± 0.0004	488.6 ±63	0.9997

Table 11. The calculated Langmuir adsorption parameters

The parameters obtained from the fitted isotherms are shown in Table 11. The correlation coefficients (R^2) are close to 1 in both cases, so the isotherms fit well with the results. According to the results, the maximum adsorption capacity (q_m) was higher for IMP80 (0.040 mmol/g) than for IMP50 (0.031 mmol/g).

The photocatalytic degradation performance of the membranes prepared by two different methods was investigated using MB as a targeted pollutant to support the photodegradation efficiency of the as-prepared membranes. The highest degradation was achieved by the membrane SOLVO 80 with a removal efficiency of 92% after 120 minutes under UV light, as can be seen in Figure 23 (red curve), followed by 78% decomposition of MB by SOLVO 50 membrane, Figure 23 (green curve).

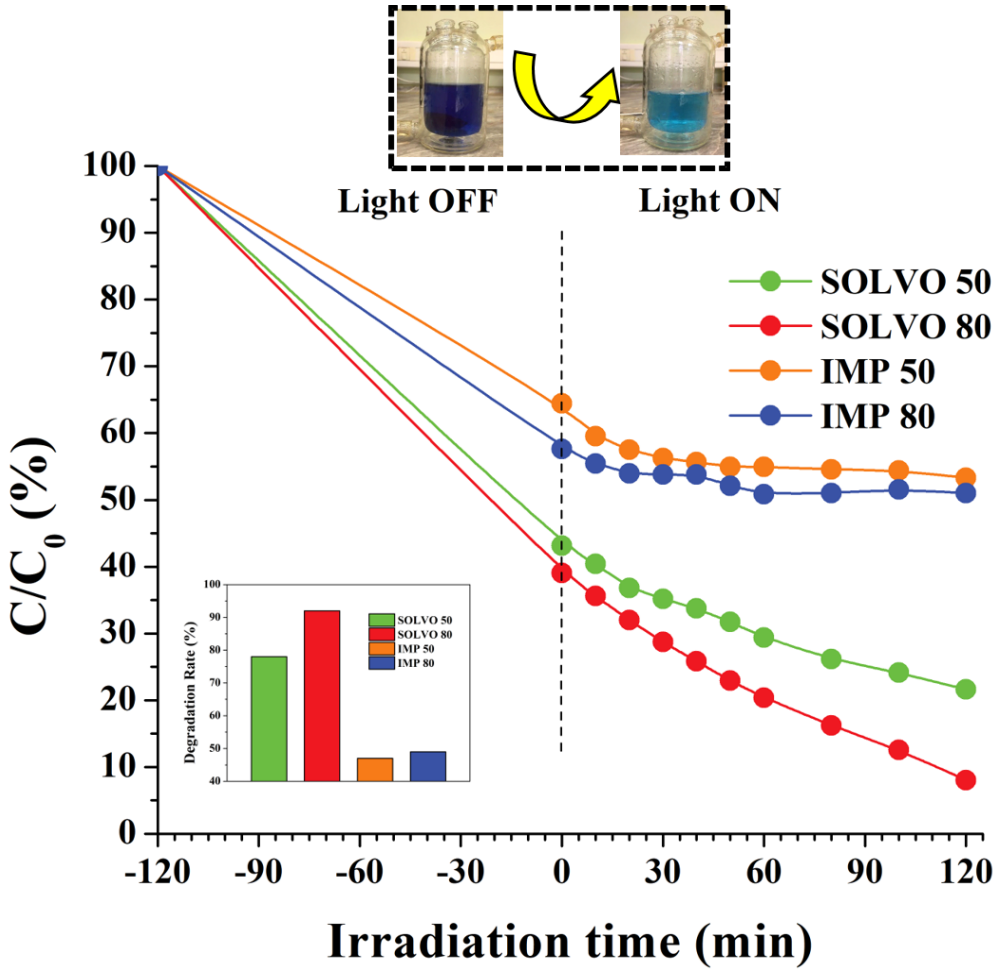

Figure 23. The photocatalytic degradation rate of MB over the different hybrid membranes under UV irradiation

However, the lowest degradation efficiencies were achieved by the membranes prepared *via* impregnation technique with the overall removal efficiency of 47 % and 49 %, for IMP 50 and IMP 80 (Figure 23 orange and blue curves), respectively. Apparently, the membranes with higher ZnO-MWCNT content (80 %) resulted in higher adsorption capacity for MB. The higher activity of the SOLVO membranes can also be explained by the higher specific surface areas than the impregnated membrane version. It means that the solvothermal method resulted in materials with higher removal efficiencies compared to the ones prepared *via* the impregnation method.

MWCNT is well-known for their high adsorption and good electron acceptor properties [170]. Both the MWCNT and bacterial cellulose are possessing remarkable physicochemical and mechanical properties, which provide superior performance via synergistic effects after combining. Furthermore, the photocatalytic degradation of MB can be explained by the electron transfer process from the ZnO particles to MWCNT. Carbon nanotubes act as a photogenerated electron acceptor to promote interfacial electron transfer processes from the ZnO particles to the MWCNT. Moreover, the bacterial cellulose, in addition, has hydroxyl groups in abundance on its surface, which may also act as a charge carrier, further improving the catalytic performance of the hybrid membranes. The enhanced photocatalytic activity of BC-ZnO-MWCNT SOLVO membranes denotes that a good interfacial combination exists between ZnO nanoparticles and the MWCNT in the as-prepared composites [171].

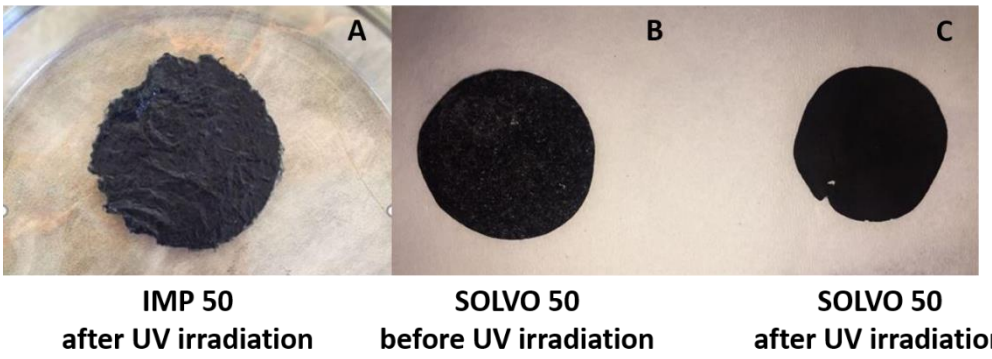

Figure 24. Membrane degradation of IMP (A) and SOLVO (B and C) membranes before and after UV irradiation

The good photocatalytic performance of SOLVO membranes could be explained not only by the chemical bonds between the ZnO and MWCNT but also by the size and volume of ZnO

particles. The incorporation of ZnO-MWCNT-SOLVO additives into the BC matrix resulted in increased photoactivity of the hybrid membranes due to the presence of micrometer-sized ZnO particles, which can also be described as the photoactive center of MB degradation. The high removal and adsorption rates of the bacterial cellulose reinforced hybrid membranes prepared *via* solvothermal method indicates good adsorption and photocatalytic activity for MB and is likely to be an efficient photocatalyst. It was also observed during the experimental process that membranes prepared *via* the IMP method were less stable physically (see Figure 24 A) and started to become deformed after few minutes. Some loose threads-like fibrous parts of membranes were also observed during sample collection. On the other hand, membranes synthesized by the SOLVO method were not deformed and maintained their original physical state throughout the whole experiment (Figure 24 B and C).

3.3.7. *E. Coli* filtration experiment

Before starting the filtration tests, control experiments were performed without applying the as-prepared hybrid membranes to investigate the possible adsorption on the membrane holder of the funnel. This investigation revealed that there was no measurable *E. Coli* retention. During the first series of the measurement, BC-ZnO-MWCNT-IMP membranes, even at 50 w/w% BC content, were damaged due to the negative differential pressure. By comparing the membranes, it was found that SOLVO 80 showed significantly higher tensile strength (6.7±1.7 MPa) than IMP 80 (1.1±0.5 MPa). To avoid this phenomenon and to obtain comparative results, two superimposed membranes were applied in each filtration cycle. Applying this experimental setup, we were able to stabilize the membrane structure against the applied pressure (0.8 bar). As can be seen in SEM images in Figure 25 A and B, the *E. Coli* removal was successful using both IMP (Figure 25 A) and SOLVO (Figure 25 B) hybrid membranes. Rod-shaped *E. Coli* bacteria could be found in these SEM images with an average length of 2-3 μm. Moreover, it can also be observed that the cell wall of the *E. Coli* bacteria was damaged during the filtration. Thus, we assume that novel BC-ZnO-MWCNT hybrid membranes has not only good adsorption ability against *E. Coli* but also have some antibacterial activity. The antibacterial properties of cellulose/ZnO nanocomposite films [116] and the pure carbon nanotubes [172] have already been presented recently. Consequently, the perceived antibacterial effect can be attributed to the synergistic effect of the ingredients of hybrid membranes and the interactions between them.

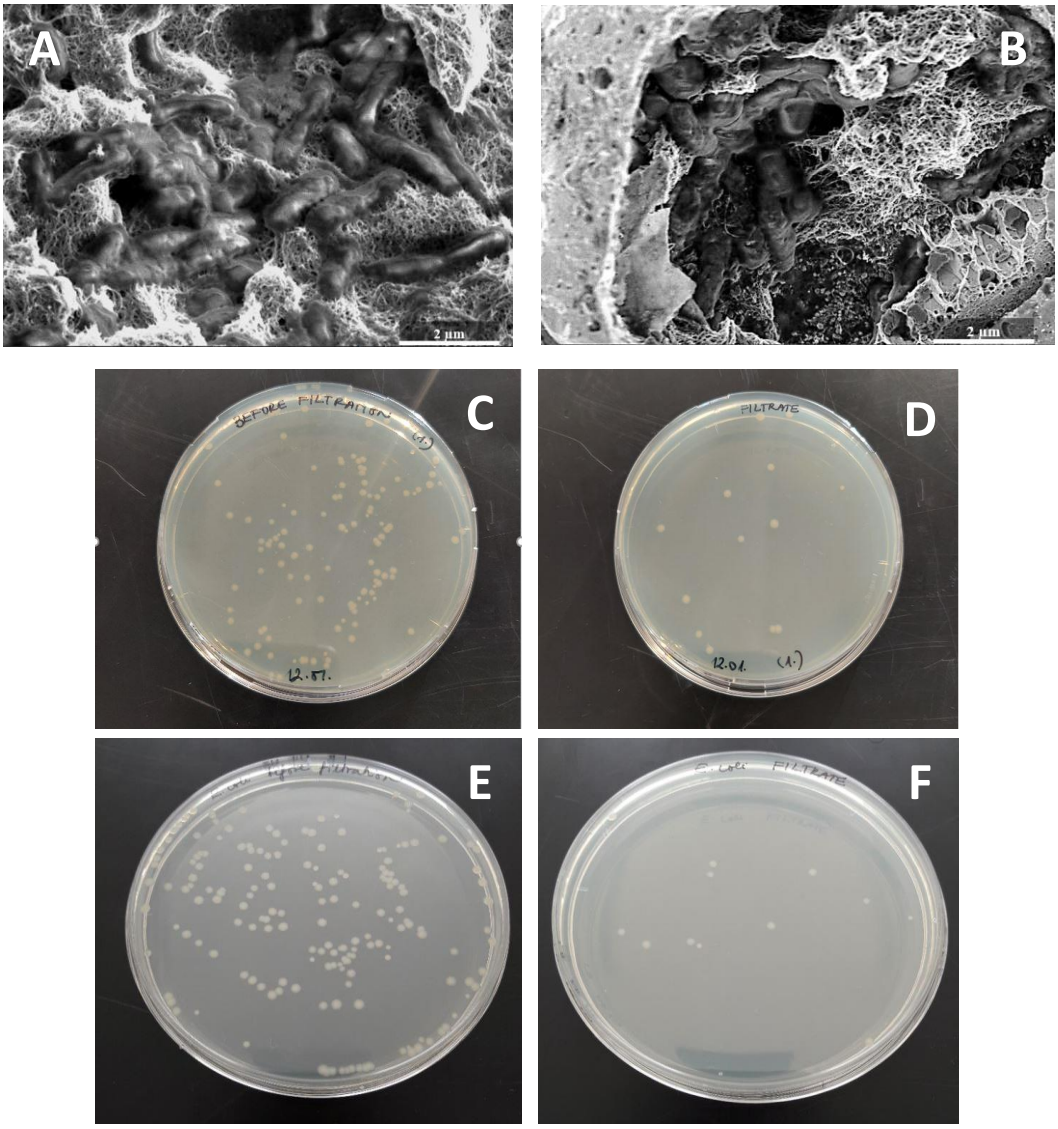

Figure 25. SEM images of IMP 50 (A) and SOLVO 50 (B) membranes after filtration. Photographs of *E. Coli* cultures after filtration with IMP 80 (C and D) and SOLVO 80 (E and F) membranes.

In both cases, the membranes containing 80 w/w % of ZnO-MWCNT additives showed significantly higher *E. Coli* removal than samples prepared using 50 w/w % of additives. Figure 25 C-F and Figure 26 present the removal efficiency of BC-ZnO-MWCNT hybrid membranes. It was found that the highest *E. Coli* removal was achieved by the membrane SOLVO 80 with an efficiency of 92% (Figure 25 F and Figure 26 red column).

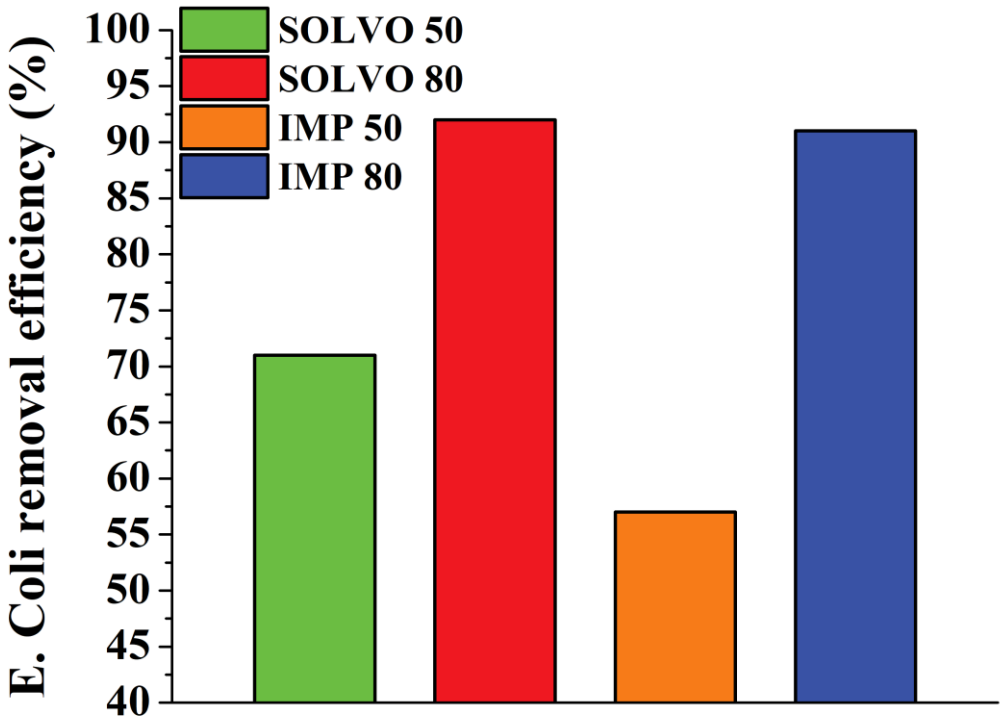

Figure 26. *E.Coli* removal efficiency (BFE%) of BC-ZnO-MWCNT hybrid membranes

IMP 80 membrane showed 91% adsorption of *E. Coli*, as can be seen in Figure 25 D and Figure 26 blue column. The lowest bacteria removal capacities were achieved by the membranes containing 50 w/w % ZnO-MWCNT additives with the overall removal efficiency of 71% and 57%, for SOLVO 50 and IMP 50 (Figure 26 green and orange column), respectively. Based on the results mentioned above, it was found that in terms of *E. Coli* removal, the amount of ZnO-MWCNT composite material incorporated into the hybrid membrane structures is more important than the size of ZnO particles. Furthermore, the outstanding filtration performance of IMP 80 and SOLVO 80 membranes indicates that the antibacterial properties of the membranes are mainly attributed to the ZnO-MWCNT additive and not to the bacterial cellulose, as was expected.

3.4. Characterization and application of the BC-Pt-NBCNT hybrid membranes

3.4.1. SEM and XRD analysis

The BC-reinforced Pt-NBCNT membranes were examined by scanning electron microscopy. The SEM image of the membrane shows the fibrous structure of the NBCNT and BC fibers (Figure 27 A). The formation of the fiber bundles is explained by interactions between the surface functional groups of BC and NBCNT [165]. The oxygen contained functional groups - hydroxyl groups (-OH) - of the NBCNT and BC surfaces was able to form hydrogen bonds, which provided for the adsorption of NBCNT on the surface of the BC fibers. The nitrogen-doped carbon nanotubes contain several incorporated nitrogen atoms, which contributed to anchoring on the cellulose surface. At higher resolution (Figure 27 B, C), the Pt nanoparticles are visible in a homogenous distribution on the nanotube surface, which is thoroughly examined by bright-field and high-angle annular dark-field imaging in STEM mode (Figure 27 D, E). The average particle sizes of Pt nanoparticles were not affected by the presence of NBCNT and BC during the nanocomposite synthesis procedure, and aggregation or bigger particles could not be observed in the structure of hybrid membranes.

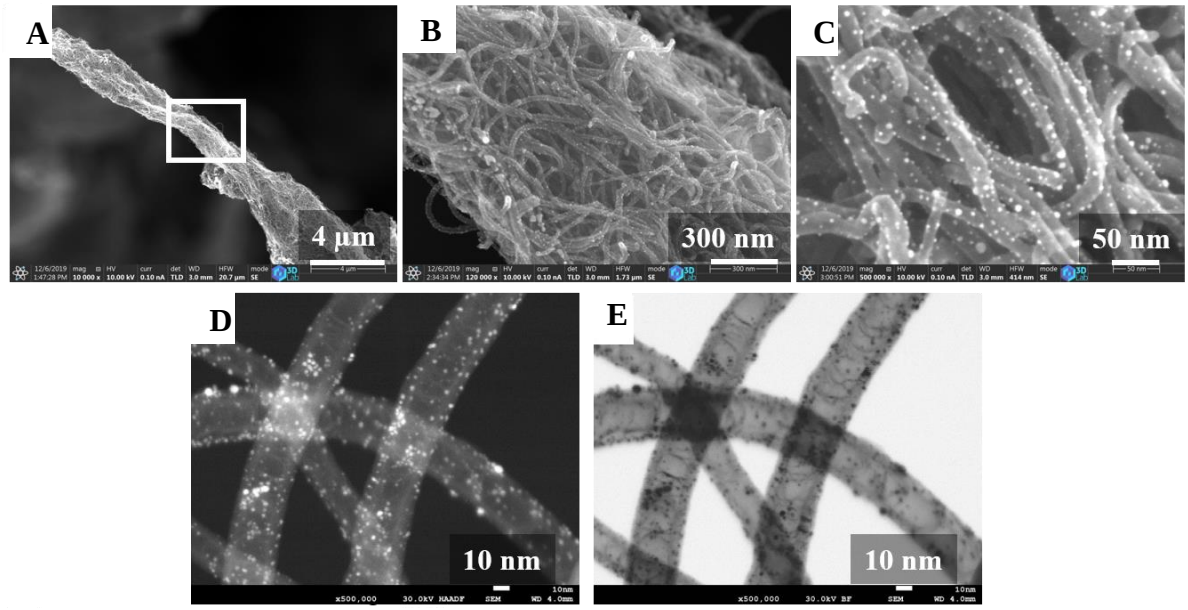

Figure 27. SEM images (A, B, C), bright-field (D) and high-angle annular dark-field (E) STEM images of the BC-Pt-NBCNT membrane

The presence of elemental platinum on the membrane surface was validated by XRD measurements. On the diffractograms, the visible peaks belong to the reflections of the Pt (111), Pt (200), Pt (220), and Pt (311); these are found at 39.9; 46.6; 67.6; 81.3 two Theta (2θ) angles, respectively (Figure 28). The appearance of the Ni (111) reflection is explained by the catalyst left after the NBCNT preparation. A small number of nickel nanoparticles were embedded in the structure of the NBCNT and could not be removed. The carbon sheets of NBCNT prevented the dissolution of nickel in hydrochloric acid during the purification step. The C (002) peak confirms the presence of carbon nanotubes.

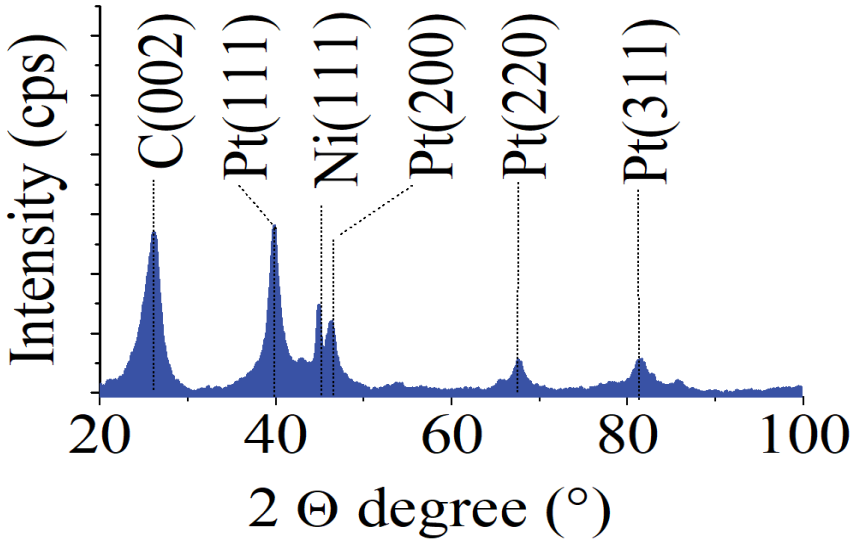

Figure 28. XRD pattern of the BC-Pt-NBCNT membrane

3.4.2. EDAX, particle size distribution, FTIR analysis and BET measurements

The bands of platinum, nickel, and carbon were also located on the EDAX spectrum (Figure 29). In the case of the platinum nanoparticles, high dispersion was detected and the measured average diameter was 3.0 ± 1.6 nm (Figure 30). The vast majority of the nanoparticles, namely 95%, were smaller than 3.3 nm, the smallest diameter was 1.8 nm, but a few nanoparticles had a size between 8 and 10 nm. The particle distribution approximates a homo-dispersal system. Based

on these results, we can conclude that applying the BC-NBCNT support allowed the formation of the small particles.

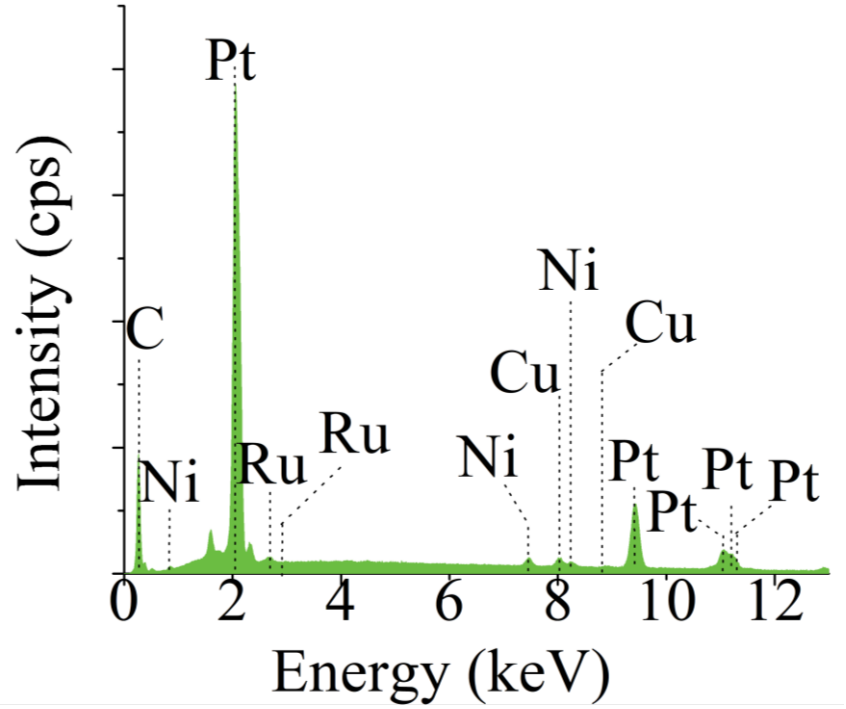

Figure 29. EDAX spectrum of the BC-Pt-NBCNT membrane

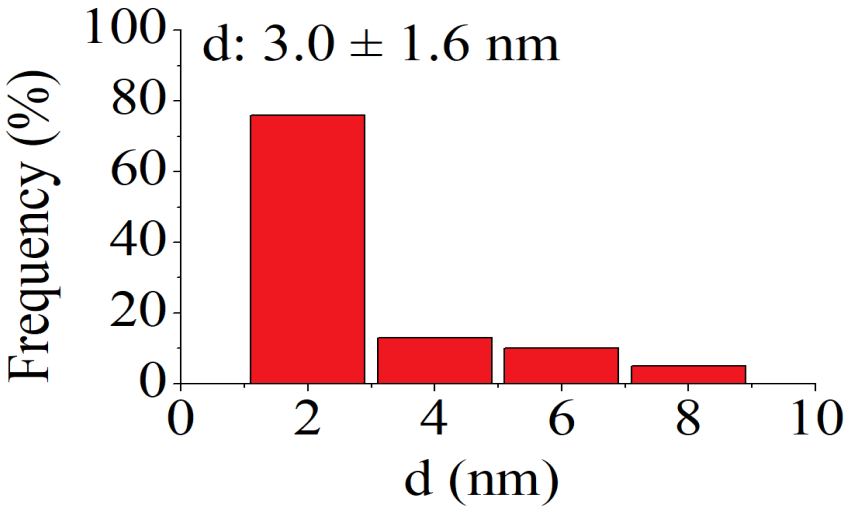

Figure 30. Particle size distribution of the BC-Pt-NBCNT membrane

The surface functional groups of the BC and NBCNT were identified by FTIR spectroscopy (Figure 31). Vibration bands of the C-O stretching are found on the spectrums at 1223 cm^{-1} (NBCNT) and at 1059 cm^{-1} (BC). Bending vibration of the hydroxyl groups results in a peak at 1431 cm^{-1} in the case of NBCNT and at 1413 cm^{-1} on the spectrum of BC. The adsorption peak at 1574 cm^{-1} can be attributed to the C=C bands on the spectra of NBCNT, which corresponds to the vibration of the lattice structure of the NBCNT. The peak located at 1590 cm^{-1} belongs to the vibration mode of water molecules absorbed in BC [173]. At the 1713 cm^{-1} wavenumber, the band corresponds to the carboxyl (COOH) groups on the NBCNT. The peaks around 2889 cm^{-1} and 2952 cm^{-1} are attributed to the symmetric and asymmetric C-H stretching vibration. The intensive peak at 3455 cm^{-1} on the spectrum of NBCNT belongs to the -OH stretching vibration. The band at 3414 cm^{-1} in the case of cellulose is characteristic of the stretching vibration of the hydroxyl group in polysaccharides; furthermore, it also includes the inter- and intra-molecular hydrogen bond vibrations in BC [174, 175].

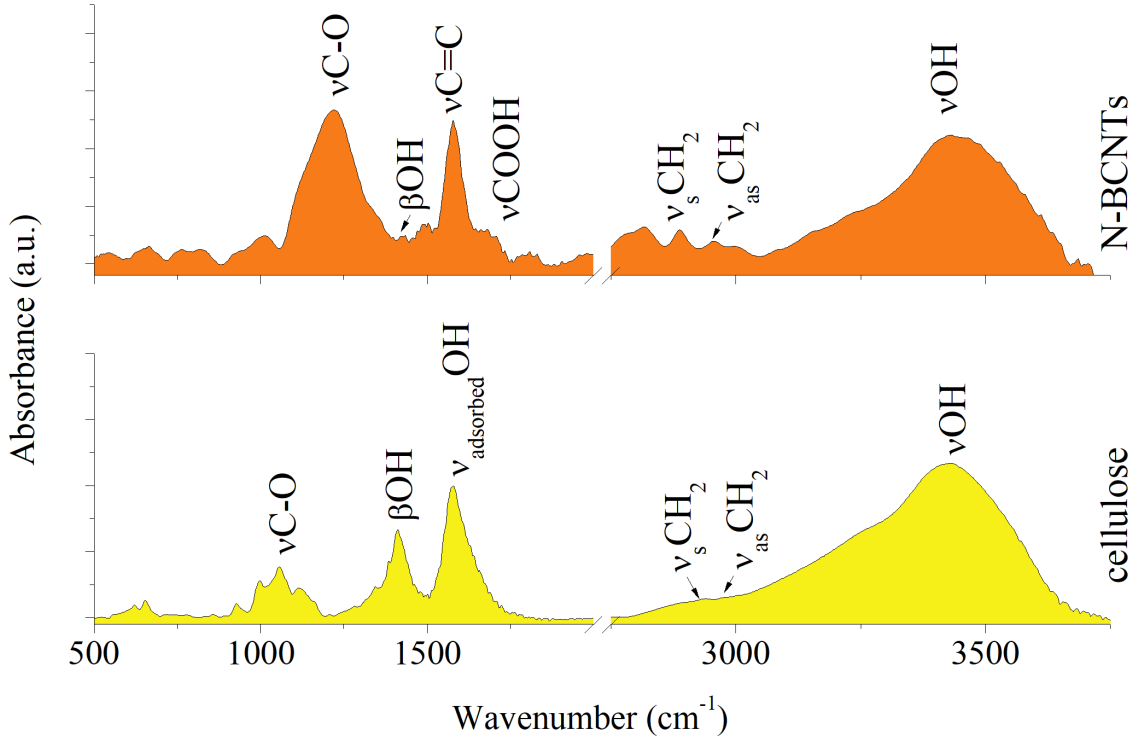

Figure 31. FTIR spectrum of the nanocrystalline cellulose fibers and the NBCNT

Several -OH groups are found on the NBCNT and BC fibers, which could make interactions and lead to the formation of hydrogen bridges. These facilitate formed the fibers into bundles, as seen in the SEM image (Figure 27 A). A further advantage of the functional groups containing oxygen is that they may regulate the particle size of catalytically active metals during catalyst preparation. Moreover, the ion-binding effect of the oxygen-containing groups (electric interaction, ion exchange, surface complexation interactions) should not be forgotten.

The as-prepared NBCNT-based membranes were also characterized by the N_2 adsorption technique to measure their specific surface area. The BET surface area values of raw materials and hybrid membranes can be seen in Table 12. It can be concluded that the addition of support material slightly reduces the surface area from 146 to 110 m^2/g. However, a significant difference in the surface area values measured before and after the catalytic reaction cannot be measured.

Table 12. Summary of BET surface area values of raw materials and BC-Pt-NBCNT membranes

Sample name	BET surface area (m^2/g)
NBCNT	146
BC	1
BC-Pt-NBCNT	110
BC-Pt-NBCNT (used 1)	107
BC-Pt-NBCNT (used 2)	109

3.4.3. Catalytic hydrogenation of 1-butene

To determine the catalytic activity of the BC-Pt-NBCNT hybrid membranes, 1-butene hydrogenation was tested in a continuous flow system (Figure 32), coupled to the gas cell of the FTIR equipment. Before the experiments, the FTIR instrument was calibrated by using an H_2/N_2/1-butene gas mixture, applying four different 1-butene concentrations at room temperature and atmospheric pressure. For each measurement, two-hybrid membranes with a weight of 100 mg were used. The applied gases' flow rates were 40 mL/min (N_2, H_2) and 20 mL/min (1-butene) at atmospheric pressure.

The reaction temperature was set at 50 °C, and the molar ratio of the hydrogen to 1-butene was 2:1. The catalytic performance of BC-Pt-NBCNT hybrid membranes was determined by the conversion (X%) of 1-butene using the equation below:

$$X\%_{1-butene}\frac{consumed\ n_{1-butene}}{initial\ n_{1-butene}} \times 100$$

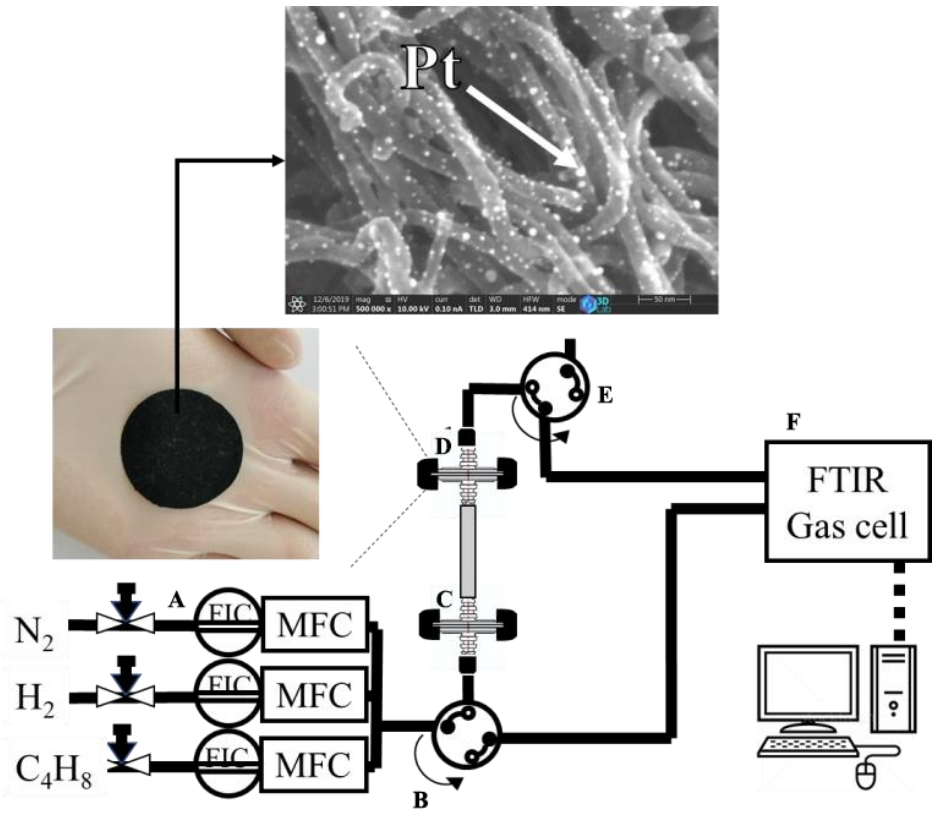

Figure 32. Experimental setup of catalytic hydrogenation of 1-butene. (A) - values for the gases (N_2, H_2, C_4H_8), (B, E) - four-way valve for a gas inlet into the reactor and the FTIR gas cell, (C, D) - membrane holders, (F) - FTIR instrument connected to a computer.

For the confirmation of the BC-Pt-NBCNT membrane catalyst applicability, an easily followable gas phased reaction was chosen, which is the most widely used method in catalytic research for fast-testing of catalysts. The hydrogenation of 1-butene was carried out in a continuous flow system by the application of two membranes. The weight hourly space velocity (WHSV) was 27.45 kg 1-butene/1 kg catalyst/1 h. The 1-butene concentration was checked in a hydrogen-

nitrogen gas mixture by FTIR measurements. The 1-butene concentration was calculated based on the change of the C=C vibration band intensity at 1646 cm^{-1} wavenumber (Figure 33A); this measuring mode was calibrated with different amounts of olefin containing N_2-H_2 mixtures. By applying only one of the two membranes, the yielded 1-butene conversion was 85.3 %, and after 7 minutes, the membrane catalyst reached its maximum catalytic activity (Figure 33 B). By using two membranes, the 1-butene conversion improved to 98 % by 10 min hydrogenation. The membranes are very thin (35 ± 5 µm); nonetheless, they are catalytically efficient for hydrogenation for olefin in a gas phase reaction. Their remarkable catalytic behaviour can be explained by the very high dispersibility of platinum nanoparticles (d_{av} = 3.0 nm) and the homogenous coverage per Pt particle of the fibers in the membrane matrix.t

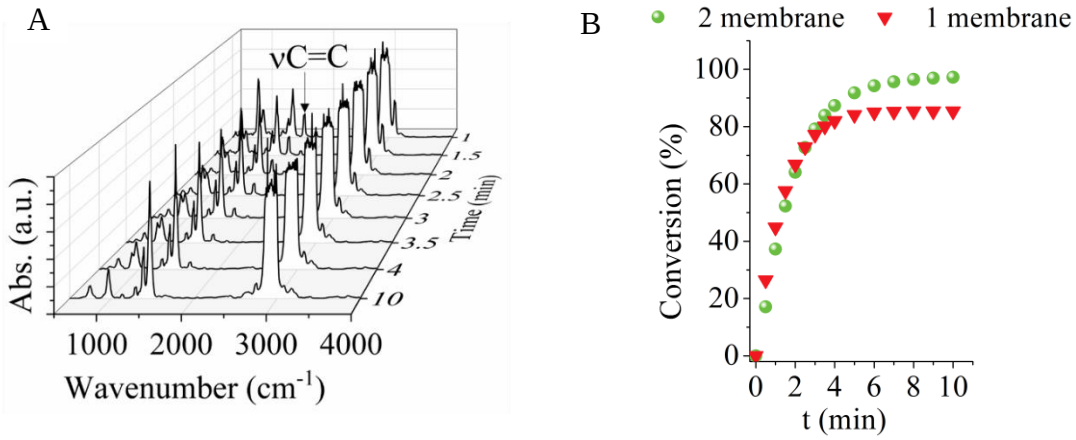

Figure 33. FTIR spectra of the 1-butene-hydrogen-nitrogen-butane mixture vs. time of hydrogenation (A); 1-butene conversion vs. hydrogenation time by applying 1 or 2 membranes (B).

4. Summary

The experimental results obtained during this Ph.D. work could be summarized in the following conclusions:

- The surface of SDS modified MWCNT were successfully coated with ZnO nanoparticles by a noncovalent impregnation method. The synthesis was successful in each case, although the resulted ZnO-MWCNT composites' structure was different. By applying the TEM technique, different layer construction and morphology were observed using EtOH and H_2O as solvents. The impregnation method's products were ideal candidates as starting material in photocatalytic measurements due to the partially covered MWCNTs, which are involved in the adsorption process during photocatalysis. The as-prepared ZnO-MWCNT nanocomposites exhibit enhanced photocatalytic degradation property of acetaldehyde (AA), caused by electron transfer processes from the attached ZnO MWCNT, in which MWCNT plays a role of an electron acceptor while ZnO is considered as a good electron donor. The synthesized ZnO-MWCNT nanocomposite prepared in EtOH showed the highest photocatalytic efficiency (71%) during the UV irradiated degradation of AA.

- The synthesis of ZnO-MWCNT composite materials was made using two different preparation methods. These were the impregnation, and the solvothermal synthesis techniques. We reported that these synthesis ways were successful, but the structure of composites and the size of the ZnO particles formed were different. Using the scanning electron microscopy technique, it was verified that different layer construction and morphology could be obtained by varying the applied synthesis techniques. Moreover, Raman measurements confirmed the presence of ZnO crystallites on the surface of MWCNT and the interaction between them. Using the impregnation surface of MWCNT was not completely covered with ZnO nanoparticles, while in hydrothermal synthesis, micrometer size ZnO particles formed. The differences observed between the two types of synthesis could be explained by the disparity of nanocrystallite size of ZnO. The results made it clear that the best wrappings were obtained using solvothermal synthesis. The biggest advantage of the hydrothermal method is that by changing the reactant's concentration, the coverage of ZnO particles on the surface of MWCNTs can be controlled easily.

- A new type of bacterial cellulose-based hybrid membrane (BC-ZnO-MWCNT) was developed and characterized. We showed that by choosing the appropriate synthesis method of ZnO-MWCNT composite additive (such as impregnation or solvothermal), the physical parameters of the as-prepared membranes could be tailored to specific applications. Zeta potential and contact angle data proved that the surface properties of hybrid membranes were modified significantly in a controllable way by the preparation method and concentration of the ZnO-MWCNT composite additive. The Zeta potential is positive for the SOLVO 80 and SOLVO 90 membranes over the pH range of drinking water. Furthermore, these membranes have the highest surface area value. Similarly, the differences in conductivity values of membranes also confirmed the importance of the synthesis method, and the SOLVO membranes showed higher conductivity over the IMP membranes. Raman spectroscopy confirmed that the intensity and position of the D- and G- bands of MWCNT in the composite were changed in comparison to those in the pristine nanotube. Thus, based on the results of Raman measurements, the formation of a chemical bond between BC fibers and MWCNT-based inorganic additive can be described as an interaction between two nanometric supra-molecular structures. The uniform structure of ZnO-MWCNT additives and the favorable MWCNT-BC matrix interaction led to excellent mechanical properties and flexibility.

- The adsorption, photocatalytic and antibacterial properties of the cellulose-ZnO-MWCNT hybrid membranes were presented. The as-prepared membranes were characterized by SEM, CT, and MIP equipment. The photocatalytic degradation of MB and the removal efficiency and antibacterial properties against *Gram-negative E. Coli* bacteria of the as-prepared hybrid membranes were studied. By comparing the results, it was found that SOLVO 80 membrane showed outstanding properties during these experiments. Both the photocatalytic degradation of MB and the *E. Coli* removal efficiency was achieved 92% in the case of SOLVO 80. Moreover, SOLVO membranes showed much better mechanical stability under UV-irradiation and in the filtration experiments. In contrast, IMP membranes were damaged during both photocatalysis and filtration experiments due to their lower tensile strength parameter. Thus, the application of BC-ZnO-MWCNT-SOLVO

membranes containing ZnO particles in a micrometer range could offer further advantages and potential application alternatives such as a field of photocatalyst-based water treatment technology.

- The BC-Pt-NBCNT support membrane is applicable for the deposition of highly-dispersive platinum nanoparticles on its surface, opening new pathways for the application of hybrid membrane technology. Owing to the interactions between the surface functional groups (-OH, -COOH) of nanotubes and cellulose, bundles were formed, which built up the membrane structure. The platinum decorated self-supporting nano-fibred membranes were tested in gas-phase hydrogenation of 1-butene in a continuous flow system. By using two membranes, high 1-butene conversion (98 %) was reached after 10 min with continuous flow.

5. New scientific results

1st thesis

ZnO-MWCNT composites were prepared under two different solvents conditions, water and EtOH. The impact of the solvent on the morphological, structural, optical properties was verified by transmission electron microscopy (TEM), X-ray powder diffraction (XRD) and the photocatalytic degradation of acetaldehyde (AA) was explored by gas chromatography (GC). We showed that using EtOH as a solvent has been the best option, and the degradation of 71% of acetaldehyde was achieved. This is explained by the impact of the surface tension of the solvent used.

2nd thesis

By changing the preparation method, two different morphologies of the ZnO-MWCNT composites were observed. The first one being carbon nanotubes covered with nanoparticles of ZnO (impregnation technique), and the second is micro-sized hexagonal ZnO particles in which carbon nanotubes were built (solvothermal method) proven by the focus ion beam scanning electron microscopy (FIB-SEM) analysis. Consequently, by choosing the appropriate synthesis route (impregnation technique or solvothermal method) the structural and mechanical properties of the as-prepared ZnO-MWCNT composites can be affected easily.

3rd thesis

As it is well-known the MWCNT has high specific surface area and excellent adsorption properties, ZnO a semiconductor material with a bandgap of 3.2 eV allowing it to have a good photocatalytic activity toward the pollutants present in water, and bacterial cellulose is an ideal candidate as a cheap and environmental friendly matrix material in order to fabricate a self-supported and flexible membrane. To prepare novel hybrid membranes containing BC and ZnO-MWCNT composite additives a simple and cheap so-called papermaking method was applied. We demonstrated that by combining the three substances (BC, ZnO and MWCNT), synergistic effects can be achieved by the as-prepared membranes for several applications, such as photodegradation of organic dyes and bacteria retention.

4th thesis

The as-prepared BC-ZnO-MWCNT hybrid membranes were investigated in the removal experiments of organic dyes and bacteria in order to prove their usability and efficacy towards contaminants present in water. The methylene blue (MB) was chosen as a model for dyes, and E. *Coli* was selected as the model of bacteria. Comparing the results of both type of membranes, IMP and SOLVO, we concluded that SOLVO membranes - containing micro meter size ZnO microparticles - showed the highest photocatalytic efficiency (92%) and an antibacterial retention of (92%). These ZnO microcrystals act as an effective trap in the retention and degradation processes of organic dyes and bacteria, as larger photoactive centres. We confirmed by X-ray micro-computed tomography (μCT) analysis that, ZnO particles in the micrometer range have significantly higher volume than ZnO nanoparticles, which explains the increased photocatalytic performance of SOLVO membranes.

6. Publications

Articles connecting the dissertation:

1. **B. El Mrabate,** E. Szőri-Dorogházi, M. A. Shehab, T. Chauhan, G. Muránszky, E. Sikora, Á. Filep, N. Sharma, L.Nánai, K. Hernadi, Z. Németh
   Widespread applicability of bacterial cellulose-ZnO-MWCNT hybrid membranes.
   ARABIAN JOURNAL OF CHEMISTRY – submitted article (

2. **B. El Mrabate,** Á. Prekob, L. Vanyorek, E. Csiszár, F. Kristály, M. Leskó, Z. Németh
   Catalytic hydrogenation of n-butene with nanosized Pt/NBCNT hybrid membranes einforced with bacterial cellulose.
   JOURNAL OF MATERIALS SCIENCE 56 (2021) 927-935.
   IF: 3.553 (Q1)

3. **B. El Mrabate,** M. Udayakumar, E. Csiszár, F. Kristály, M. Leskó, L. Somlyai-Sipos, M. Schabikowski, Z. Németh
   Development of bacterial cellulose-ZnO-MWCNT hybrid membranes: a study of structural and mechanical properties.
   ROYAL SOCIETY OPEN SCIENCE 7 (2020) 200592.
   IF: 2.647 (D1)

4. **B. El Mrabate**, M. Udayakumar, M. Schabikowski, Z. Németh
   Comparative Electron Microscopy study of the ZnO/MWCNT nanocomposites prepared by different methods.
   CIRCULAR ECONOMY AND ENVIRONMENTAL PROTECTION 3(1) (2019) 16-24.
   IF: - (ISSN 2560-1024)

5. E. Bartfai, K. Nemeth, **B. El Mrabate**, M. Udayakumar, K. Hernadi, Z. Nemeth
   Synthesis, Characterization and Photocatalytic Efficiency of ZnO/MWCNT Nanocomposites Prepared Under Different Solvent Conditions.
   JOURNAL OF NANOSCIENCE AND NANOTECHNOLOGY 19:1 (2019) 422-428.
   IF: 1.354 (Q3)

Other publications:

1. L. Vanyorek, Á. Prekob, E. Sikora, G. Muránszky, **B. El Mrabate**, M. Udayakumar, P. Pekker, B. Viskolcz, Z. Németh
   Development of N-doped bamboo-shaped carbon nanotube/magnesium oxide nanocomposites.
   JOURNAL OF COMPOSITE MATERIALS 54(6) (2019) 857-863.
   IF: 1.972 (Q2)

2. M. Udayakumar, **B. El Mrabate**, T. Koós, K. Szemmelveisz, J. Lakatos, L. Vanyorek, Z. Németh
   Preparation and investigation of carbon foams from waste polyurethanes.
   CIRCULAR ECONOMY AND ENVIRONMENTAL PROTECTION 3:1 (2019) 5-15.
   IF: - (ISSN 2560-1024)

Conference presentations:

1. **B. El Mrabate**, M. Udayakumar, Z. Németh
   Influence of the preparation technique on the properties of MWCNT/ZnO used as additives for BC hybrid membranes.
   9TH VISEGRAD SYMPOSIUM ON STRUCTURAL SYSTEMS BIOLOGY
   Szilvásvárad, Hungary (2019)
   Poster Presentation

2. M. Udayakumar, **B. El Mrabate**, T. Koós, K. Szemmelveisz, J. Lakatos, L. Vanyorek, Z. Németh
   Effective recycling of polyurethane wastes with enhanced CO_2 reduction.
   9TH VISEGRAD SYMPOSIUM ON STRUCTURAL SYSTEMS BIOLOGY
   Szilvásvárad, Hungary (2019)
   Poster Presentation

3. **B. El Mrabate,** Z. Németh
   Design of photoactive bacterial cellulose-based hybrid membranes.
   3rd INTERNATIONAL CONFERENCE ON MEMBRANE SCIENCE AND TECHNOLOGY
   Barcelona, Spain (2019)
   Oral Presentation

4. M. Udayakumar, **B. El Mrabate**, T. Koós, K. Szemmelveisz, J. Lakatos, L. Vanyorek, Z. Németh
   A comparative study of carbon foams prepared from waste polyurethanes under different pyrolysis conditions.
   18TH AUSTRIAN CHEMISTRY DAYS
   Linz, Austria (2019)
   Poster Presentation

7. References

[1] N. Mohammed, N. Grishkewich and K. C. Tam, Cellulose nanomaterials: promising sustainable nanomaterials for application in water/wastewater treatment processes, *Environ. Sci.: Nano*, **2018**, 5, 623–658.

[2] C. Santhosh, V. Velmurugan, G. Jacob, S. K. Jeong, A. N. Grace and A. Bhatnagar, Role of nanomaterials in water treatment applications: A review, *Chemical Engineering Journal*, **2016**, 306, 1116–1137.

[3] S. Kar, R. C. Bindal and P. K. Tewari, Carbon nanotube membranes for desalination and water purification: Challenges and opportunities, *Nano Today*, **2012**, 7, 385–389.

[4] D. Zhou, L. Zhu, Y. Fu, M. Zhu and L. Xue, Development of lower cost seawater desalination processes using nanofiltration technologies — A review, *Desalination*, **2015**, 376, 109–116.

[5] P. S. Goh, A. F. Ismail and B. C. Ng, Carbon nanotubes for desalination: Performance evaluation and current hurdles, *Desalination*, **2013**, 308, 2–14.

[6] Jordi Lladó Valero, Adsorption of organic and emerging pollutants on carbon materials in aqueous media. Environmental implications, *PhD thesis*, Universitat Politècnica de Catalunya, **2014**.

[7] X. Qu, P.J.J. Alvarez, Q. Li, Applications of nanotechnology in water and wastewater treatment, *Water Res.*, **2013**, 47, 3931–3946.

[8] M.M. Pendergast, E.M. V Hoek, A review of water treatment membrane nanotechnologies, *Environ. Sci.* ,**2011**, 4, 1946–1971.

[9] G. Zhu, H. Xu, A. Dufresne and N. Lin, High-Adsorption, Self-Extinguishing, Thermal, and Acoustic-Resistance Aerogels Based on Organic and Inorganic Waste Valorization from Cellulose Nanocrystals and Red Mud, *ACS Sustainable Chem. Eng.*, **2018**, 6, 7168–7180.

[10] M. Gouda, A. Hebeish and A. Aljafari, Synthesis and characterization of novel drug delivery system based on cellulose acetate electrospun nanofiber mats, *Journal of Industrial Textiles*, **2013**, 43, 319–329.

[11] P. Bazant, I. Kuritka, L. Munster and L. Kalina, Microwave solvothermal decoration of the cellulose surface by nanostructured hybrid Ag/ZnO particles: a joint XPS, XRD and SEM study, *Cellulose*, **2015**, 22, 1275–1293.

[12] N. A. Ibrahim, B. M. Eid, E. Abd El-Aziz and T. M. Abou Elmaaty, Functionalization of linen/cotton pigment prints using inorganic nano structure materials, *Carbohydr Polym*, **2013**, 97, 537–545.

[13] A. Jiménez and R. A. Ruseckaite, Binary mixtures based on polycaprolactone and cellulose derivatives, *J Therm Anal Calorim*, **2006**, 88, 851–856.

[14] S. B. Khan, K. A. Alamry, E. N. Bifari, A. M. Asiri, M. Yasir, L. Gzara and R. Z. Ahmad, Assessment of antibacterial cellulose nanocomposites for water permeability and salt rejection, *J Ind Eng Chem*, **2015**, 24, 266–275.

[15] S.-W. Zhao, C.-R. Guo, Y.-Z. Hu, Y.-R. Guo and Q.-J. Pan, The preparation and antibacterial activity of cellulose/ZnO composite: a review, *Open Chemistry*, **2018**, 16, 9–20.

[16] E. Csiszár and S. Nagy, A comparative study on cellulose nanocrystals extracted from bleached cotton and flax and used for casting films with glycerol and sorbitol plasticisers, *Carbohydrate Polymers*, **2017**, 174, 740–749.

[17] F. Cheng, J. W. Betts, S. M. Kelly, D. W. Wareham, A. Kornherr, F. Dumestre, J. Schaller and T. Heinze, Whiter, brighter, and more stable cellulose paper coated with antibacterial carboxymethyl starch stabilized ZnO nanoparticles, *J. Mater. Chem. B*, **2014**, 2, 3057–3064.

[18] L. Jiao, J. Ma and H. Dai, Preparation and Characterization of Self-Reinforced Antibacterial and Oil-Resistant Paper Using a NaOH/Urea/ZnO Solution, *PLoS ONE*, **2015**, 10, e0140603.

[19] S. Azizi, M. B. Ahmad, M. Zobir Hussein, N. A. Ibrahim and F. Namvar, Preparation and properties of poly(vinyl alcohol)/chitosan blend bionanocomposites reinforced with cellulose nanocrystals/ZnO-Ag multifunctional nanosized filler, *Int J Nanomedicine*, **2014**, 1909.

[20] O. M. El-Feky, E. A. Hassan, S. M. Fadel and M. L. Hassan, Use of ZnO nanoparticles for protecting oil paintings on paper support against dirt, fungal attack, and UV aging, *Journal of Cultural Heritage*, **2014**, 15, 165–172.

[21] M. A. Hubbe, O. J. Rojas, L. A. Lucia, and M. Sain, Cellulosic nanocomposites: a review. *BioResources*, **2008**, 3, 929-980.

[22] X. Xu, Y.-Q. Yang, Y.-Y. Xing, J.-F. Yang and S.-F. Wang, Properties of novel polyvinyl alcohol/cellulose nanocrystals/silver nanoparticles blend membranes, *Carbohydrate Polymers*, **2013**, 98, 1573–1577.

[23] Q. Cheng, D. Ye, C. Chang and L. Zhang, Facile fabrication of superhydrophilic membranes consisted of fibrous tunicate cellulose nanocrystals for highly efficient oil/water separation, *Journal of Membrane Science*, **2017**, 525, 1–8.

[24] A. W. Carpenter, C.-F. de Lannoy and M. R. Wiesner, Cellulose Nanomaterials in Water Treatment Technologies, *Environ. Sci. Technol.*, **2015**, 49, 5277–5287.

[25] R. E. Abouzeid, R. Khiari, D. Beneventi and A. Dufresne, Biomimetic Mineralization of Three-Dimensional Printed Alginate/TEMPO-Oxidized Cellulose Nanofibril Scaffolds for Bone Tissue Engineering, *Biomacromolecules*, **2018**, 19, 4442–4452.

[26] H. Zhu, S. Jia, T. Wan, Y. Jia, H. Yang, J. Li, L. Yan and C. Zhong, Biosynthesis of spherical Fe_3O_4/bacterial cellulose nanocomposites as adsorbents for heavy metal ions, *Carbohydrate Polymers*, **2011**, 86, 1558–1564.

[27] V. K. Thakur and S. I. Voicu, Recent advances in cellulose and chitosan-based membranes for water purification: A concise review, *Carbohydrate Polymers*, **2016**, 146, 148–165.

[28] WHO and UNICEF Progress on Drinking Water and Sanitation. *In Hydrologie Und Wasserbewirtschaftung*, **2014**, 58, 244−245.

[29] B. Michen, Virus removal in ceramic depth filters: The electrostatic enhanced adsorption approach *PhD Thesis*. Freiberg, **2010**.

[30] H. Huang, T. A. Young, K. J. Schwab and J. G. Jacangelo, Mechanisms of virus removal from secondary wastewater effluent by low pressure membrane filtration, *Journal of Membrane Science*, **2012**, 409–410, 1–8.

[31] S. A. Baghoth, S. K. Sharma and G. L. Amy, Tracking natural organic matter (NOM) in a drinking water treatment plant using fluorescence excitation–emission matrices and PARAFAC, *Water Research*, **2011**, 45, 797–809.

[32] A. S. Brady-Estévez, M. H. Schnoor, C. D. Vecitis, N. B. Saleh and M. Elimelech, Multiwalled Carbon Nanotube Filter: Improving Viral Removal at Low Pressure, *Langmuir*, **2010**, 26, 14975–14982.

[33] H. Sehaqui, L. Schaufelberger, B. Michen and T. Zimmermann, Humic acid desorption from a positively charged nanocellulose surface, *Journal of Colloid and Interface Science*, **2017**, 504, 500–506.

[34] Z. Sui, Q. Meng, X. Zhang, R. Ma and B. Cao, Green synthesis of carbon nanotube–graphene hybrid aerogels and their use as versatile agents for water purification, *J. Mater. Chem.*, **2012**, 22, 8767.

[35] Y. Han, Z. Xu and C. Gao, Ultrathin Graphene Nanofiltration Membrane for Water Purification, *Adv. Funct. Mater.*, **2013**, 23, 3693–3700.

[36] S. K. Khetan and T. J. Collins, Human Pharmaceuticals in the Aquatic Environment: A Challenge to Green Chemistry, *Chem. Rev.*, **2007**, 107, 2319–2364.

[37] R. Daghrir, P. Drogui and D. Robert, Modified TiO_2 For Environmental Photocatalytic Applications: A Review, *Ind. Eng. Chem. Res.*, **2013**, 52, 3581–3599.

[38] C. M. Friend, Perspectives on Heterogeneous Photochemistry, *The Chemical Record*, **2014**, 14, 944–951.

[39] M. M. Momeni and Z. Nazari, Preparation of TiO_2 and WO_3–TiO_2 nanotubes decorated with PbO nanoparticles by chemical bath deposition process: A stable and efficient photo catalyst, *Ceramics International*, **2016**, 42, 8691–8697.

[40] L. Ma, X. Dong, M. Chen, L. Zhu, C. Wang, F. Yang and Y. Dong, Fabrication and Water Treatment Application of Carbon Nanotubes (CNTs)-Based Composite Membranes: A Review, Membranes, 2017, 7, 16.

[**41**] M. Sweetman, S. May, N. Mebberson, P. Pendleton, K. Vasilev, S. Plush and J. Hayball, Activated Carbon, Carbon Nanotubes and Graphene: Materials and Composites for Advanced Water Purification, C, 2017, 3, 18.

[42] R. K. Yadav, G. H. Oh, N.-J. Park, A. Kumar, K. Kong and J.-O. Baeg, Highly Selective Solar-Driven Methanol from CO_2 by a Photocatalyst/Biocatalyst Integrated System, *J. Am. Chem. Soc.*, **2014**, 136, 16728–16731.

[43] P. M. Ajayan and O. Z. Zhou, Applications of Carbon Nanotubes, Topics in Applied Physics, *Springer Berlin Heidelberg*, **2001**, 80, 391–425.

[44] M. F. L. De Volder, S. H. Tawfick, R. H. Baughman and A. J. Hart, Carbon Nanotubes: Present and Future Commercial Applications, *Science*, **2013**, 339, 535–539.

[45] C. W. Tan, K. H. Tan, Y. T. Ong, A. R. Mohamed, S. H. S. Zein and S. H. Tan, Energy and environmental applications of carbon nanotubes, *Environ Chem Lett*, **2012**, 10, 265–273.

[46] Y. Sakata, Md. A. Uddin, A. Muto and M. Imaoka, Carbon-supported well-dispersed Cu-ZnO catalysts prepared from sawdust impregnated with [$Cu(NO_3)_2$, $Zn(NO_3)_2$] solution: catalytic activity in CO_2 hydrogenation to methanol, *Microporous Materials*, **1997**, 9, 183–187.

[47] R. Das, S. B. Abd Hamid, Md. E. Ali, A. F. Ismail, M. S. M. Annuar and S. Ramakrishna, Multifunctional carbon nanotubes in water treatment: The present, past and future, *Desalination*, **2014**, 354, 160–179.

[48] T. A. Saleh and V. K. Gupta, Functionalization of tungsten oxide into MWCNT and its application for sunlight-induced degradation of rhodamine B, *Journal of Colloid and Interface Science*, **2011**, 362, 337–344.

[49] J. E. Riggs, Z. Guo, D. L. Carroll and Y.-P. Sun, Strong Luminescence of Solubilized Carbon Nanotubes, *J. Am. Chem. Soc.*, **2000**, 122, 5879–5880.

[50] V. Subramanian, E. E. Wolf and P. V. Kamat, Catalysis with TiO_2/Gold Nanocomposites. Effect of Metal Particle Size on the Fermi Level Equilibration, *J. Am. Chem. Soc*., **2004**, 126, 4943–4950.

[51] Q. Geng, Q. Guo, C. Cao and L. Wang, Investigation into NanoTiO_2/ACSPCR for Decomposition of Aqueous Hydroquinone, *Ind. Eng. Chem. Res*., **2008**, 47, 2561–2568.

[52] B. Réti, K. Németh, Z. Németh, K. Mogyorósi, K. Markó, A. Erdőhelyi, A. Dombi and K. Hernadi, Photocatalytic measurements of TiO2/MWCNT catalysts having different surface coverage, *Phys. Status Solidi B*, **2011**, 248, 2475–2479.

[53] A. Jitianu, T. Cacciaguerra, R. Benoit, S. Delpeux, F. Béguin and S. Bonnamy, Synthesis and characterization of carbon nanotubes–TiO_2 nanocomposites, *Carbon*, **2004**, 42, 1147–1151.

[54] V. M. Aroutiounian, V. M. Arakelyan, E. A. Khachaturyan, G. E. Shahnazaryan, M. S. Aleksanyan, L. Forro, A. Magrez, K. Hernadi and Z. Nemeth, Manufacturing and investigations of i-butane sensor made of SnO2/multiwall-carbon-nanotube nanocomposite, *Sensors and Actuators B: Chemical*, **2012**, 173, 890–896.

[55] J. Khanderi, C. Contiu, J. Engstler, R. C. Hoffmann, J. J. Schneider, A. Drochner and H. Vogel, Binary [Cu_2O/MWCNT] and ternary [Cu_2O/ZnO/MWCNT] nanocomposites: formation, characterization and catalytic performance in partial ethanol oxidation, *Nanoscale*, **2011**, 3, 1102–1112.

[56] Y. Yu, L.-L. Ma, W.-Y. Huang, F.-P. Du, J. C. Yu, J.-G. Yu, J.-B. Wang and P.-K. Wong, Sonication assisted deposition of Cu_2O nanoparticles on multiwall carbon nanotubes with polyol process, *Carbon*, **2005**, 43, 670–673.

[57] L.-P. Zhu, G.-H. Liao, W.-Y. Huang, L.-L. Ma, Y. Yang, Y. Yu and S.-Y. Fu, Preparation, characterization and photocatalytic properties of ZnO-coated multi-walled carbon nanotubes, *Materials Science and Engineering: B*, **2009**, 163, 194–198.

[58] L. Jiang and L. Gao, Fabrication and characterization of ZnO-coated multi-walled carbon nanotubes with enhanced photocatalytic activity, *Materials Chemistry and Physics*, **2005**, 91, 313–316.

[59] X. Wang, B. Xia, X. Zhu, J. Chen, S. Qiu and J. Li, Controlled modification of multiwalled carbon nanotubes with Zno nanostructures, *Journal of Solid State Chemistry*, **2008**, 181, 822–827.

[60] M. H. Huang, Room-Temperature Ultraviolet Nanowire Nanolasers, *Science*, **2001**, 292, 1897–1899.

[61] Z.-Y. Jiang, Z.-X. Xie, X.-H. Zhang, S.-C. Lin, T. Xu, S.-Y. Xie, R.-B. Huang and L.-S. Zheng, Synthesis of Single-Crystalline ZnO Polyhedral Submicrometer-Sized Hollow Beads Using Laser-Assisted Growth with Ethanol Droplets as Soft Templates, *Adv. Mater*., **2004**, 16, 904–907.

[62] W. N. Kang, H. J. Kim, H.-J. Kim, E.-M. Choi, K. H. P. Kim, H. S. Lee and S.-I. Lee, Synthesis ofc-axis-oriented MgB2thin films and the Hall effect, Supercond. *Sci. Technol*., **2003**, 16, 237–240.

[63] J. Liu, X. Li and L. Dai, Water-Assisted Growth of Aligned Carbon Nanotube–ZnO Heterojunction Arrays, *Adv. Mater*., **2006**, 18, 1740–1744.

[64] Y. Zhu, H. I. Elim, Y.-L. Foo, T. Yu, Y. Liu, W. Ji, J.-Y. Lee, Z. Shen, A. T. S. Wee, J. T. L. Thong and C. H. Sow, Multiwalled Carbon Nanotubes Beaded with ZnO Nanoparticles for Ultrafast Nonlinear Optical Switching, *Adv. Mater*., **2006**, 18, 587–592.

[65] M. Alaf, D. Gultekin and H. Akbulut, A New Approach to Synthesis of Free-Standing ZnO/MWCNT Nanocomposites by Vacuum Infiltration, *Acta Phys. Pol. A*, **2014**, 125, 426–428.

[66] Y. W. Koh, M. Lin, C. K. Tan, Y. L. Foo and K. P. Loh, Self-Assembly and Selected Area Growth of Zinc Oxide Nanorods on Any Surface Promoted by an Aluminum Precoat, *J. Phys. Chem. B*, **2004**, 108, 11419–11425.

[**67**] M. Shaban, A. M. Ashraf and M. R. Abukhadra, TiO2 Nanoribbons/Carbon Nanotubes Composite with Enhanced Photocatalytic Activity; Fabrication, Characterization, and Application, *Sci Rep*, **2018**, 8, 781.

[68] C. S. Chen, X. H. Chen, B. Yi, T. G. Liu, W. H. Li, L. S. Xu, Z. Yang, H. Zhang and Y. G. Wang, Zinc oxide nanoparticle decorated multi-walled carbon nanotubes and their optical properties, *Acta Materialia*, **2006**, 54, 5401–5407.

[69] V. Datsyuk, M. Kalyva, K. Papagelis, J. Parthenios, D. Tasis, A. Siokou, I. Kallitsis and C. Galiotis, Chemical oxidation of multiwalled carbon nanotubes, *Carbon*, **2008**, 46, 833–840.

[70] K. J. Ziegler, Z. Gu, H. Peng, E. L. Flor, R. H. Hauge and R. E. Smalley, Controlled Oxidative Cutting of Single-Walled Carbon Nanotubes, *J. Am. Chem. Soc*., **2005**, 127, 1541–1547.

[71] M. W. Marshall, S. Popa-Nita and J. G. Shapter, Measurement of functionalised carbon nanotube carboxylic acid groups using a simple chemical process, *Carbon*, **2006**, 44, 1137–1141.

[72] H. Wang, H.-L. Wang and W.-F. Jiang, Solar photocatalytic degradation of 2,6-dinitro-p-cresol (DNPC) using multi-walled carbon nanotubes (MWCNT)–TiO_2 composite photocatalysts, *Chemosphere*, **2009**, 75, 1105–1111.

[73] G. Jiang, X. Zheng, Y. Wang, T. Li and X. Sun, Photo-degradation of methylene blue by multi-walled carbon nanotubes/TiO_2 composites, *Powder Technology*, **2011**, 207, 465–469.

[74] T. A. Saleh and V. K. Gupta, Photo-catalyzed degradation of hazardous dye methyl orange by use of a composite catalyst consisting of multi-walled carbon nanotubes and titanium dioxide, *Journal of Colloid and Interface Science*, **2012**, 371, 101–106.

[75] M. Sangari, M. Umadevi, J. Mayandi and J. P. Pinheiro, Photocatalytic degradation and antimicrobial applications of F-doped MWCNT/TiO_2 composites, *Spectrochimica Acta Part A: Molecular and Biomolecular Spectroscopy*, **2015**, 139, 290–295.

[76] K. E. Tettey, M. Q. Yee and D. Lee, Photocatalytic and Conductive MWCNT/TiO_2 Nanocomposite Thin Films, *ACS Appl. Mater. Interfaces*, **2010**, 2, 2646–2652.

[77] F.-J. Zhang, W.-C. Oh and K. Zhang, New insight for enhancing photocatalytic activity of MWCNT/TiO_2 by decorating palladium nanoparticles as charge-transfer channel, *Materials Research Bulletin*, **2012**, 47, 619–624.

[78] Q. Wang, J. Shang, H. Song, T. Zhu, J. Ye, F. Zhao, J. Li and S. He, Visible-light photoelectrocatalytic degradation of rhodamine B over planar devices using a multi-walled carbon Nanotube-TiO_2 composite, *Materials Science in Semiconductor Processing*, **2013**, 16, 480–484.

[79] J. Wang, P. Wang, Y. Cao, J. Chen, W. Li, Y. Shao, Y. Zheng and D. Li, A high efficient photocatalyst Ag_3VO_4/TiO_2/graphene nanocomposite with wide spectral response, *Applied Catalysis B: Environmental*, **2013**, 136–137, 94–102.

[80] Z. Li, L. He, L. Jing, J. Lin and Y. Luan, Facile Synthesis of Phosphate-Functionalized MWCNT-TiO_2 Nanocomposites as Efficient Photocatalysts and Insights into the Roles of Nanostructured Carbon, *ChemPlusChem*, **2013**, 78, 670–676.

[81] T. S. Natarajan, J. Y. Lee, H. C. Bajaj, W.-K. Jo and R. J. Tayade, Synthesis of multiwall carbon nanotubes/TiO_2 nanotube composites with enhanced photocatalytic decomposition efficiency, *Catalysis Today*, **2017**, 282, 13–23.

[82] M. Ahmad, E. Ahmed, Z. L. Hong, W. Ahmed, A. Elhissi and N. R. Khalid, Photocatalytic, sonocatalytic and sonophotocatalytic degradation of Rhodamine B using ZnO/CNTs composites photocatalysts, *Ultrasonics Sonochemistry*, **2014**, 21, 761–773.

[83] H.-Y. Phin, Y.-T. Ong and J.-C. Sin, Effect of carbon nanotubes loading on the photocatalytic activity of zinc oxide/carbon nanotubes photocatalyst synthesized via a modified sol-gel method, *Journal of Environmental Chemical Engineering*, **2020**, 8, 103222.

[84] N. Arsalani, S. Bazazi, M. Abuali and S. Jodeyri, A new method for preparing ZnO/CNT nanocomposites with enhanced photocatalytic degradation of malachite green under visible light, *Journal of Photochemistry and Photobiology A: Chemistry*, **2020**, 389, 112207.

[85] C.-H. Chen, Y.-H. Liang and W.-D. Zhang, $ZnFe_2O_4$/MWCNT composite with enhanced photocatalytic activity under visible-light irradiation, *Journal of Alloys and Compounds*, **2010**, 501, 168–172.

[86] Y. Wan, T. Cong, Q. Liang, Z. Li, S. Xu, Y. Peng and D. Lu, Facile in-situ solvothermal method to synthesize ZnPc–MWCNT composites with enhanced visible light photocatalytic activity, *Ceramics International*, **2016**, 42, 2425–2430.

[87] R. M. Mohamed and M. Abdel Salam, Photocatalytic reduction of aqueous mercury(II) using multi-walled carbon nanotubes/Pd-ZnO nanocomposite, *Materials Research Bulletin*, **2014**, 50, 85–90.

[88] S. Vadivel, J. Theerthagiri, J. Madhavan, T. Santhoshini Priya and N. Balasubramanian, Enhanced photocatalytic activity of degradation of azo, phenolic and triphenyl methane dyes using novel octagon shaped BiOCl discs/MWCNT composite, *Journal of Water Process Engineering*, **2016**, 10, 165–171.

[89] **S**. Vadivel, A. N. Naveen, J. Theerthagiri, J. Madhavan, T. Santhoshini Priya and N. Balasubramanian, Solvothermal synthesis of $BiPO_4$ nanorods/MWCNT (1D-1D) composite for photocatalyst and supercapacitor applications, *Ceramics International*, **2016**, 42, 14196–14205.

[90] J. Di, M. Ji, J. Xia, X. Li, W. Fan, Q. Zhang and H. Li, $Bi_4O_5Br_2$ ultrasmall nanosheets in situ strong coupling to MWCNT and improved photocatalytic activity for tetracycline hydrochloride degradation, *Journal of Molecular Catalysis A: Chemical*, **2016**, 424, 331–341.

[91] D. D. Chronopoulos, N. Karousis, S. Zhao, Q. Wang, H. Shinohara and N. Tagmatarchis, Photocatalytic application of nanosized CdS immobilized onto functionalized MWCNT, *Dalton Trans.*, **2014**, 43, 7429.

[92] H.-Y. Zhu, J. Yao, R. Jiang, Y.-Q. Fu, Y.-H. Wu and G.-M. Zeng, Enhanced decolorization of azo dye solution by cadmium sulfide/multi-walled carbon nanotubes/polymer composite in combination with hydrogen peroxide under simulated solar light irradiation, *Ceramics International*, **2014**, 40, 3769–3777.

[93] S. Fang, M. Sun, Y. Zhou, Q. Liang, Z. Li and S. Xu, Solvothermal synthesis of CdS QDs/MWCNT nanocomposites with high efficient photocatalytic activity under visible light irradiation, *Journal of Alloys and Compounds*, **2016**, 656, 771–776.

[94] B. Liu, Z. Li, S. Xu, T. Cong, L. Tian, C. Ding and M. Lu, in situ synthesis of $Ag@Ag_3PO_4$/MWCNT triples hetero-photocatalyst for degradation of malachite green, *Materials Letters*, **2014**, 131, 229–232.

[95] L. Cai, T. Xu, J. Shen and W. Xiang, Highly efficient photocatalytic treatment of mixed dyes wastewater via visible-light-driven AgI–Ag_3PO_4/MWCNT, *Materials Science in Semiconductor Processing*, **2015**, 37, 19–28.

[96] D. Klemm, B. Heublein, H.-P. Fink and A. Bohn, Cellulose: Fascinating Biopolymer and Sustainable Raw Material, *Angew. Chem. Int. Ed.*, **2005**, 44, 3358–3393.

[97] A. N. Fernandes, L. H. Thomas, C. M. Altaner, P. Callow, V. T. Forsyth, D. C. Apperley, C. J. Kennedy and M. C. Jarvis, Nanostructure of cellulose microfibrils in spruce wood, *Proceedings of the National Academy of Sciences*, **2011**, 108, E1195–E1203.

[98] D. P. Oehme, M. T. Downton, M. S. Doblin, J. Wagner, M. J. Gidley and A. Bacic, Unique Aspects of the Structure and Dynamics of Elementary Iβ Cellulose Microfibrils Revealed by Computational Simulations, *Plant Physiol.*, **2015**, 168, 3–17.

[99] M. Reza, C. Bertinetto, K. K. Kesari, P. Engelhardt, J. Ruokolaine and T. VuorinenCellulose elementary fibril orientation in the spruce S 1-2 transition layer. *Scientific reports*, **2019**, 9, 1, 1-7.

[100] D. Klemm, F. Kramer, S. Moritz, T. Lindström, M. Ankerfors, D. Gray and A. Dorris, Nanocelluloses: A New Family of Nature-Based Materials, *Angew. Chem. Int. Ed.*, **2011**, 50, 5438–5466.

[101] Y.-C. Hsieh, H. Yano, M. Nogi and S. J. Eichhorn, An estimation of the Young's modulus of bacterial cellulose filaments, *Cellulose*, **2008**, 15, 507–513.

[102] H. Voisin, L. Bergström, P. Liu and A. Mathew, Nanocellulose-Based Materials for Water Purification, *Nanomaterials*, **2017**, 7, 57.

[103] D. Klemm, E. D. Cranston, D. Fischer, M. Gama, S. A. Kedzior, D. Kralisch, F. Kramer, T. Kondo, T. Lindström, S. Nietzsche, K. Petzold-Welcke and F. Rauchfuß, Nanocellulose as a natural source for groundbreaking applications in materials science: Today's state, *Materials Today*, **2018**, 21, 720–748.

[104] A. Mautner, Nanocellulose water treatment membranes and filters: a review, *Polym Int*, **2020**, 69, 741–751.

[105] Gorgieva and Trček, Bacterial Cellulose: Production, Modification and Perspectives in Biomedical Applications, *Nanomaterials*, **2019**, 9, 1352.

[106] M. Liu, L. Liu, S. Jia, S. Li, Y. Zou and C. Zhong, Complete genome analysis of Gluconacetobacter xylinus CGMCC 2955 for elucidating bacterial cellulose biosynthesis and metabolic regulation, *Sci Rep*, **2018**, 8, 1, 1-10.

[107] S.-S. Wang, Y.-H. Han, J.-L. Chen, D.-C. Zhang, X.-X. Shi, Y.-X. Ye, D.-L. Chen and M. Li, Insights into Bacterial Cellulose Biosynthesis from Different Carbon Sources and the Associated Biochemical Transformation Pathways in Komagataeibacter sp. W1, *Polymers*, **2018**, 10, 963.

[108] A. Sionkowska, O. Mężykowska and J. Piątek, Bacterial nanocelullose in biomedical applications: a review, *Polym. Int.*, **2019**, 68, 1841–1847.

[109] Y. Habibi, L. A. Lucia and O. J. Rojas, Cellulose Nanocrystals: Chemistry, Self-Assembly, and Applications, *Chem. Rev*., **2010**, 110, 3479–3500.

[110] R. J. Moon, A. Martini, J. Nairn, J. Simonsen and J. Youngblood, Cellulose nanomaterials review: structure, properties and nanocomposites, *Chem. Soc. Rev*., **2011**, 40, 3941.

[111] AF Turbak, FW Snyder and Sandberg KR, Microfibrillated cellulose, a new cellulose product: properties, uses, and commercial potential, *J Appl Polym Sci*, **1983**, 37,815–827.

[112] M. A. S. Azizi Samir, F. Alloin and A. Dufresne, Review of Recent Research into Cellulosic Whiskers, Their Properties and Their Application in Nanocomposite Field, *Biomacromolecules*, **2005**, 6, 612–626.

[113] S. J. Eichhorn, A. Dufresne, M. Aranguren, N. E. Marcovich, J. R. Capadona, S. J. Rowan, C. Weder, W. Thielemans, M. Roman, S. Renneckar, W. Gindl, S. Veigel, J. Keckes, H. Yano, K. Abe, M. Nogi, A. N. Nakagaito, A. Mangalam, J. Simonsen, A. S. Benight, A. Bismarck, L. A. Berglund and T. Peijs, Review: current international research into cellulose nanofibres and nanocomposites, *J Mater Sci*, **2010**, 45, 1–33.

[**114**] A. Mautner, Nanocellulose water treatment membranes and filters: a review, *Polym Int*, **2020**, 69, 741–751.

[115] S. Hokkanen, A. Bhatnagar and M. Sillanpää, A review on modification methods to cellulose-based adsorbents to improve adsorption capacity, *Water Research*, **2016**, 91, 156–173.

[116] K. P. Y. Shak, Y. L. Pang and S. K. Mah, Nanocellulose: Recent advances and its prospects in environmental remediation, *Beilstein J. Nanotechnol*., **2018**, 9, 2479–2498.

[117] J. Yang, J. Yu, J. Fan, D. Sun, W. Tang and X. Yang, Biotemplated preparation of CdS nanoparticles/bacterial cellulose hybrid nanofibers for photocatalysis application, *Journal of Hazardous Materials*, **2011**, 189, 377–383.

[118] L. Jin, W. Li, Q. Xu and Q. Sun, Amino-functionalized nanocrystalline cellulose as an adsorbent for anionic dyes, *Cellulose*, **2015**, 22, 2443–2456.

[119] Mohammed N, Grishkewich N, Waeijen HA, Berry RM, Tam KC. Continuous flow adsorption of methylene blue by cellulose nanocrystal-alginate hydrogel beads in fixed bed columns. *Carbohydr Polym*. **2016**; 136:1194-1202.

[120] H. Qiao, Y. Zhou, F. Yu, E. Wang, Y. Min, Q. Huang, L. Pang and T. Ma, Effective removal of cationic dyes using carboxylate-functionalized cellulose nanocrystals, *Chemosphere*, **2015**, 141, 297–303.

[121] H. Sehaqui, A. Mautner, U. Perez de Larraya, N. Pfenninger, P. Tingaut and T. Zimmermann, Cationic cellulose nanofibers from waste pulp residues and their nitrate, fluoride, sulphate and phosphate adsorption properties, *Carbohydrate Polymers*, **2016**, 135, 334–340.

[122] **S**. Hokkanen, A. Bhatnagar, E. Repo, S. Lou and M. Sillanpää, Calcium hydroxyapatite microfibrillated cellulose composite as a potential adsorbent for the removal of Cr(VI) from aqueous solution, *Chemical Engineering Journal*, **2016**, 283, 445–452.

[123] S. I. Siddiqui, F. Zohra and S. A. Chaudhry, Nigella sativa seed based nanohybrid composite-Fe_2O_3–SnO_2/BC: A novel material for enhanced adsorptive removal of methylene blue from water, *Environmental Research*, **2019**, 178, 108667.

[124] Y. Li, L. Cao, L. Li and C. Yang, In situ growing directional spindle TiO_2 nanocrystals on cellulose fibers for enhanced Pb^{2+} adsorption from water, *Journal of Hazardous Materials*, **2015**, 289, 140–148.

[125] S. B. Khan, K. A. Alamry, H. M. Marwani, A. M. Asiri and M. M. Rahman, Synthesis and environmental applications of cellulose/ZrO_2 nanohybrid as a selective adsorbent for nickel ion, *Composites Part B: Engineering*, **2013**, 50, 253–258.

[126] **S**. I. Siddiqui and S. A. Chaudhry, Nanohybrid composite Fe_2O_3-ZrO_2/BC for inhibiting the growth of bacteria and adsorptive removal of arsenic and dyes from water, *Journal of Cleaner Production*, **2019**, 223, 849–868.

[127] **C**. Jiao, J. Tao, J. Xiong, X. Wang, D. Zhang, H. Lin and Y. Chen, In situ synthesis of MnO_2-loaded biocomposite based on microcrystalline cellulose for Pb^{2+} removal from wastewater, *Cellulose*, **2017**, 24, 2591–2604.

[128] K. Taleb, J. Markovski, Z. Veličković, J. Rusmirović, M. Rančić, V. Pavlović and A. Marinković, Arsenic removal by magnetite-loaded amino modified nano/microcellulose adsorbents: Effect of functionalization and media size, *Arabian Journal of Chemistry*, **2019**, 12, 4675–4693.

[129] W. Maatar and S. Boufi, Microporous cationic nanofibrillar cellulose aerogel as promising adsorbent of acid dyes, *Cellulose*, **2016**, 24, 1001–1015.

[130] M. Thomas, T. S. Natarajan, M. U. D. Sheikh, M. Bano and F. Khan, Self-organized graphene oxide and TiO_2 nanoparticles incorporated alginate/carboxymethyl cellulose nanocomposites with efficient photocatalytic activity under direct sunlight, *Journal of Photochemistry and Photobiology A: Chemistry*, **2017**, 346, 113–125.

[131] T. S. Anirudhan and J. R. Deepa, Nano-zinc oxide incorporated graphene oxide/nanocellulose composite for the adsorption and photo catalytic degradation of ciprofloxacin hydrochloride from aqueous solutions, *Journal of Colloid and Interface Science*, **2017**, 490, 343–356.

[132] K. Lefatshe, C. M. Muiva and L. P. Kebaabetswe, Extraction of nanocellulose and in-situ casting of ZnO/cellulose nanocomposite with enhanced photocatalytic and antibacterial activity, *Carbohydrate Polymers*, **2017**, 164, 301–308.

[133] P. Chen, X. Liu, R. Jin, W. Nie and Y. Zhou, Dye adsorption and photo-induced recycling of hydroxypropyl cellulose/molybdenum disulfide composite hydrogels, *Carbohydrate Polymers*, **2017**, 167, 36–43.

[134] M. F. Nsib, F. Hajji, A. Mayoufi, N. Moussa, A. Rayes and A. Houas, In situ synthesis and characterization of TiO_2/HPM cellulose hybrid material for the photocatalytic degradation of 4-NP under visible light, *Comptes Rendus Chimie*, **2014**, 17, 839–848.

[135] L.-P. Liu, X.-N. Yang, L. Ye, D.-D. Xue, M. Liu, S.-R. Jia, Y. Hou, L.-Q. Chu and C. Zhong, Preparation and characterization of a photocatalytic antibacterial material: Graphene oxide/TiO_2/bacterial cellulose nanocomposite, *Carbohydrate Polymers*, **2017**, 174, 1078–1086.

[136] M. Thomas, G. A. Naikoo, M. U. D. Sheikh, M. Bano and F. Khan, Effective photocatalytic degradation of Congo red dye using alginate/carboxymethyl cellulose/TiO_2 nanocomposite hydrogel under direct sunlight irradiation, *Journal of Photochemistry and Photobiology A: Chemistry*, **2016**, 327, 33–43.

[137] P. Dong, X. Cheng, Z. Huang, Y. Chen, Y. Zhang, X. Nie and X. Zhang, In-situ and phase controllable synthesis of nanocrystalline TiO_2 on flexible cellulose fabrics via a simple hydrothermal method, *Materials Research Bulletin*, **2018**, 97, 89–95.

[138] M**.** Gao, N. Li, W. Lu and W. Chen, Role of cellulose fibers in enhancing photosensitized oxidation of basic green 1 with massive dyeing auxiliaries, *Applied Catalysis B: Environmental*, **2014**, 147, 805–812.

[139] K**.** Tu, Q. Wang, A. Lu and L. Zhang, Portable Visible-Light Photocatalysts Constructed from Cu_2O Nanoparticles and Graphene Oxide in Cellulose Matrix, *J. Phys. Chem. C*, **2014**, 118, 7202–7210.

[140] M. A. Mohamed, W. N. W. Salleh, J. Jaafar, A. F. Ismail, M. Abd Mutalib and S. M. Jamil, Incorporation of N-doped TiO_2 nanorods in regenerated cellulose thin films fabricated from recycled newspaper as a green portable photocatalyst, *Carbohydrate Polymers*, **2015**, 133, 429–437.

[141] Z. Zhou, X. Peng, L. Zhong, L. Wu, X. Cao and R. C. Sun, Electrospun cellulose acetate supported Ag@AgCl composites with facet-dependent photocatalytic properties on degradation of organic dyes under visible-light irradiation, *Carbohydrate Polymers*, **2016**, 136, 322–328.

[142] G. Li, A. G. Nandgaonkar, Q. Wang, J. Zhang, W. E. Krause, Q. Wei and L. A. Lucia, Laccase-immobilized bacterial cellulose/TiO_2 functionalized composite membranes: Evaluation for photo- and bio-catalytic dye degradation, *Journal of Membrane Science*, **2017**, 525, 89–98.

[143] F. Wahid, Y.-X. Duan, X.-H. Hu, L.-Q. Chu, S.-R. Jia, J.-D. Cui and C. Zhong, A facile construction of bacterial cellulose/ZnO nanocomposite films and their photocatalytic and antibacterial properties, *International Journal of Biological Macromolecules*, **2019**, 132, 692–700.

[144] G. Yang, J. Xie, F. Hong, Z. Cao and X. Yang, Antimicrobial activity of silver nanoparticle impregnated bacterial cellulose membrane: Effect of fermentation carbon sources of bacterial cellulose, *Carbohydrate Polymers*, **2012**, 87, 839–845.

[145] G. P. Szekeres, Z. Németh, K. Schrantz, K. Németh, M. Schabikowski, J. Traber, W. Pronk, K. Hernádi and T. Graule, Copper-Coated Cellulose-Based Water Filters for Virus Retention, *ACS Omega*, **2018**, 3, 446–454.

[146] Z. Zhou, C. Lu, X. Wu and X. Zhang, Cellulose nanocrystals as a novel support for CuO nanoparticles catalysts: facile synthesis and their application to 4-nitrophenol reduction, *RSC Adv.*, **2013**, 3, 26066.

[147] D. Sun, J. Yang and X. Wang, Bacterial cellulose/TiO_2 hybrid nanofibers prepared by the surface hydrolysis method with molecular precision, *Nanoscale*, **2010**, 2, 287–292.

[148] H. Ma, C. Burger, B. S. Hsiao and B. Chu, Nanofibrous Microfiltration Membrane Based on Cellulose Nanowhiskers, *Biomacromolecules*, **2011**, 13, 180–186.

[149]. L. Fu, G. Lai, H. Zhang and A. Yu, One-Pot Synthesis of Multipod ZnO-Carbon Nanotube-Reduced Graphene Oxide Composites with High Performance in Photocatalysis, *j nanosci nanotechnol*, **2015**, 15, 4325–4331.

[150]. E. A. Whitsitt and A. R. Barron, Silica Coated Single Walled Carbon Nanotubes, Nano Lett., **2003**, 3, 775–778.

[151]. R. Smajda, M. Mionic, M. Duchamp, J. C. Andresen, L. Forró and A. Magrez, Production of high-quality carbon nanotubes for less than $1 per gram, *Phys. Status Solidi (c)*, **2010**, 7, 1236-1240.

[152]. A. Di Crescenzo, V. Ettorre and A. Fontana, Non-covalent and reversible functionalization of carbon nanotubes, *Beilstein J. Nanotechnol.*, **2014**, 5, 1675–1690.

[153]. Cruz E, Zheng Y, Torres E, Li W, Song W, Burugapalli K., Zeta potential of modified multi-walled carbon nanotubes in presence of poly(vinyl alcohol) hydrogel. *Int. J. Electrochem. Sci*., **2012**, 7, 3577–3590.

[154]. A. D. French, Idealized powder diffraction patterns for cellulose polymorphs, *Cellulose*, **2013**, 21, 885–896.

[155] S. Brunauer, P. H. Emmett and E. Teller, Adsorption of Gases in Multimolecular Layers, J. Am. Chem. Soc., **1938**, 60, 309–319.

[156] J. Yang, B. Wei, X. Li, J. Wang, H. Zhai, X. Li, Y. Sui, Y. Liu, J. Wang, J. Lang and Q. Zhang, Synthesis of ZnO films in different solvents and their photocatalytic activities, *Crystal Research and Technology*, **2015**, 50, 840–845.

[157] A. L. Patterson, The Scherrer Formula for X-Ray Particle Size Determination, *Phys. Rev.*, **1939**, 56, 978–982

[158] 3000ºF Ceramic Paper and 300R Ceramic Paper Datasheet from http://cotronics.com/vo/cotr/pdf/300.pdf

[159] C. L. Bianchi, S. Gatto, C. Pirola, A. Naldoni, A. Di Michele, G. Cerrato, V. Crocellà and V. Capucci, Photocatalytic degradation of acetone, acetaldehyde and toluene in gas-phase: Comparison between nano and micro-sized TiO2, Applied Catalysis B: Environmental, **2014**, 146, 123–130.

[160] A. Chanda, S. Gupta, M. Vasundhara, S.R. Joshi, G.R. Mutta, J. Singh. Study of structural, optical and magnetic properties of cobalt doped ZnO nanorods. *RSC Advances*, **2017**, 7, 50527-50536.

[161] S. H. Yoon, H.-J. Jin, M.-C. Kook and Y. R. Pyun, Electrically Conductive Bacterial Cellulose Incorporation of Carbon Nanotubes, *Biomacromolecules*, **2006**, 7, 1280–1284.

[162] H. Qi, J. Liu and E. Mäder, Smart Cellulose Fibers Coated with Carbon Nanotube Networks, *Fibers*, **2014**, 2, 295–307.

[163] N. F. Vasconcelos, J. P. A. Feitosa, F. M. P. da Gama, J. P. S. Morais, F. K. Andrade, M. de S. M. de Souza Filho and M. de F. Rosa, Bacterial cellulose nanocrystals produced under different hydrolysis conditions: Properties and morphological features, *Carbohydrate Polymers*, **2017**, 155, 425–431

[164] M. Samadi, H. A. Shivaee, M. Zanetti, A. Pourjavadi and A. Moshfegh, Visible light photocatalytic activity of novel MWCNT-doped ZnO electrospun nanofibers, *Journal of Molecular Catalysis A: Chemical*, **2012**, 359, 42–48.

[165] Z. Németh, E. Horváth, A. Magrez, B. Réti, P. Berki, L. Forró and K. Hernádi, Preparation of titania covered multi-walled carbon nanotube thin films, *Materials & Design*, **2015**, 86, 198–203.

[166] H. Qi, E. Mäder and J. Liu, Electrically conductive aerogels composed of cellulose and carbon nanotubes, *J. Mater. Chem. A*, **2013**, 1, 9714.

[167] D. Baskaran, J. W. Mays and M. S. Bratcher, Noncovalent and Nonspecific Molecular Interactions of Polymers with Multiwalled Carbon Nanotubes, *Chem. Mater.*, **2005**, 17, 3389–3397.

[168] Krässig H., Cellulose-structure accessibility and reactivity. Amsterdam, The Netherlands: *Gordon and Breach Science Publishers* **1993**.

[169] Kim D-Y, Nishiyama Y, Kuga S., Surface acetylation of bacterial cellulose, *Cellulose,* **2002**, 9, 361–367

[170] Y. Sun; S. R. Wilson; D. I. Schuster. High dissolution and strong light emission of carbon nanotubes in aromatic amine solvents. *J. Am. Chem. Soc.* 123 (**2001**) 5348-5349.

[171] P. Berki; Z. Németh; B. Réti; O. Berkesi; A. Magrez; V. Aroutiounian; L. Forro; K. Hernadi. Preparation and characterization of multiwalled carbon nanotube/In_2O_3 composites. *Carbon* 60 (**2013**) 266-272.

[172] M. A. Saleemi; M. H. Fouladi; P. V. C. Yong; E. H. Wong. Elucidation of antimicrobial activity of non-covalently dispersed carbon nanotubes. *Materials* 13(7) (**2020**) 1676.

[173] M. Poletto, V. Pistor, M. Zeni and A. J. Zattera, Crystalline properties and decomposition kinetics of cellulose fibers in wood pulp obtained by two pulping processes, Polymer Degradation and Stability, **2011**, 96, 679–685.

[174] M.-C. Popescu, C.-M. Popescu, G. Lisa and Y. Sakata, Evaluation of morphological and chemical aspects of different wood species by spectroscopy and thermal methods, *Journal of Molecular Structure*, **2011**, 988, 65–72.

[175] K. Fackler, J. S. Stevanic, T. Ters, B. Hinterstoisser, M. Schwanninger and L. Salmén, FT-IR imaging microscopy to localise and characterise simultaneous and selective white-rot decay within spruce wood cells, *Holzforschung*, **2011**, 65, 411–420.